DIMITRIOS KALTSAS

Modelling of the dynamic pressuremeter test in porous soil using analytical and numerical methods

MSc Thesis Project

TU Delft Delft University of Technology

FUGRO

Modelling of the dynamic pressuremeter test in porous soil using analytical and numerical methods

By

Dimitrios Kaltsas

in fulfilment of the requirements for the degree of

Master of Science
in Civil Engineering

at the Delft University of Technology,
to be defended publicly on Monday August 22, 2016 at 11:30 AM.

Student number: 4414195
Duration of project: November 7, 2015 – August 22, 2016
Thesis committee:

Prof. Dr. Ir. Timo J. Heimovaara,	TU Delft (chairman)
Dr. Ir. Karel N. van Dalen	TU Delft (daily supervisor)
Dr. Federico Pisanó	TU Delft (supervisor)
Ir. Flip J.M. Hoefsloot	Fugro GeoServices BV

TU Delft Delft University of Technology

FUGRO

Preface

According to the dictionary, behaviour is the action, reaction, or functioning of a system under normal or specified circumstances. It can be related to any kind of system: from human beings to machines and from animals to artificial materials. Science has always tried to predict and explain the behaviour of any kind of system. When it comes to material behaviour, ground is one of the most challenging ones to analyse. That specific challenge led me to Geotechnical Engineering, TU Delft and the Netherlands.

Following what always challenged me the most, I decided to dig into Soil Dynamics for my Graduation Project. According to Dynamics, the variables which represent the aforementioned behaviour vary in time. Thus, time, and therefore frequency, are factors that play a determinant role on the behaviour of soil; just think about earthquakes. In time or frequency domain (which are interconnected via simple mathematical tools) one can represent features of the behaviour with complex numbers. That I think is almost magic!

The present research is diving into this magical world providing a representation of the soil behaviour during the cone pressuremeter test, which is an in-situ test developed in France for soil characterisation. For the realisation of this project I am grateful to some people.

First of all, I would like to thank my daily supervisor from TU Delft, Dr. Ir. Karel N. van Dalen, who gave me the opportunity to deal with this project, and fully supported me during this whole 9-month period, sometimes multiple times per week. His guidance was continuous and always valuable.

The research was carried out at the offices of Fugro GeoServices BV in Leidschendam, the Netherlands. Hence, I would like to thank the company for hosting and investing in this project. Special thanks are given to Ir. Flip. J.M. Hoefsloot who guided me in most practical aspects, but also for helping me find my way within the company.

I would also like to express my gratitude to Dr. Federico Pisanó for his guidance both when he was present in the Geo-engineering section and when he was working on the other side of the globe. Finally, Prof. Dr. Ir. Timo J. Heimovaara, for being the chairman of the assessment committee and for the high-level conceptual advice.

Furthermore, I would like to thank the Client Support department of COMSOL Multiphysics for the long discussions and file exchange. They helped me a lot become better in numerical modelling using the specific platform.

Last but not least, I would like to thank my parents and my brother for their love and support during my whole two-year long MSc programme. Finally, all the amazing people that I met in Delft during the last two years, my friends, my classmates and the jazz band ‘French Fry And The Broke Refugees’. You guys made it special for a lifetime!

Dimitris Kaltsas

Delft, August 2016

Contents

List of Figures

List of tables

Nomenclature

Upper case Latin symbols:

A	Biot coefficient related to stiffness	Pa
$\mathbf{A_i}$, $\mathbf{B_i}$, $\mathbf{C_i}$	Various polynomial coefficients	
C	Cauchy elasticity tensor	Pa
C_{air}, C_f, C_s, C_m, $C_{f,eff}$	Compressibility values (air, fluid, solid, overall compressibility of the medium and effective compressibility of the fluid)	m^2/N
C_i	Various constants	
E, E_u	Young's Modulus (drained and undrained conditions)	Pa
G, G_{max}, G_s	Shear moduli	Pa
H_s	Dynamic coefficient based on density and stiffness	
I	Identity matrix	
K,K_u	Bulk modulus (drained and undrained conditions)	Pa
M	Pore shape factor	
$\mathcal{M}$	Biot constant	
N	Biot coefficient related to stiffness	Pa
OCR	Overconsolidation ratio	
P	Biot constant related to stiffness	Pa
Q	Biot constant related to stiffness	Pa
Q_m	Mass source term	kg/m^3
R	Biot coefficient related to stiffness	Pa
$\boldsymbol{\mathcal{R}}$	Viscous drag forces vector	$kg*m^2/s$
S	Degree of saturation	
S	Spatial derivative matrix	
S_p	Storativity	
S_{Pi}	Slowness	s/m
U	Radial displacement of the fluid	m
$\mathbf{U^R}$	Fluid displacement relative to the solid	m

Lower case Latin symbols

a	Dimensionless parameter for the 1D solution	
b	Dimensionless parameter for the 1D solution	
b	Body force vector	N
b_0, $\hat{b}$	Damping coefficient (real and complex value)	Ns/m^4

c	Wave velocity	m/s
c_{Pi}	Phase velocity	m/s
d_0	Dynamic coefficient based on density	
d_f	Dimensionless parameter for the 1D solution	
e	Void ratio	
ϵ	Fluid dilatation	
eps	Numerical constant	
f	Frequency	Hz
$\mathscr{f}$	Stretching function	
g	Acceleration of gravity	m/s^2
$\mathbf{k}$	Hydraulic conductivity	m/s
k_{eq}	Equivalent wave number	
k_0	Earth pressure coefficient	
$\mathscr{k}$	Permeability (no viscosity included)	m^3s/kg
ℓ	Wave length	m
m_v	1D compressibility	m^2/N
m	Tortuosity coefficient	
$\mathbf{m}$	Unit vector	
n, n'	Porosity, Effective porosity	
$\mathbf{n}_\xi$	Direction of the unit vector	
$\bar{n}$	Exponential coefficient	
p, p_0, $\hat{p}$, p_{atm}	Pressure, Pressure amplitude, Complex pressure, Atmospheric pressure	Pa
p'	Mean effective stress	Pa
r, r_0	Radius, Cavity initial radius	m
t	time	s
u	Radial displacement of the solid	m
$\mathbf{u_D}$	Darcy velocity field	m/s
$\mathbf{w}$	Fluid velocity relative to the solid	m/s

Greek symbols

α	Biot coefficient
β	Nonlinear curvature exponential coefficient
β_{Pi}	Amplitude ratio
γ	Shear strain
γ_{ref}	Reference shear strain

γ_i	Complex wavenumber	
δ_{ij}	Kronecker delta	
ε	Volumetric strain	
$\boldsymbol{\varepsilon}$	Strain tensor	
ε_{el}^{II}	Second invariant of the elastic deviatoric strain tensor	
η	Dynamic viscosity of the fluid	$N*s/m^2$
$\boldsymbol{\kappa}$	Permeability	m^2
λ	First Lamé constant	Pa
μ	Second Lamé constant	Pa
ν, ν_u	Poisson ratio (drained and undrained conditions)	
ρ, ρ_f, ρ_s	Average density, density of fluid, density of solid	kg/m^3
ρ_{11}, ρ_{12}, ρ_{22}, $\hat{\rho}_{11}$, $\hat{\rho}_{12}$, $\hat{\rho}_{12}$	Coupled density terms (real and complex values)	kg/m^3
$\hat{\rho}_{eq}$	Equivalent density term	kg/m^3
ρ_c	Complex density term (used by COMSOL Multiphysics)	kg/m^3
$\boldsymbol{\sigma}$	Total stress tensor	Pa
$\boldsymbol{\sigma'}$	Effective stress tensor	Pa
σ_x	Step function (for PML)	
τ	Tortuosity	
τ_c	Tortuosity factor	
ϕ	Potential function for the PDE solution	
ϕ_i	Nonlinear semi-empirical factors	
ψ	Potential function for the PDE solution	
ω	Angular frequency	rad/s
ω_c	Rollover frequency	rad/s

Abstract

The pressuremeter test is one of the most popular in-situ soil testing methods. Developed in the 1950s in France, the test has evolved throughout the past decades and was built into a cone resulting in a cone pressuremeter device (CPM). A proposed extension of the test involves time dependent pressurisation of the device resulting in wave propagation in the soil. Therefore, the dynamic behaviour can be determined. The possible applications of this extension include the response of an offshore monopole to dynamic loading and liquefaction analysis. The present research work deals with the modelling of the dynamic version of the pressuremeter test. The soil where the test was assumed to be conducted was saturated sand. Therefore, it was modelled as a porous medium, following the poroelastic theory by Biot (1956). The latter was based on the consolidation theory (Biot, 1941).

First, the poroelastic behaviour is thoroughly described. Through one-dimensional analytical solution on an infinitely long soil bar the physical mechanism is explained. Biot (1956) concluded that there are two compressional waves propagating in the porous medium. Therefore, the wave that is generated by the oscillating boundary of the soil bar consists of two components, whose characteristics were quantified. It was found that because of the second compressional wave the solid and fluid move out of phase. This kind of wave is a result of a diffusion process and is strongly attenuated. Additionally, a parametric investigation showed that the permeability and the degree of saturation of the medium are determining for the response, whereas the porosity does not play such a significant role. Especially for the degree of saturation, the response of a nearly saturated medium was compared to the response of a saturated one. It was observed that the presence of entrapped air in the pores amplifies the response much. However, the amplitude converges fast to a certain value when the degree of saturation decreases further than about 95%.

Afterwards, the cavity expansion problem in poroelastic medium is solved analytically in order to simulate the dynamic cone pressuremeter test. Various formulations of the equations of motion found in the literature were compared, and the effect of the respective assumptions on the response was evaluated. The poroelastic response in the frequency domain was compared to the linear elastic response assuming both drained and undrained conditions. It was found that the poroelastic response lies between the two extremes, which are the drained and the undrained linear elastic responses, both in amplitude and phase shift. Further investigation on more response features, such as the pore pressures, the stiffness, the cavity radius and the energy dissipation was conducted in the frequency domain. It is of high interest that the pore pressures can amplify to values larger than the pressure applied on the cavity and that the cavity radius can lead to completely different resonance frequencies.

In order to incorporate more complicated and more realistic soil modelling, the cavity expansion problem was solved numerically as well with the aid of the finite element platform ‘COMSOL Multiphysics’. First, the numerical poroelastic solution in the frequency domain was compared to the analytical. A perfect match was observed between the two. Additionally, it could be concluded that the very common assumption of negligible relative acceleration of the fluid with respect to the solid can be valid for the operational frequencies of the CPM test. Furthermore, the solution was obtained in the time domain as well. The amplitude of the time-domain response matched with the one predicted by the frequency-domain spectra. Based on that reliable result, the soil constitutive

behaviour was enhanced with the nonlinear hyperbolic law for the shear modulus which was implemented by manual coupling of the ‘Solid Mechanics’ and the ‘Darcy Law’ interfaces in COMSOL Multiphysics. In order to check the coupling and the nonlinear behaviour, direct simple shear tests were conducted on a single element. After the single element was ensured to perform according to the analytical expression of the hyperbolic law, the nonlinear analyses were conducted in the time domain for discrete frequencies. It was observed that the nonlinearity gives rise to third-order harmonics which is similar to the behaviour obtained for a so-called Duffing oscillator, being a mass-spring system with a cubic stiffness term. The response was computed at discrete frequencies. The maximum displacement values as well as the pore pressures of the steady-state response were calculated over frequency by means of interpolation for various nonlinear parameters found in the literature. The effect of nonlinear parameters, applied pressure and hydraulic conductivity was evaluated. In addition, the nonlinear poroelastic analysis was compared to the nonlinear elastic analysis assuming a single phase material. It was found that as nonlinearity becomes more dominant, the poroelastic effects maximize. Additionally, during the accomplishment of the test, it was observed that COMSOL Multiphysics is a tool which cannot deal with severe nonlinearities. On the other hand, the dynamic cone pressuremeter test itself can be an efficient tool to detect nonlinear behaviour.

1

Introduction

The ground behaviour under loading has always been a determining factor of the design of all civil engineering activities. Either soil or rock, or even ground materials that are difficult to be categorised, always affect the overall behaviour of a structure. Therefore, geotechnical engineers always strive to determine the behaviour of the ground under any change of its state. A well-established tool to achieve this is the representation of the ground features by parameters. The latter are determined usually by conducting tests, either in situ or laboratory, so that the parameters can be determined by the behaviour of the ground under examination. In the design phase, the parameters are the input to predict the ground behaviour when a project is going to be realised. The present work focuses on one particular in-situ test for the determination of the soil parameters, the Cone Pressuremeter Test (CPM) and more specifically the dynamic version of it. The above described process will be followed reversely: The ground will be modelled respectively, using selected parameters in order to thoroughly describe its response and derive according conclusions. The latter will focus on the influence of the ground parameters, the loading frequency, the dynamic consolidation (if any) and finally the nonlinearity.

1.1 Motivation and scope of the research

The pressuremeter test has always been conducted in a static way, meaning that the pressure is applied 'slowly enough' to allow for static analysis and extract static parameters. Fugro GeoServices BV is currently planning to realise a dynamic version of the test. The initiation of the present thesis project was driven by this special development of the test. In particular, the applied pressure can vary in time, so that dynamic soil properties can be determined as well. Therefore, the response should be analysed using methods that describe the wave propagation in the surrounding soil, rather than static analysis. Apart from that, this type of loading cannot be characterised neither as undrained nor as drained and therefore, the hydraulic behaviour of the pore fluid needs to be studied as well. As a result, the soil model becomes quite complex, combining dynamic equations that couple the solid material behaviour with the fluid flow. In other words, the soil is treated as a porous medium. This representation allows for investigation of further effects such as the partial saturation of the pores, nonlinear material behaviour and damping.

In this framework, the present thesis project is realised in order to provide a detailed explanation of the physical processes which are expected to take place during the execution of the test and therefore to validate existing assumptions that are taken into account.

In the following section the main components of the problem will be analysed. These are the cone pressuremeter test itself, the theory of poroelasticity and the cavity expansion theory, which is the basic theory of the cone pressuremeter test. A short historical recursion will be provided along with the highlights of the research conducted so far, forming the 'state of the art'. In other words, the background information is provided before the proposed model is presented.

1.2 Background information – State of the art

1.2.1 The pressuremeter test

The history of the pressuremeter goes back to the 1950s when independent developments took place in France and Japan. These developments led to the use of probes in ground investigation for foundation design. Although the first documented evidence of the pressuremeter is that of Kogler in 1933, the term 'pressuremeter' was first used by Ménard, who patented this testing equipment in 1955 (the Ménard pressuremeter or MPM). In the 1970s, self-boring pressuremeters (SBP) were developed in France and the UK in order to determine directly ground properties, such as in-situ stress, stiffness and strength. Theoretically, the SBP causes no disturbance in the surrounding soil because it can be drilled into the ground. In practice, there is always ground disturbance, though it can be kept to a minimum through the SBP. The latter requires careful installation, which was overcome in the 1980s with the development of the pushed-into-ground pressuremeter (PIP). To sum up, the prebored pressuremeters (PBP) are placed in prebored pockets, while the pushed-in pressuremeters (PIP) are inserted and displace the ground. Self-bored pressuremeters (SBP) replace the ground by using a drilling system within the probe, allowing the probe to be drilled in the test position. (Clarke, 1995)

Baguelin et al. (1978) referred to the pressuremeter probe as a device that applies hydraulic pressure through a flexible membrane to the walls of a borehole. This development helped the analysis and interpretation of the pressuremeter tests. Mair and Wood (1987) further restricted the definition of a pressuremeter to a cylindrical device and this definition is recognised internationally by the International Society for Soil Mechanics and Foundation Engineering (ISSMFE):

'A pressuremeter is a cylindrical probe that has an expandable flexible membrane designed to apply a uniform pressure to the walls of a borehole'.(Clarke, 1995)

In the 1980s, Fugro Engineers developed the Fugro Cone Pressuemeter (CPM) assisted by Cambridge In-situ, UK, driven by unsatisfactory experience with other types of pressuremeters. The objectives for such development were the following (Ballivy, 1995):

- The installation of the tool should be performed using routine CPT equipment and associated personnel.
- The installation and execution of the test should be operator independent, resulting in repeatable test results.
- An electric piezo-cone penetrometer should be included to the device in order to provide with clear identification of the test zone.
- Theoretical analysis and research had to indicate that reliable soil parameters can be obtained, despite the large degree of initial soil disturbance.

Withers et al. (1986) have provided some guidelines with respect to the interpretation of the results. These are the following:

- ✓ The electric piezo-cone penetrometer identifies the soil type in which the pressuremeter test is performed.
- ✓ The soil which was situated at the location where the cone is installed has been fully displaced by the penetrometer. In the present work, this feature will not be taken into account. The soil will be assumed undisturbed until the membrane starts inflating.

- ✓ The expanding part of the pressuremeter module has a large length over diameter ratio to ensure a predominantly radial expansion of the membrane during inflation. This characteristic is taken into account by assuming no edge effects on the domain under examination.
- ✓ The membrane is inflated to a large radial strain (ε_{rr} = 0.50) to ensure that the limit pressure is achieved at full inflation.
- ✓ Special attention should be paid both during design and during operation to ensure that accurate pressure and strain data are obtained.

For the present analysis, the second guideline will not be taken into account. The soil will be assumed undisturbed until the membrane starts inflating. On the other hand, the third guideline will be accounted for by assuming no edge effects on the domain under examination.

The main advantage of the pressuremeter test is that it is able to assess the ideal condition in which the ground is loaded from the in-situ stress conditions. This allows prediction of the in-situ stress-strain response by observing the deformation caused by loading of the pressuremeter. Thus, the parameters obtained, which include in-situ stress, stiffness and strength are a function of the type of the probe, the method of installation and the method of testing. Nevertheless, they depend on the chosen method of analysis and interpretation. Another significant advantage of the pressuremeter test is that it can be applied to almost any type of ground, from soft soils to hard rocks, as it is presented in Table 1.1 for different types of pressuremeters. On the other hand, limitations among the different versions/developments of the pressuremeter exist. For instance, the theories of cavity expansion, which will be described in the next section, do not apply to the prebored pressuremeter (PBP) and pushed-into-soil pressuremeter (PIP) because of disturbance during installation. Additionally, results from self-bored pressuremeter cannot be used in the Ménard design methods, because of the different installation method. (Clarke, 1995)

Table 1.1. The applicability of pressuremeters to ground conditions (Clarke, 1995)

Ground type	PBP	SBP	PIP
Soft clays	Very good	Very good	Very good
Stiff clays	Very good	Very good	Very good
Loose sands	Good, with support	Very good	Very good
Dense sands	Good, with support	Good	Moderate
Gravel	Moderate, by driving	Not possible	Not possible
Weak rock	Very good	Good	Not possible
Strong rock	Very good	Not possible	Not possible

The proposed extension of the pressuremeter test is its dynamic version. This development allows for determination of the cyclic ground response to dynamic load, for instance in case of a seismic event or the wave load acting on an offshore monopile. More specifically, possible soil characteristics that can be determined are the dynamic stiffness and strength, the permeability and damping properties.

Figure 1.1 presents a typical installation of the cone pressuremeter. In general, the installation consists of three parts: The probe, the control unit and the connections between them. The present work will focus on the pressuremeter module, or test section, which will be assumed of infinite length or the analyses, so as vertical restrictions and disturbance will not influence the measurements.

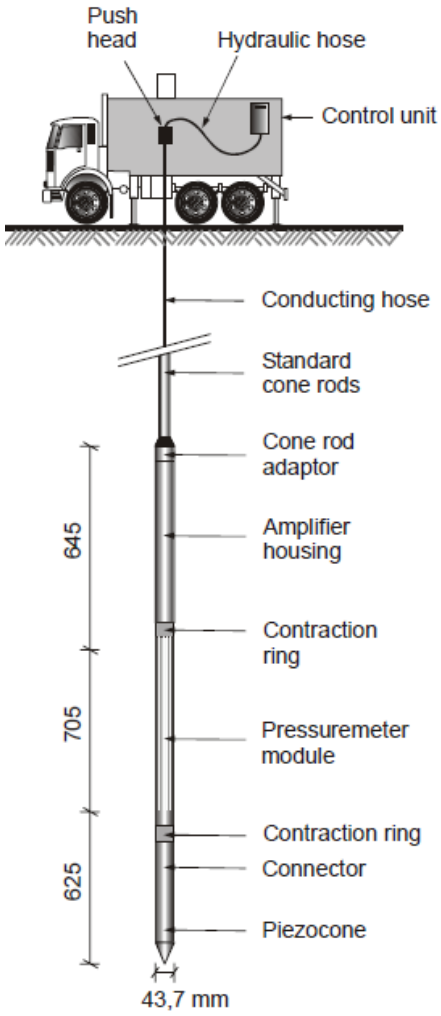

Figure 1.1. Typical cone pressuremeter installation and its parts (Schnaid, n.d.)

In Figure 1.2 the probe of the Cambridge cone pressuremeter is illustrated. The picture provides with more details the structure of the probe. The membrane part of the probe can be similized by a Chinese lantern. The probe is in total 2m long and 43.7mm in diameter. The test section is 50cm long and it is covered with an elastic membrane. The membrane has the ability to be inflated. The pressure applied and the displacement of the membrane are monitored by transducers in the instrument itself (Whittle, 1999). The displacement transducer is situated at the centre of the expanding cavity, and therefore, the variables measured at the cavity boundary during the present work will refer exactly to this point.

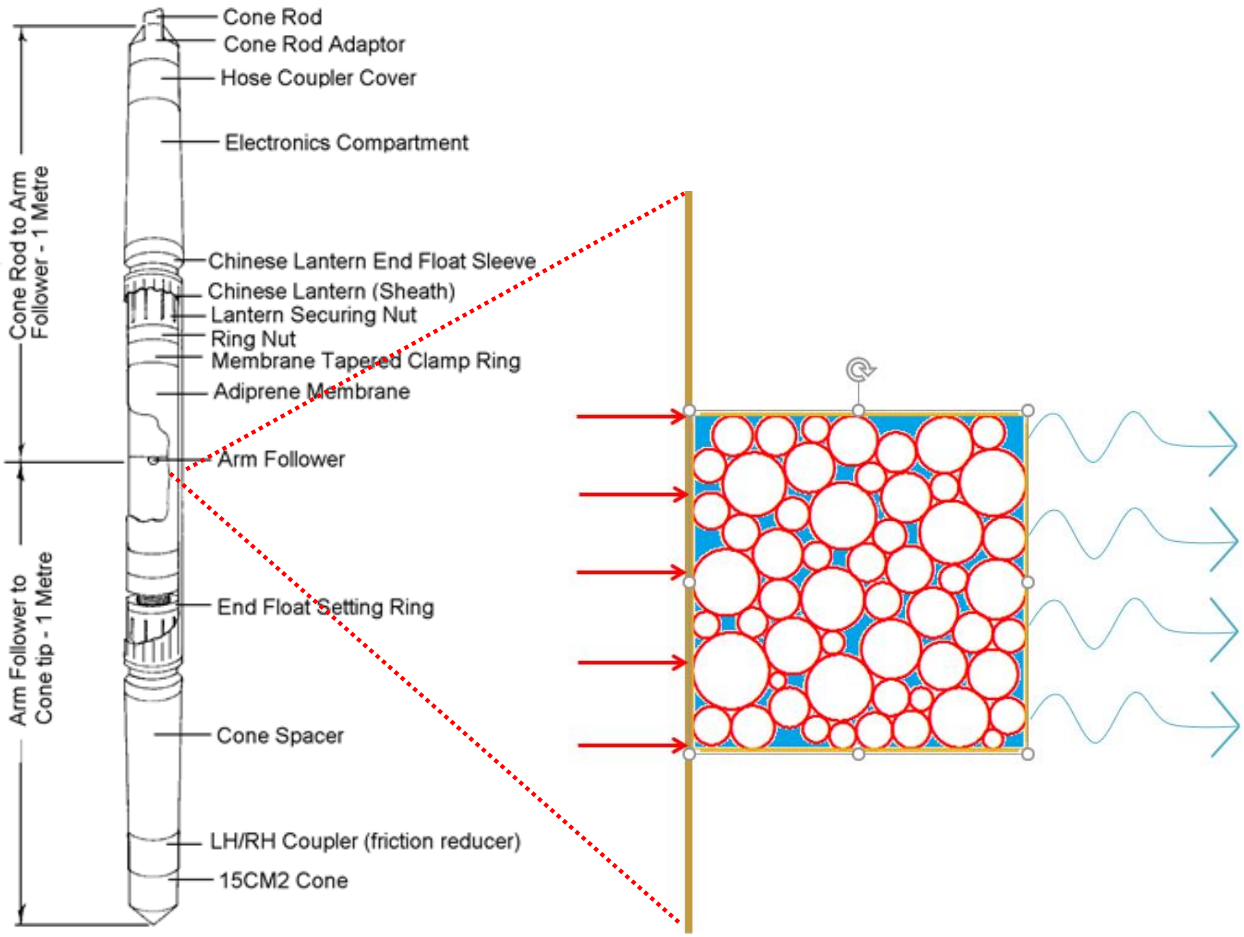

Figure 1.2. The probe of the cone pressuremeter test (Whittle, 1999) and the poroelastic soli element

1.2.2 The theory of poroelasticity

The term poroelasticity consists of: a) the word “pore” (from the old French ‘pore’, the Latin ‘porus’ and the ancient Greek ‘poros’) meaning initially a tiny opening in the skin and extensively any small opening allowing passage and b) the word elasticity (from French ‘élasticité’, modern Latin ‘elasticus’ and ancient Greek ‘elastos’) meaning ductile, flexible. Poroelasticity is used to describe the behaviour of a material, which is porous, containing namely tiny passages which allow for fluid flow and is elastic, in a sense that every deformation of the material is reversible. Porous materials can be either granular materials or porous solid materials. As can be seen in Figure 1.3, sand is a granular material whereas a bone with osteoporosis is a solid material containing pores. Such materials can be found everywhere; filters, plants, living bodies, bones, and rocks are examples of porous materials. Soils are also a great example of such materials, consisting of a solid grain matrix and pore space which is filled with fluid, usually water and/or air. The pore space allows fluid flow in case the pores are interconnected. As a result, the behaviour of the porous material, or, better, the porous medium, is governed by the stiffness of the solid particles and the behaviour of the fluid in the pores (Verruijt, 2014).

The theory of porous materials saturated by a viscous fluid was first described in the three dimensions by Biot (1941) on the basis of the consolidation theory developed by von Terzaghi (1925) for the one-dimensional case. In the original consolidation theory by Terzaghi the pore fluid and solid particles were assumed to be completely incompressible. As a result, any deformation of the porous medium is a result

of particle rearrangement, and volumetric changes must be accompanied by pore water expulsion (Verruijt, 2010).

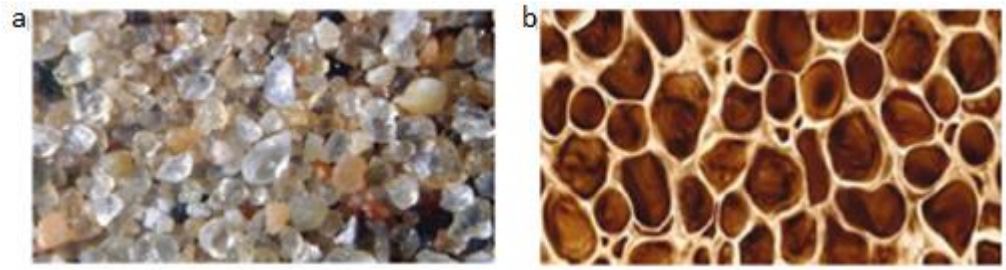

Figure 1.3. Porous materials: a) Sand b) Bone with osteoporosis

On the other hand, according to poroelasticity, the constituents of the porous medium, which are the solid particles and the pore fluid, form the two interacting phases of the material and they are both compressible. Hence, material deformation is also allowed. Poroelasticity was first established by Biot as a quasistatic theory, taking into account no inertia terms (Schanz, 2009). Later on, Biot (1956) extended the poroelastic theory to include dynamic phenomena. He assumed that the fluid may flow relative to the solid matrix causing friction to arise. The fluid flow is assumed to be of the Poisseuille type. It was pointed out by Kirchhoff that this is valid only below a certain frequency which depends on the kinematic viscosity of the fluid and the size of the pores. Therefore, Biot distinguished his theory accordingly to low and high-frequency ranges. The present work, like almost every application in Geomechanics, will deal with the theory in the low-frequency range. Biot's theory results in the development of a second compressional wave which relates to the diffusion process and is highly attenuated. This wave results from the fluid phase inertia. The latter varies from the solid phase inertia and this provides the system with one more possible motion (van Dalen, 2013). On the other hand, the compressional wave of first kind is a true wave. The dispersion is practically negligible with a phase velocity slightly increasing with frequency. The physical meaning of the phase velocity will be explained thoroughly later in this report.

Further assumptions by Biot include that the size of the unit volume elements are large compared to the pores. In addition, with the term 'pores' only the interconnected pores are included, meaning that isolated voids where no flow occurs are regarded as part of the solid phase. In Chapter 2.1 the Biot theory will be solved analytically in one dimension for a soil bar following the notation by Verruijt (2010).

Although Biot was the developer of poroelastodynamics, the basis to this theory was laid by Frenkel (1944). In fact, both Frenkel (1944) and Biot (1956) developed the same theory. Deresiewicz and Skalak (1963) connected these two theories with each other. An extension of the theory of poroelastodynamics to nearly saturated porous media was conducted by Vardoulakis and Beskos (1986). In order to study the effect of entrapped air in the pores of the medium, this extension will be consulted.

More recently, the theory of poroelasticity is extended to solve more complex three-dimensional problems, such as the transient response of a circular (Senjuntichai and Rajapakse, 1993) and cylindrical lined cavity in a poroelastic medium (Gao et al., 2013). These two papers provide a solution according to Biot's theory in non-dimensional parameters. Although the aforementioned research by Senjuntichai and Rajapakse (1993) and Gao et al. (2013) provides an analytical solution in cylindrical coordinates, it will not be adopted by the present report, because it solves slightly different problems. Hence, the solution derived in Chapter 2.2 follows the study by Abbas and Abd-alla (2012). The latter derived an analytical solution for two-dimensional wave propagation in a poroelastic infinite circular cylinder, which applies to the case of the pressuremeter test as well. To this solution the damping term according to Biot (1956) is

added and therefore a set of equations of motion is proposed, which models the linear poroelastic behaviour of the ground during the dynamic pressuremeter test. In general, the case is formulated by three variables:

- Displacement of the solid matrix (u)
- Displacement of the pore fluid (U)
- Pore pressure (p)

These three variables - and respectively three governing equations - can be reduced to two, leading to a simplified set of equations. This acts in favour of numerical calculations, since the computational memory and time consumed reduces significantly, as the degrees of freedom decrease as well. In Chapter 2.2 the various formulations, namely the 'u-p-U formulation', the 'u-U formulation' and the 'u-p formulation', are presented and compared with each other. The proposed analytical solution is based on the u-U formulation of the governing equations.

Additionally, Zienkiewicz et al. (1999) conducted extensive research on poroelastodynamics. They distinguished the low and high-frequency range as well and provided solutions for both. The main feature for the low-frequency solution is that within this range the relative displacement of the fluid and the solid can be neglected. This assumption will be evaluated in the present research. The proposed methodology by Zienkiewicz et al. (1999) is highly appreciated nowadays and applied by the engineering society.

Although the poroelastic model is a more accurate representation for the soil response than the linear elastic model, as it will be shown later on, it leads to a rather simplified solution, with respect to the solid phase. The drained particles are assumed to exhibit a perfectly linearized stress-strain relationship. However, in reality, the soil behaviour is more complicated. As a result, the stress strain relationship will be modified to incorporate nonlinearity. According to Richards, Hall and Woods (1970): 'The process of obtaining representative values for the critical soil properties is probably the most difficult part of the design study'. This is a result of the dependence of the soil properties on various soil parameters. Hardin and Drnevich (1972), who developed the popular nonlinear Hyperbolic law, clearly state that parameters such as the strain amplitude, the state of effective stress and the number of cycles can be determinant for the soil properties, and therefore, the soil response. For many problems the shear stress-strain relation is the most important (Hardin and Drnevich, 1972).

1.2.3 The cavity expansion mechanism

The basic theory to approach the pressuremeter test in the present work is the cavity expansion theory. An infinitely long cylindrical cavity is considered, which can approximate the device, although there are end effects, because in reality the length is finite and the cylindrical membrane is restrained in each end (Baguelin et al., 1978).

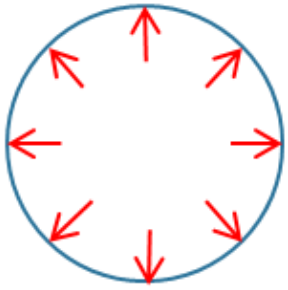

Figure 1.4. Cylindrical cavity expansion (Verruijt, 2010)

The deformed element is cylindrically symmetrical, meaning that the basic coordinates are the radial (r) and the tangential (θ) and consequently no shear occurs in these directions. In addition, the normal stresses σ_{rr} and σ_{tt} are independent of the coordinate θ. The deformed element is plotted in Figure 1.5.

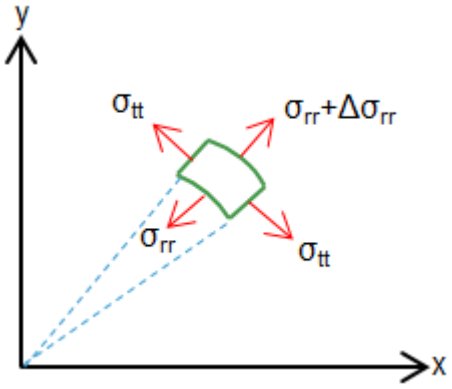

Figure 1.5. Element in cylindrical coordinates and stresses acting on it at the deformed case (Verruijt, 2010)

The general solution of the cavity expansion problem both static and dynamic is presented in the Appendix. The static solution generally results in reduction of the displacement over distance according to a factor of 1/r. On the other hand, if the load on the soil caused by the expanding cavity is time dependent, an inertia term must be introduced in the equilibrium equation. As a result, the displacement reduces over distance by a factor of 1/√r, in contrast to the static displacement. This means that the displacements attenuate later according to a dynamic analysis than according to a static one. An example is illustrated in Figure 1.6. It can be observed that at 10m away from an expanding cavity the dynamic radial displacement is almost twice as large as the static value.

The above expression for the displacement is the analytical solution of the cylindrical cavity expansion problem assuming linear elasticity and will be used later in this report for the comparison of the linear elastic response with the poroelasticity.

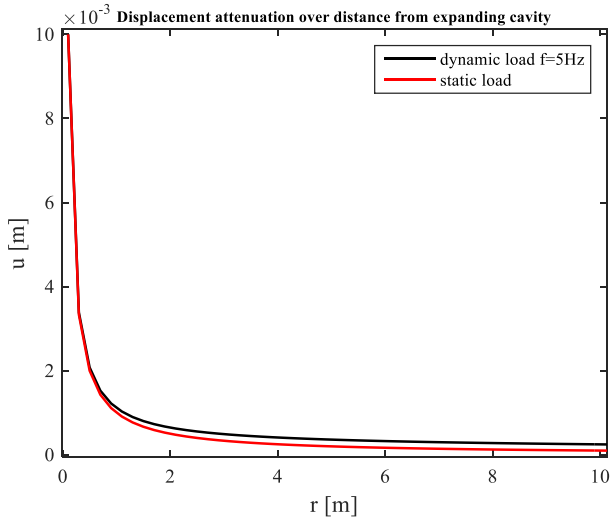

Figure 1.6. Displacement over distance from expanding cavity (dynamic vs. static load)

1.3 Research objectives

In Section 1.2 the main components of the problem which is analysed in the present research have been explained. These components will be combined to model the dynamic version of the pressuremeter test and answer the following research question:

'How does the porous medium respond to the dynamic pressure applied by the cone pressuremeter test?'

The question above is the main research question which is attempted to be answered. To accomplish this, it should be divided into partial sub-questions according to the different problem aspects.

In general, the present work analyses the dynamic version of the pressuremeter test when this is conducted in a poroelastic medium. The probe is assumed to be inserted in a specific depth and the cavity of the pressuremeter is assumed to expand sinusoidally. The test is realised at low frequencies - usually lower than 5Hz - so the results' comparison will focus on that range of frequency. However, a larger frequency range is studied so that according conclusions can be drawn. Consequently:

'Is poroelasticity a more sensible option for such frequencies or is a single-phase elastic model enough?'

According to Biot's theory which is the basis for the present work, there are two compressional waves propagating in a porous medium. The question that arises from the existence of the additional compressional wave is this:

'How does the slow compressional wave influence the response and how much does the latter differ from the response according to linear elasticity?'

The special case of nearly saturated medium will be studied following the aforementioned extension of Biot's theory by Vardoulakis and Beskos (1986). Since the entrapped air in the pores is expected to influence the response, the following question arises:

'What is the influence of the degree of saturation on the response of the porous medium? What are the drainage conditions that more accurately represent the physical process for various frequencies?'

The assumption taken into account by Zienkiewicz et al. (1999) for similar problems to the one studied in the present research that the acceleration of the fluid relative to the solid can be neglected for the low-frequency range is evaluated. An answer will be provided to the following sub-question.

'Is it sensible to neglect the acceleration of the pore fluid relatively to the solid matrix at the operational frequency range of the dynamic pressuremeter test?'

Subsequently, the treatment of the soil as a two phase material is physically sensible and common in engineering practice. More specifically, the extension of the consolidation theory to dynamic phenomena has been used and is being continuously used to represent the wave propagation in the ground. In the present project it will be adopted as well to simulate the behaviour of sandy soil to a recent dynamic extension of the pressuremeter test.

Finally, in order to add nonlinearity to the constitutive equation of the solid part, the Hyperbolic law which will be used in the present study. It assumes dependency of the shear modulus on the shear strains. The question arising is:

'To what extent does nonlinearity influence the soil behaviour compared to the linear analysis and how can nonlinearity be detected and quantified using the dynamic CPM test?'

In order to answer this question, the Hyperbolic nonlinear law will be used. This model makes use of a strain-dependent stiffness modulus and results to less stiff behaviour with increasing strain. In the present research, the secant shear modulus (G) is assumed strain-dependent. More specifically, the shear modulus has an initial value which is dependent on the initial stress regime through the mean effective stress, according to Hardin (1978). Thus, it is dependent on the depth of the domain examined, which is the depth of the insertion of the probe of the pressuremeter. Generally, the initial (maximum) shear modulus value is dependent on more parameters, such as the geological history, but these lie beyond the scope of the present analysis. The value of the shear modulus is reduced as the strain increases through a shear strain invariant. During unloading, the stress-strain curve follows the same path, maintaining an elastic behaviour. This kind of soil behaviour is coupled with Darcy's flow of the pore fluid to determine the nonlinear poroelastic response in harmonic loading.

The path to answer the aforementioned research questions is explained briefly in the following section.

1.4 Overview of the report

In the first part of the present work (Chapter 2) the analytical solutions to poroelastic problems are derived. Initially, the wave propagation in a porous, one-dimensional, infinitely long poroelastic soil bar is investigated. After the basic principles of Biot's theory are presented, the derivation of the analytical solution for one-dimensional problems in Cartesian coordinates described in Verruijt (2010) follows. Although the rest of this research is conducted in cylindrical coordinates, the analytical solution in Cartesian coordinates is the first step to gain insight into how the equations of motion are built up. Moreover, Verruijt (2010) provides a detailed explanation of each term of the equations, and the corresponding link to the physical phenomena. In addition, parametric analysis in one dimension leads to identification of the special features of poroelasticity, such as the phase velocity of each propagating wave. What is more, the significant effect of the fluid compressibility, in other words, of the air content in the pores, is investigated.

Later on, the two-dimensional cavity expansion problem will be solved in cylindrical coordinates, in order to simulate the pressuremeter test. The equations of motion are solved with the aid of Hankel functions. The solution can be expressed in terms of displacement of the solid particles (u), displacement of the fluid (U) and pore pressures (p) and every possible combination of two out of the three aforementioned variables. Therefore, the so-called 'u-U' and 'u-p' formulations of the equations of motion are derived and compared to respective formulation found in the literature. Especially for the 'u-p formulation' which is the most convenient for numerical simulations for reasons that are explained later, the governing equations are compared to the set used by COMSOL Multiphysics, a software package which is used to accomplish the numerical approximation of the cavity expansion case in a poroelastic medium. COMSOL Multiphysics makes use of a set of equations in the frequency domain which are coupled in a slightly different way to the proposed solution. Hence, the validity of the constitutive equations used by COMSOL Multiphysics are checked by comparison with the formulation derived in the present work. The same set of governing equations is compared to the derived equations by Zienkiewicz et al. (1999), which is commonly used in geotechnical engineering. Zienkiewicz et al. (1999) make the assumption that for the low-frequency range, the relative acceleration of the fluid and the solid phase of the material can be neglected. Last but not least, the derived equations are expressed in the time domain, for further analysis using more complex soil models, such as the nonlinearly behaving soils.

In Chapter 3 the results of the analytical solutions are presented and discussed. Initially, a parametric investigation of the one-dimensional case (infinitely long soil bar) is conducted to quantify the influence of the soil parameters on the response. In addition, this is a way to identify the two compressional waves described by Biot (1956) and their features. Moving to the cylindrical problem (cavity expansion), a parametric analysis is conducted in the frequency domain where the amplitude and phase shift spectra are investigated for varying soil conditions. The cylindrical poroelastic solution is compared with the linear elastic solution derived in the Appendix for both drained and undrained conditions and according conclusions are drawn. What is more, results of variables such as the dynamic stiffness and the energy dissipation are presented in the frequency domain. The influence of the radius of the cavity is also investigated.

In Chapter 4 the development of the numerical model is thoroughly explained. First, the setup for the frequency-domain analyses is described. It has been accomplished using the 'Poroelastic Waves' interface of COMSOL Multiphysics. On the other hand for the time-domain analyses the 'Poroelasticity' interface was used, due to the limitation of the 'Poroelastic Waves' interface to conduct time-domain analysis. In Chapter 4, linear elastic analyses in the time domain are initially conducted to verify the response predicted by the frequency domain, after a detailed explanation of the FE model is given. Afterwards, the stages of the application of the gravitational load and the stress initialisation are explained, as well as the Hyperbolic model. The performance of COMSOL Multiphysics on capturing the nonlinear material behaviour is tested by modelling pure shear on a single element. Various boundary conditions and interface couplings were applied to accomplish this. Finally, the coupling between the 'Poroelastic' with the 'Darcy law' interface is proven to be the most efficient.

In Chapter 5 the results of the numerical solution are presented. Initially, the response is investigated in the frequency domain to prove a match between the numerical solution with the analytical. In addition, the aforementioned assumption expressed by Zienkiewicz et al. (1999) is evaluated. The deviation in the response is minor, and therefore the assumption is indeed valid for the frequencies under examination. Afterwards, linear elastic analyses in time domain are conducted using a constant shear modulus, dependent on the mean effective pressure. The soil exhibits a more stiff behaviour as the depth grows. For a specific depth, nonlinear analysis are then accomplished to compare the poroelastic with the elastic nonlinear response. The influence of the nonlinear parameters, the applied pressure, the hydraulic conductivity and the frequency are examined, providing a concrete answer to the research questions stated in this chapter.

A schematic overview of the types of analyses conducted and the respective formulation used is given in Figure 1.7.

To sum up, the present study provides a prediction of the ground response to the cylindrical dynamic excitation caused by the cone pressuremeter test. The proposed model can be a first approach to what an engineer can expect when the test is conducted in saturated sand. However, the model has limitations which can be overcome during a possible future extension of the present study. First, the model assumes a 'wished in place' installation while in fact during installation of the probe an infinitely large radial strain applies at the central axis of the probe resulting in a plastic region directly around the probe. Second, it does not take into account ground anisotropy and variability. The soil is assumed to be homogeneous and isotropic. Therefore, soil plasticity and more advanced soil models could be used to capture more complex soil behaviour. All these features compose a recommendation for future research.

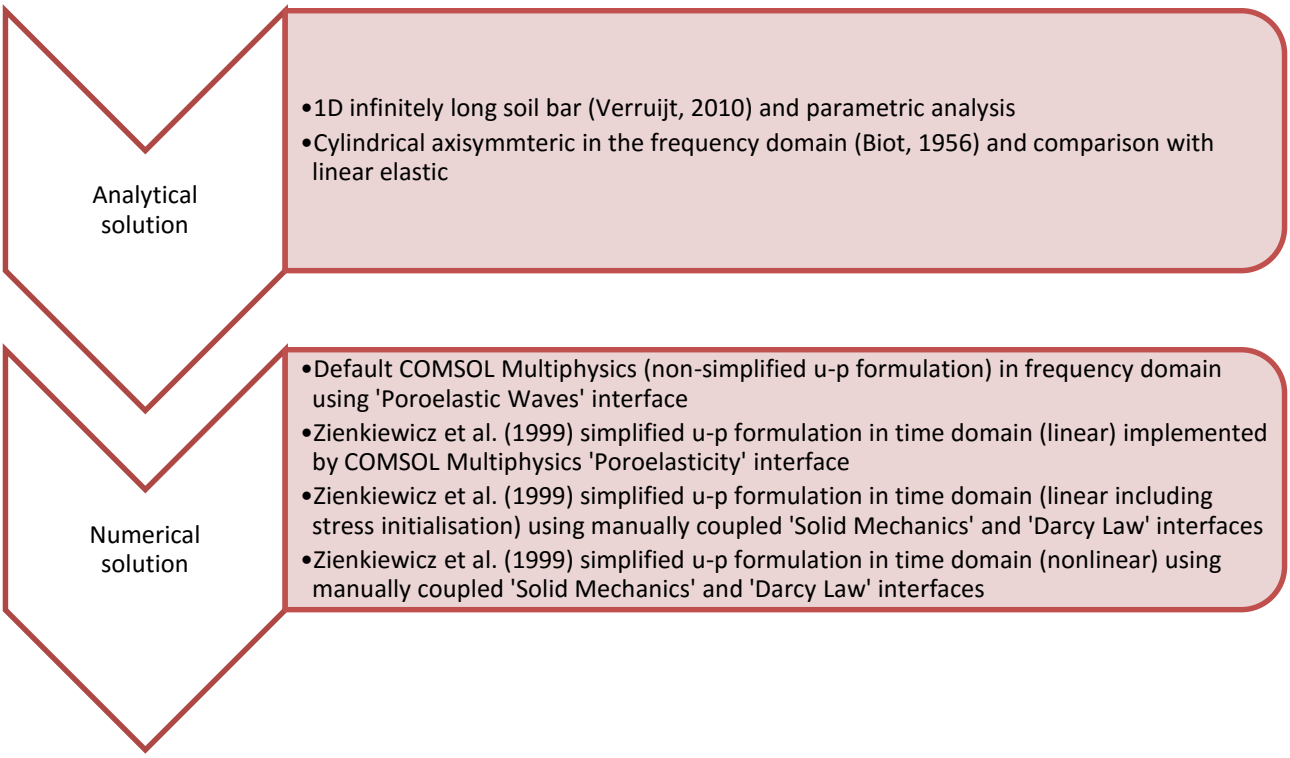

Figure 1.7. Overview of the analyses and the respective formulations of the governing equations

2

Mathematical formulation of the dynamics in porous media

This chapter deals with the development of the governing equations that represent the wave propagation in linear poroelastic medium and their solution. As a starting point, an infinitely long soil bar is subjected to sinusoidal load. This one-dimensional representation is convenient in order to gain insight into Biot's theory of poroelasticity by explaining term-by-term the governing equations. Afterwards, the same set of equations is transferred to the polar coordinate system in order to incorporate the cavity expansion mechanism, which is representative for the cone pressuremeter test. Assumptions expressed and taken into account by various authors are verified in this chapter as well. Additionally, different independent variable sets are compared and the connection between the formulations of the existing literature is clarified. Finally, because both an analytical and a numerical model are developed in the present research, the governing equations are formulated both in the frequency and the time domain.

2.1 One-dimensional wave propagation in linear poroelastic medium

The response of an infinitely long 1D soil bar subjected to sinusoidal pressure is modelled assuming that the ground is a porous medium (Figure 2.1). This means that the ground consists of solid particles with a continuous system of interconnected pores, which are either partially or fully filled with fluid. The assumptions that were taken into account by Biot for the development of the poroelastic theory are summarized below (van Dalen, 2013):

- The representative volume element is large compared to both the size of the solid grains and the size of the pores and small compared to the relevant wavelength. Hence, an average value of the solid and fluid displacement is considered.
- Only interconnected pores are taken into account when calculating the material porosity. Sealed pores are considered part of the solid matrix (Biot, 1956).
- The deformation of the elementary volume is linear elastic and reversible, though later in the present study nonlinear material behaviour will be investigated.
- Both material phases are compressible. However, only the solid phase can resist shearing.
- Both material phases are homogeneous and isotropic. No dissipation mechanism which takes place in the solid phase is taken into account.
- Thermoelastic and chemical reaction effects are not taken into account.

The fluid is at most cases water. It may also contain tiny air bubbles, which make the medium much more compressible than a homogeneous liquid (saturated soil). The influence of the entrapped air will be quantified in Chapter 3.

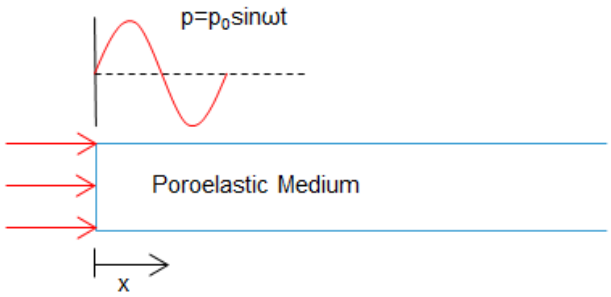

Figure 2.1. 1D soil bar subjected in sinusoidal excitation at the boundary

Therefore, the average density of the medium is equal to:

$$\rho = (1-n)\rho_s + n\rho_f \qquad 2.1$$

where (n) is the porosity of the medium, (ρ_s) is the density of the solid particles and (ρ_f) is the density of the fluid. In the present research, a sandy material is assumed.

Further assumptions on the partially saturated medium include that the entrapped air in the pores is not much enough to change the fluid density, leading to a constant value of permeability throughout the analysis as well.

2.1.1 Basic principles

The basic principles to describe the response of a porous medium is the conservation of mass and the conservation of momentum (Verruijt, 2010).

- Conservation of mass

Considering the elementary volume element of porous material already described and the fluid flow into and out of it (Figure 2.2), the increment of the fluid mass per unit time is determined by the net inward flux across the surfaces of the element. Hence, the basic equation of the conservation of mass of the pore fluid is (Verruijt, 2010):

$$\frac{\partial(n\rho_f)}{\partial t} + \nabla\cdot(n\rho_f \dot{\boldsymbol{U}}) = 0 \qquad 2.2$$

where $\dot{\mathbf{U}}$ is the average velocity of the fluid particles defining the velocity of the fluid.

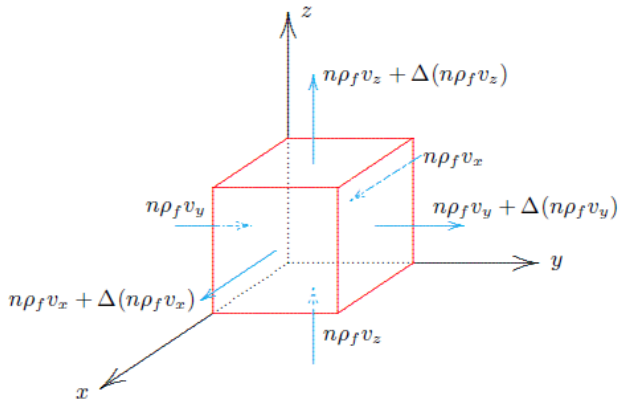

Figure 2.2. Conservation of mass of the fluid (Verruijt, 2010)

Taking into account that the density is a function of the fluid pressure, in accordance with the definition of compressibility:

$$\frac{\partial \rho_f}{\partial p} = \rho_f C_f \tag{2.3}$$

equation (2.2) gives after substitution and by assuming that the spatial derivative of the fluid density is zero:

$$\frac{\partial n}{\partial t} + nC_f \frac{\partial p}{\partial t} + \nabla \cdot (n\dot{\boldsymbol{U}}) = 0 \tag{2.4}$$

where (C_f) is the compressibility of the fluid. In the above equation, a term expressing the product of the fluid velocity and the pressure gradient has been disregarded assuming that both of them are small quantities.

Regarding the solid particles, the balance equation is (Verruijt, 2010):

$$\frac{\partial[(1-n)\rho_s]}{\partial t} + \nabla \cdot [(1-n)\rho_s \dot{\boldsymbol{u}}] = 0 \tag{2.5}$$

The particle density (ρ_s) is governed by the isotropic total stress (σ) and the pore pressure (p) as follows:

$$\frac{\partial \rho_s}{\partial t} = \frac{\rho_s C_s}{1-n}\left(\frac{\partial \sigma}{\partial t} - n\frac{\partial p}{\partial t}\right) = 0 \tag{2.6}$$

If (C_s) is the compressibility of the particle material, equation (2.5) yields:

$$-\frac{\partial n}{\partial t} + C_s\left(\frac{\partial \sigma}{\partial t} - n\frac{\partial p}{\partial t}\right) + \nabla \cdot [(1-n)\dot{\boldsymbol{u}}] = 0 \tag{2.7}$$

Combination of equations (2.4) and (2.7) gives:

$$n\left(C_f - C_s\right)\frac{\partial p}{\partial t} + C_s\frac{\partial \sigma}{\partial t} + \nabla \cdot \dot{\boldsymbol{u}} + \nabla \cdot \left[n\left(\dot{\boldsymbol{U}} - \dot{\boldsymbol{u}}\right)\right] = 0 \tag{2.8}$$

The last term of Equation (2.8) is associated with the specific discharge of Darcy's law for the flow of the fluid through a porous medium.

- Conservation of momentum

The equations of conservation of momentum, or equations of motion, should be expressed in three directions. Assuming that the total stresses are decomposed to effective stresses and pore pressures according to Terzaghi (1925):

$$\sigma_{ij} = \sigma'_{ij} + \alpha p \delta_{ij} \tag{2.9}$$

where $\alpha=1-C_s/C_m$ is the Biot's coefficient and δ_{ij} is the Kronecker delta function ($\delta=1$ when $i=j$ and $\delta=0$ when $i\neq j$, the set of equations is (Verruijt, 2010):

$$\begin{aligned}
-\frac{\partial \sigma'_{xx}}{\partial x} - \frac{\partial \sigma'_{yx}}{\partial y} - \frac{\partial \sigma'_{zx}}{\partial z} - \alpha\frac{\partial p}{\partial x} &= n\rho_f\frac{\partial \dot{U}_x}{\partial t} + (1-n)\rho_s\frac{\partial \dot{u}_x}{\partial t} \\
-\frac{\partial \sigma'_{xy}}{\partial x} - \frac{\partial \sigma'_{yy}}{\partial y} - \frac{\partial \sigma'_{zy}}{\partial z} - \alpha\frac{\partial p}{\partial y} &= n\rho_f\frac{\partial \dot{U}_y}{\partial t} + (1-n)\rho_s\frac{\partial \dot{u}_y}{\partial t} \\
-\frac{\partial \sigma'_{xz}}{\partial x} - \frac{\partial \sigma'_{yz}}{\partial y} - \frac{\partial \sigma'_{zz}}{\partial z} - \alpha\frac{\partial p}{\partial z} &= n\rho_f\frac{\partial \dot{U}_z}{\partial t} + (1-n)\rho_s\frac{\partial \dot{u}_z}{\partial t}
\end{aligned} \tag{2.10}$$

The left hand side of the equations 2.10 consists of the effective stress and the pore pressures, both resulting from the (total) force acting on a unit bulk area. These changes in stress result in respective accelerations of the fluid and the solid particles, shown in the right hand side of the equation.

The equations of conservation of momentum of the fluid are:

$$\begin{aligned}
-n\frac{\partial p}{\partial x}-\frac{n^2\eta}{\kappa}\left(\dot{U}_x-\dot{u}_x\right)&=n\rho_f\frac{\partial \dot{U}_x}{\partial t}+\tau n\rho_f\frac{\partial\left(\dot{U}_x-\dot{u}_x\right)}{\partial t}\\
-n\frac{\partial p}{\partial y}-\frac{n^2\eta}{\kappa}\left(\dot{U}_y-\dot{u}_y\right)&=n\rho_f\frac{\partial \dot{U}_y}{\partial t}+\tau n\rho_f\frac{\partial\left(\dot{U}_y-\dot{u}_y\right)}{\partial t}\\
-n\frac{\partial p}{\partial z}-\frac{n^2\eta}{\kappa}\left(\dot{U}_z-\dot{u}_z\right)&=n\rho_f\frac{\partial \dot{U}_z}{\partial t}+\tau n\rho_f\frac{\partial\left(\dot{U}_z-\dot{u}_z\right)}{\partial t}
\end{aligned} \qquad 2.11$$

where the interaction of the fluid and solid components due to friction is taken into account. In addition (τ) is a tortuosity factor, describing the added mass due to the tortuosity of the flow path, (η) is the viscosity of the pore fluid and (κ) is the permeability of the porous medium in [m^2]. The conservation of momentum of the solids can be obtained by subtraction of equation (2.11) from equation (2.10):

$$\begin{aligned}
-\frac{\partial\sigma'_{xx}}{\partial x}-\frac{\partial\sigma'_{yx}}{\partial y}-\frac{\partial\sigma'_{zx}}{\partial z}-(\alpha-n)\frac{\partial p}{\partial x}+\frac{n^2\eta}{\kappa}\left(\dot{U}_x-\dot{u}_x\right)&=(1-n)\rho_s\frac{\partial \dot{u}_x}{\partial t}-\tau n\rho_f\frac{\partial\left(\dot{U}_x-\dot{u}_x\right)}{\partial t}\\
-\frac{\partial\sigma'_{xy}}{\partial x}-\frac{\partial\sigma'_{yy}}{\partial y}-\frac{\partial\sigma'_{zy}}{\partial z}-(\alpha-n)\frac{\partial p}{\partial y}+\frac{n^2\eta}{\kappa}\left(\dot{U}_y-\dot{u}_y\right)&=(1-n)\rho_s\frac{\partial \dot{u}_y}{\partial t}-\tau n\rho_f\frac{\partial\left(\dot{U}_y-\dot{u}_y\right)}{\partial t}\\
-\frac{\partial\sigma'_{xz}}{\partial x}-\frac{\partial\sigma'_{yz}}{\partial y}-\frac{\partial\sigma'_{zz}}{\partial z}-(\alpha-n)\frac{\partial p}{\partial z}+\frac{n^2\eta}{\kappa}\left(\dot{U}_z-\dot{u}_z\right)&=(1-n)\rho_s\frac{\partial \dot{u}_z}{\partial t}-\tau n\rho_f\frac{\partial\left(\dot{U}_z-\dot{u}_z\right)}{\partial t}
\end{aligned} \qquad 2.12$$

- Constitutive equations

The deformations of the soil are fully determined by the effective stresses. For isotropic material, the relation between the strains and the effective stresses is described by the generalised Hooke's law:

$$\begin{aligned}
\sigma'_{xx}&=-\left(K-\frac{2}{3}G\right)\varepsilon-2G\varepsilon_{xx}, \quad \sigma'_{xy}=-2G\varepsilon_{xy}, \quad \sigma'_{xz}=-2G\varepsilon_{xz}\\
\sigma'_{yy}&=-\left(K-\frac{2}{3}G\right)\varepsilon-2G\varepsilon_{yy}, \quad \sigma'_{yz}=-2G\varepsilon_{yz}, \quad \sigma'_{yx}=-2G\varepsilon_{yx}\\
\sigma'_{zz}&=-\left(K-\frac{2}{3}G\right)\varepsilon-2G\varepsilon_{zz}, \quad \sigma'_{zx}=-2G\varepsilon_{zx}, \quad \sigma'_{zy}=-2G\varepsilon_{zy}
\end{aligned} \qquad 2.13$$

where (K) and (G) are the bulk and shear modulus of the material, respectively. One can enhance the above stress-strain relations with terms that can represent the stress history or time-dependent processes, such as creep. Later in this report, the above constitutive equation will assume strain-dependent stiffness to represent nonlinear material behaviour. In any case, the constitutive equations have to be expressed in terms of the governing stress parameter, which is the effective stress.

The strain components are related to displacements by the following kinematic equations

$$\begin{aligned}
\varepsilon_{xx}&=\frac{\partial u_x}{\partial x}, \quad \varepsilon_{xy}=\frac{1}{2}\left(\frac{\partial u_x}{\partial y}+\frac{\partial u_y}{\partial x}\right), \quad \varepsilon_{xz}=\frac{1}{2}\left(\frac{\partial u_x}{\partial z}+\frac{\partial u_z}{\partial x}\right)\\
\varepsilon_{yy}&=\frac{\partial u_y}{\partial y}, \quad \varepsilon_{yz}=\frac{1}{2}\left(\frac{\partial u_y}{\partial z}+\frac{\partial u_z}{\partial y}\right), \quad \varepsilon_{yx}=\frac{1}{2}\left(\frac{\partial u_y}{\partial x}+\frac{\partial u_x}{\partial y}\right)\\
\varepsilon_{zz}&=\frac{\partial u_z}{\partial z}, \quad \varepsilon_{zx}=\frac{1}{2}\left(\frac{\partial u_z}{\partial x}+\frac{\partial u_x}{\partial z}\right), \quad \varepsilon_{zy}=\frac{1}{2}\left(\frac{\partial u_z}{\partial y}+\frac{\partial u_y}{\partial z}\right)
\end{aligned} \qquad 2.14$$

Hence, the volumetric strain is:

$$\varepsilon = \varepsilon_{xx} + \varepsilon_{yy} + \varepsilon_{zz} = \frac{\partial u_x}{\partial x} + \frac{\partial u_y}{\partial y} + \frac{\partial u_z}{\partial z} \quad 2.15$$

2.1.2 Analytical solution

From the general system of equations described in Chapter 2.1.1, the following equations can be obtained for the one-dimensional case (x direction) of the wave propagation in porous medium problem (Verruijt, 2010):

Total mass conservation – Storage equation:

$$a\frac{\partial \dot{u}}{\partial x} + S_p\frac{\partial p}{\partial t} = -\frac{\partial\left[n\left(\dot{U} - \dot{u}\right)\right]}{\partial x} \quad 2.16$$

Stress-strain relation of the soil skeleton:

$$m_v\frac{\partial \sigma'}{\partial t} = -\frac{\partial \dot{u}}{\partial x} \quad 2.17$$

Conservation of total momentum:

$$n\rho_f\frac{\partial \dot{U}}{\partial t} + (1-n)\rho_s\frac{\partial \dot{u}}{\partial t} = -\frac{\partial \sigma'}{\partial x} - \alpha\frac{\partial p}{\partial x} \quad 2.18$$

Conservation of momentum of fluid (generalised Darcy's law):

$$n\rho_f\frac{\partial \dot{U}}{\partial t} + \tau n\rho_f\frac{\partial(\dot{U} - \dot{u})}{\partial t} = -n\frac{\partial p}{\partial x} - \frac{n^2\eta}{\kappa}\left(\dot{U} - \dot{u}\right) \quad 2.19$$

where m_v = [1/(K+4G/3)] is the 1D compressibility of the porous medium and $S_p = nC_f+(\alpha-n)C_s$ is the storativity of the pore space. The storativity is defined as the volume of water released from storage per unit surface area per unit decline of hydraulic head.

Because the excitation is harmonic, it is assumed that the pore pressure, the effective stresses as well as the velocity of the fluid and the solid particles are also harmonic:

$$\begin{bmatrix} p \\ \sigma' \\ \dot{U} \\ \dot{u} \end{bmatrix} = \begin{bmatrix} P \\ S \\ V \\ W \end{bmatrix} e^{i(\ell x + \omega t)} \quad 2.20$$

Substitution of (2.20) in equations (2.16)-(2.19) gives:

$$n\ell V + (a-n)\ell W = -S_p\omega P \quad 2.21$$

$$m_v\omega S = -\ell W \quad 2.22$$

$$n\rho_f\omega V + (1-n)\rho_s\omega W = -\ell S - \alpha\ell P \quad 2.23$$

$$(1+\tau)n\rho_f\omega V - \tau n\rho_f\omega W = -n\ell P + \frac{in^2\eta}{\kappa}V - \frac{in^2\eta}{\kappa}W \quad 2.24$$

The above system of equations is solved analytically with the assistance of the computing environment MATLAB, according to Verruijt (2010). Elimination of unknowns leads to a reduction of the system of four equations to a system of two, the determinant of which, namely the following quadratic polynomial equation, should be equal to zero in order to have a non-zero solution:

$$A\gamma^4 + B\gamma^2 + C = 0 \quad 2.25$$

where the coefficients A,B,C are complex numbers dependent on the porosity, the density of solids and fluid, the viscosity of the fluid, the storativity and permeability of the material and the frequency of the excitation.

It should be noted that the choice of the tortuosity factor was made according to Matyka et al. (2008). For sandy sediments, a factor of m=2 is selected and inserted in equation (2.26):

$$\tau(n) = 1 + m(1 - n) \tag{2.26}$$

Regarding the dynamic viscosity of the water, after some depth the ground temperature remains constant at about 20°C, so the value of η = 1.002*10^{-3}Ns/m^2 is selected (Kestin et al., 1978), which corresponds to the dynamic viscosity of water at 20°C under pressure of 1atm (101.3kPa).

The roots of equation (2.25) are:

$\gamma_{1,2} = \pm(q_1 + ir_1)$ and $\gamma_{3,4} = \pm(q_2 + ir_2)$

and lead to four different possible values of the complex wave number. The latter is linked to the wavelength ℓ via the following relation:

$\ell_{1,2} = \pm(q_1 + ir_1)\omega/c$ and $\ell_{3,4} = \pm(q_2 + ir_2)\omega/c$

where c is the propagation speed of plane waves with compressibility m_v and density ρ given by the following relation:

$$c = \sqrt{\frac{1}{\rho m_v}} \tag{2.27}$$

For the semi-infinite medium (x>0), which implies in the specific case, only roots with positive imaginary part are valid, because only these lead to a finite limit at infinity. In this case, the general solutions for the pore pressure, the velocity of the solids, the effective stress and the velocity of the fluid respectively are (Verruijt, 2010):

$$p = A_p e^{-(\omega/c)(r_1 - iq_1)x} e^{i\omega t} + B_p e^{-(\omega/c)(r_2 - iq_2)x} e^{i\omega t} \tag{2.28}$$

$$\dot{u} = A_u e^{-(\omega/c)(r_1 - iq_1)x} e^{i\omega t} + B_u e^{-(\omega/c)(r_2 - iq_2)x} e^{i\omega t} \tag{2.29}$$

$$\sigma' = A_s e^{-(\omega/c)(r_1 - iq_1)x} e^{i\omega t} + B_s e^{-(\omega/c)(r_2 - iq_2)x} e^{i\omega t} \tag{2.30}$$

$$\dot{U} = A_U e^{-(\omega/c)(r_1 - iq_1)x} e^{i\omega t} + B_U e^{-(\omega/c)(r_2 - iq_2)x} e^{i\omega t} \tag{2.31}$$

The above-mentioned solutions reveal the propagation of two compression waves in the porous medium. These waves were described by Biot (1956). The first wave corresponds to the first part of the summation of the right hand side of the equations (2.28)-(2.31). This wave, which is also known as compressional wave of the first kind, causes the two phases of the material to vibrate practically in phase. It is similar to an elastic wave with a small amount of attenuation (Cheng, 2016). The second wave is described by the second root (γ_2) of the equation (2.25) and corresponds to the second part of the summation in equations (2.28)-(2.31). This compressional wave of the second kind describes out-of-phase movement between the solid and the fluid phase of the material and is strongly attenuated because of the viscous damping mechanism caused by the relative motion of the fluid and the solid phase (van Dalen, 2013). As it will be shown later in this chapter, the characteristics of these waves are frequency dependent.

The boundary conditions on the left boundary for a sinusoidal excitation are:

$$x = 0: p = p_0 \sin(\omega t) \tag{2.32}$$

$$x = 0: \sigma' = (1 - a)p_0 \sin(\omega t) \quad 2.33$$

With the assistance of these boundary conditions the parameters A and B are calculated. For x=0, equations (2.28) and (2.30) give:

$$A_p + B_p = p_0 \quad 2.34$$

$$A_s + B_s = (1 - a)p_0 \quad 2.35$$

Following the procedure described by Verruijt (2010) the complex constants A_p and B_p are calculated for the case of a plane wave applied on the boundary, which contains the term $e^{i\omega t}$ instead of sin(ωt) in equations (2.32) and (2.33). In this case, the coefficients A and B can be calculated as constants and the final solution only contains the imaginary part of the general one. Hence, the coefficients are calculated as follows (Verruijt, 2010):

$$A_p = p_0 \frac{\left[d_f b - \gamma_2^2 + (1 - \alpha)\left(1 - \alpha d_f\right)\right]\left(1 - \alpha d_f - \gamma_1^2\right)}{(\gamma_1^2 - \gamma_2^2)\left(\alpha - \alpha^2 d_f - b d_f\right)} \quad 2.36$$

$$B_p = -p_0 \frac{\left[d_f b - \gamma_1^2 + (1 - \alpha)\left(\mathrm{a} - \alpha d_f\right)\right]\left(1 - \alpha d_f - \gamma_2^2\right)}{(\gamma_1^2 - \gamma_2^2)\left(\alpha - \alpha^2 d_f - b d_f\right)} \quad 2.37$$

$$A_u = A_p \frac{\left(d_f b - \alpha\gamma_1^2\right) c m_v}{\left(1 - \alpha d_f - \gamma_1^2\right)\gamma_1} \quad 2.38$$

$$B_u = B_p \frac{\left(d_f b - \alpha\gamma_2^2\right) c m_v}{\left(1 - \alpha d_f - \gamma_2^2\right)\gamma_2} \quad 2.39$$

$$A_s = -A_u \frac{\gamma_1}{c m_v} \quad 2.40$$

$$B_s = -B_u \frac{\gamma_2}{c m_v} \quad 2.41$$

$$A_U = -A_u \left(\frac{\alpha - n}{n} + \frac{\left(1 - \alpha d_f - \gamma_1^2\right) b}{n\left(d_f b - \alpha\gamma_1^2\right)}\right) \quad 2.42$$

$$B_U = -B_u \left(\frac{\alpha - n}{n} + \frac{\left(1 - \alpha d_f - \gamma_2^2\right) b}{n\left(d_f b - \alpha\gamma_2^2\right)}\right) \quad 2.43$$

where a, b and d_f are dimensionless parameters. These values are plugged in the equations (2.28) to (2.31) where the imaginary part is thus only taken into account. It should be noted that equations (2.29) and (2.31) calculate velocities. Because one is more interested in displacement than in velocity, the following formulas calculate the displacements of the pore fluid and the solid particles, respectively:

$$U = Im\left\{\frac{A_U e^{-(\omega/c)(r_1 - iq_1)x} e^{i\omega t} + B_U e^{-(\omega/c)(r_2 - iq_2)x} e^{i\omega t}}{i\omega}\right\} \quad 2.44$$

$$u = Im\left\{\frac{A_u e^{-(\omega/c)(r_1 - iq_1)x} e^{i\omega t} + B_u e^{-(\omega/c)(r_2 - iq_2)x} e^{i\omega t}}{i\omega}\right\} \quad 2.45$$

2.2 Cylindrical axisymmetric wave propagation in a linear poroelastic medium

2.2.1 Derivation of governing equations

In this section, an infinitely-wide cylindrical domain of poroelastic material is considered. The longitudinal axis of the cylinder coincides with the z-axis. An infinitely long cavity of radius surrounds the z-axis. Time-dependent harmonic pressure is applied on the cavity boundary, producing axisymmetric wave propagation in the porous medium. The problem is presented in Figure 2.3.

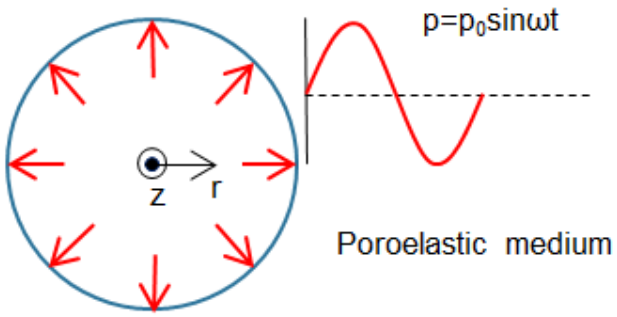

Figure 2.3. Representation of the cylindrical axisymmetric case

In the cylindrical coordinate system (r,θ,z) the equations that govern the wave propagation are solved following the formulation by Abbas and Abd-alla (2012), including a damping term based on the permeability and the porosity of the porous medium and the dynamic viscosity of the fluid phase (Biot, 1956). Only the radial direction (r) is considered, because the problem is independent from the vertical direction (z) axisymmetric. As a result:

$$\frac{\partial^2}{\partial t^2}(\rho_{11}u + \rho_{12}U) + b_0\frac{\partial}{\partial t}(u-U) = (A+2N)\frac{\partial \varepsilon}{\partial r} + Q\frac{\partial \epsilon}{\partial r} \quad 2.46$$

$$\frac{\partial^2}{\partial t^2}(\rho_{12}u + \rho_{22}U) - b_0\frac{\partial}{\partial t}(u-U) = Q\frac{\partial \varepsilon}{\partial r} + R\frac{\partial \epsilon}{\partial r} \quad 2.47$$

where

u and U are the displacements of the solid and the fluid phase respectively in the radial direction,

$\rho_{11}=(1-n)\rho_s-\rho_{12}$ is a mass coupling parameter for the solid phase,

$\rho_{22}=n\rho_f-\rho_{12}$ is a mass coupling parameter for the fluid phase,

$\rho_{12}=-(\tau-1)n\rho_f$ is the coupling term which exists due to the tortuosity of the porous network,

$b_0=\eta n^2/\kappa$ is the damping coefficient related to the permeability of the porous medium (Biot, 1956),

$A=1/m_v-2G/3+(1-n-C_s/m_v)^2/(C_f n')$,

$R=n^2/(C_f n')$ and

$Q=n(1-n-C_s/m_v)/(C_f n')$ are Biot coefficients calculated according to van Dalen (2013),

N is equal to the second Lame constant (μ) and

$n'=n+C_s/C_f*(1-n-C_s/m_v)$ is some effective porosity parameter (van Dalen, 2013)

Substituting the dilatation of the solid (ε) and the fluid (ϵ):

$$\varepsilon = \nabla \cdot \mathbf{u} = \frac{\partial u}{\partial r} + \frac{u}{r} \tag{2.48}$$

$$\epsilon = \nabla \cdot \mathbf{U} = \frac{\partial U}{\partial r} + \frac{U}{r} \tag{2.49}$$

to equations (2.46) and (2.47), they give:

$$\begin{aligned}\left(\rho_{11}\ddot{u} + \rho_{12}\ddot{U}\right) + b_0\left(\dot{u} - \dot{U}\right) &= (A+2N)\left(\frac{\partial^2 u}{\partial r^2} + \frac{1}{r}\frac{\partial u}{\partial r} - \frac{u}{r^2}\right) + Q\left(\frac{\partial^2 U}{\partial r^2} + \frac{1}{r}\frac{\partial U}{\partial r} - \frac{U}{r^2}\right) \\ &= (A+2N)\left(\nabla^2 u - \frac{u}{r^2}\right) + Q\left(\nabla^2 U - \frac{U}{r^2}\right)\end{aligned} \tag{2.50}$$

$$\begin{aligned}\left(\rho_{12}\ddot{u} + \rho_{22}\ddot{U}\right) - b_0\left(\dot{u} - \dot{U}\right) &= Q\left(\frac{\partial^2 u}{\partial r^2} + \frac{1}{r}\frac{\partial u}{\partial r} - \frac{u}{r^2}\right) + R\left(\frac{\partial^2 U}{\partial r^2} + \frac{1}{r}\frac{\partial U}{\partial r} - \frac{U}{r^2}\right) \\ &= Q\left(\nabla^2 u - \frac{u}{r^2}\right) + R\left(\nabla^2 U - \frac{U}{r^2}\right)\end{aligned} \tag{2.51}$$

At this point, potential functions are introduced for the solid and fluid displacement respectively:

$$u = \frac{\partial \varphi}{\partial r} \tag{2.52}$$

$$U = \frac{\partial \psi}{\partial r} \tag{2.53}$$

so, equations (2.50) and (2.51) give:

$$\left(\rho_{11}\ddot{\varphi} + \rho_{12}\ddot{\psi}\right) + b_0\left(\dot{\varphi} - \dot{\psi}\right) = (A+2N)\nabla^2\varphi + Q\nabla^2\psi \tag{2.54}$$

$$\left(\rho_{12}\ddot{\varphi} + \rho_{22}\ddot{\psi}\right) - b_0\left(\dot{\varphi} - \dot{\psi}\right) = Q\nabla^2\varphi + R\nabla^2\psi \tag{2.55}$$

The above equations are represented next in the frequency domain. The density terms are modified to frequency-dependent equivalent terms, incorporating the damping terms as well (van Dalen, 2013):

$\hat{b}(\omega)=b_0(1+i\omega\tau_c)^{1/2}$

$\tau_c=M/2\omega_c$

ω_c is the rollover frequency, at which the inertia terms and viscous effects are of the same order of magnitude (van Dalen, 2013)

M=1 (Smeulers, 1992)

$\hat{\rho}_{11}=\rho_{11}-i\hat{b}/\omega$

$\hat{\rho}_{22}=\rho_{22}-i\hat{b}/\omega$

$\hat{\rho}_{12}=\rho_{12}+i\hat{b}/\omega$

In this case, equations (2.54) and (2.55) in the frequency domain yield:

$$-\omega^2\hat{\rho}_{11}\hat{\varphi} - \omega^2\hat{\rho}_{12}\hat{\psi} = P\nabla^2\hat{\varphi} + Q\nabla^2\hat{\psi} \tag{2.56}$$

$$-\omega^2\hat{\rho}_{12}\hat{\varphi} - \omega^2\hat{\rho}_{22}\hat{\psi} = Q\nabla^2\hat{\varphi} + R\nabla^2\hat{\psi} \tag{2.57}$$

where P=A+2N. The general solutions of equations (2.56) and (2.57) for radially outward propagating waves are

$$\hat{\varphi} = A_{P1}H_0^{(2)}(\gamma_1 r) + A_{P2}H_0^{(2)}(\gamma_2 r) \tag{2.58}$$

$$\hat{\psi} = B_{P1}H_0^{(2)}(\gamma_1 r) + B_{P2}H_0^{(2)}(\gamma_2 r) \tag{2.59}$$

where

$H_0^{(2)}(\gamma_i r)$ are Hankel functions (or Bessel functions of third kind),

γ_i are the complex wavenumbers of each wave mode,

A_{Pi}, B_{Pi} are arbitrary amplitude coefficients determined later using the boundary conditions.

Substitution of the solutions (2.58) and (2.59) in one of the equations (2.56) or (2.57) for each of the two wave modes gives the amplitude ratios of the displacement of the fluid and the solid (β_i):

$$\beta_{P1} = \frac{B_{P1}}{A_{P1}} = -\frac{\omega^2\hat{\rho}_{11} - P\gamma_1^2}{\omega^2\hat{\rho}_{12} - Q\gamma_1^2} \tag{2.60}$$

$$\beta_{P2} = \frac{B_{P2}}{A_{P2}} = -\frac{\omega^2\hat{\rho}_{11} - P\gamma_2^2}{\omega^2\hat{\rho}_{12} - Q\gamma_2^2} \tag{2.61}$$

Hence, the amplitude coefficients A_{Pi} will be determined according to the boundary conditions and the B_{Pi} will be calculated according to the aforementioned amplitude ratios.

Boundary condition 1: At the cavity boundary, $r=r_0$, the displacement of both phases is equal.

$$\hat{u} = \hat{U} \tag{2.62}$$

Substitution of the solutions and further elaboration gives:

$$A_{P1} = \frac{(\beta_{P2} - 1)\left[H_{-1}^{(2)}(\gamma_2 r_0) - H_1^{(2)}(\gamma_2 r_0)\right]}{(1 - \beta_{P1})\left[H_{-1}^{(2)}(\gamma_1 r_0) - H_1^{(2)}(\gamma_1 r_0)\right]}A_{P2} \tag{2.63}$$

Boundary condition 2: At the cavity boundary, $r=r_0$, the total stress is equal to the opposite of the applied load (the minus sign is because compression is considered negative).

$$\sigma_{tot,rr} = 2G\varepsilon_{rr} + A\varepsilon + Q\epsilon + Q\varepsilon + R\epsilon = -p_0 \tag{2.64}$$

where $\varepsilon_{rr}=\partial u/\partial r$ is the radial strain of the solid particles and the rest of the strains have been calculated in equations (2.48) and (2.49). Substitutions of the displacement expressions instead of strains and elaboration of (2.64) leads to:

$$A_{P1} = \frac{p_0 r_0 - A_{P2}\gamma_2\left[H_0^{(2)}(\gamma_2 r_0)r_0\gamma_2(2G + A + Q(1 + \beta_{P2}) + R\beta_{P2}) + 2GH_1^{(2)}(\gamma_2 r_0)\right]}{\gamma_1\left[H_0^{(2)}(\gamma_1 r_0)r_0\gamma_1(2G + A + Q(1 + \beta_{P1}) + R\beta_{P1}) + 2GH_1^{(2)}(\gamma_1 r_0)\right]} \tag{2.65}$$

Equalisation of equations (2.63) and (2.65) gives the value of A_{P2}

$$A_{P2} = \\ = \frac{p_0 r_0(1 - \beta_{P1})H_1^{(2)}(\gamma_1 r_0)}{\gamma_2\{(\beta_{P2} - 1)H_1^{(2)}(\gamma_2 r_0)\left[H_0^{(2)}(\gamma_1 r_0)r_0\gamma_1(2G + A + Q(1 + \beta_{P1}) + R\beta_{P1}) + 2GH_1^{(2)}(\gamma_1 r_0)\right] + \\ +(1 - \beta_{P1})H_1^{(2)}(\gamma_1 r_0)\left[H_0^{(2)}(\gamma_2 r_0)r_0\gamma_2(2G + A + Q(1 + \beta_{P2}) + R\beta_{P2}) + 2GH_1^{(2)}(\gamma_2 r_0)\right]\}} \tag{2.66}$$

which can be substituted to either of the two equations, to determine A_{P1}:

$$A_{P1} = \\ = \frac{p_0 r_0 (\beta_{P2} - 1) H_1^{(2)}(\gamma_2 r_0)}{\gamma_1 \{(\beta_{P2} - 1) H_1^{(2)}(\gamma_2 r_0) \left[H_0^{(2)}(\gamma_1 r_0) r_0 \gamma_1 (2G + A + Q(1 + \beta_{P1}) + R\beta_{P1}) + 2G H_1^{(2)}(\gamma_1 r_0)\right] + \\ + (1 - \beta_{P1}) H_1^{(2)}(\gamma_1 r_0) \left[H_0^{(2)}(\gamma_2 r_0) r_0 \gamma_2 (2G + A + Q(1 + \beta_{P2}) + R\beta_{P2}) + 2G H_1^{(2)}(\gamma_2 r_0)\right]\}} \quad 2.67$$

Next, the coefficients B_{Pi} are calculated using the amplitude ratios of equations (2.60) and (2.61).

Combining equations (2.52)-(2.53) and (2.58)-(2.59) and taking into account that:-

$$\frac{d}{dr} H_0^{(2)}(\gamma_i r) = -H_1^{(2)}(\gamma_i r) \gamma_i \quad 2.68$$

the response is:

$$\hat{u} = -A_{P1} H_1^{(2)}(\gamma_1 r) \gamma_1 - A_{P2} H_1^{(2)}(\gamma_2 r) \gamma_2 \quad 2.69$$

$$\hat{U} = -B_{P1} H_1^{(2)}(\gamma_1 r) \gamma_1 - B_{P2} H_1^{(2)}(\gamma_2 r) \gamma_2 \quad 2.70$$

The steady-state response under sinusoidal loading on the cavity, $p=p_0 \cdot Im(e^{i\omega t})$, follows for the solid and fluid phase respectively:

$$u = Im(-A_{P1} H_1^{(2)}(\gamma_1 r) \gamma_1 e^{i\omega t} - A_{P2} H_1^{(2)}(\gamma_2 r) \gamma_2 e^{i\omega t}) \quad 2.71$$

$$U = Im(-B_{P1} H_1^{(2)}(\gamma_1 r) \gamma_1 e^{i\omega t} - B_{P2} H_1^{(2)}(\gamma_2 r) \gamma_2 e^{i\omega t}) \quad 2.72$$

2.3 Equations of motion in porous medium used by COMSOL Multiphysics (u-p formulation)

2.3.1 Derivation and comparison with Biot equations

In the previous section, a u-U formulation has been used, according to which, the variables of the problem are the displacement of the solid particles and the pore fluid. This kind of formulation, when implemented numerically, requires cumbersome calculations (Atalla et al., 1998). The main reason is that each displacement variable requires the definition of three degrees of freedom at each node in a FEM analysis. Apart from this, if only displacements are used in the interpolating functions, there is a high probability that numerical problems will be caused if the material is nearly incompressible, which is the case at this study as well (COMSOL Multiphysics Users' guide). As a result, it is more convenient to turn the system of equations into a "u-p formulation", which takes into account the displacement of the solid matrix and the pore fluid pressure. The latter is only one degree of freedom instead of three resulting in a total of four degrees of freedom per node instead of six. It also involves symmetric coupling terms, which reduce the computational time by five to twelve times (Atalla et al., 1998).

The inner workings of COMSOL Multiphysics are based on the above formulation. According to the user guide:

$$\rho \frac{\partial^2 \boldsymbol{u}}{\partial t^2} + \rho_f \frac{\partial^2 \boldsymbol{U^R}}{\partial t^2} - \nabla \cdot \boldsymbol{\sigma} = 0 \quad 2.73$$

$$\rho_f \frac{\partial^2 \boldsymbol{u}}{\partial t^2} + \frac{\tau \rho_f}{n} \frac{\partial^2 \boldsymbol{U^R}}{\partial t^2} + \frac{\eta}{\kappa} \frac{\partial \boldsymbol{U^R}}{\partial t} + \nabla p = 0 \quad 2.74$$

where

$\mathbf{U^R} = n(\mathbf{U}\text{-}\mathbf{u})$ is the displacement of the fluid relative to the solid phase, as it was defined by Biot (1962),

$\boldsymbol{\sigma}=\boldsymbol{\sigma}_{dr}-\alpha p\mathbf{I}$ is the total stress tensor ($\mathbf{I}$ is the identity matrix),

$\boldsymbol{\sigma}_{dr}=\mathbf{C}:\boldsymbol{\varepsilon}$, with $\boldsymbol{\varepsilon}$ being the strain tensor of the porous matrix and the elasticity tensor ($\mathbf{C}$) containing the elastic properties of the drained porous matrix**.**

Assuming that the displacement terms are harmonic functions of the angular frequency, the above equations in the frequency domain yield:

$$-\rho\omega^2\boldsymbol{u}-\rho_f\omega^2\boldsymbol{U^R}-\nabla\cdot\boldsymbol{\sigma}=0 \tag{2.75}$$

$$-\rho_f\omega^2\boldsymbol{u}-\rho_c\omega^2\boldsymbol{U^R}+\nabla p=0 \tag{2.76}$$

where

$$\rho_c(\omega)=\frac{\tau\rho_f}{n}+\frac{\eta}{i\omega\kappa} \tag{2.77}$$

is a complex density accounting for tortuosity, dynamic viscosity and permeability.

Because of reasons already mentioned, the u-p formulation is preferred. Solving equation 2.76 for fluid displacement ($\mathbf{U}$) and substitution in 2.75 gives:

$$-\rho\omega^2\boldsymbol{u}-\frac{\rho_f}{\rho_c(\omega)}\left(\nabla p-\rho_f\omega^2\boldsymbol{u}\right)-\nabla\cdot\boldsymbol{\sigma}=0 \tag{2.78}$$

Substitution of $\boldsymbol{\sigma}$ in 2.78 gives the first equation in terms of $\mathbf{u}$ and p. The second equation comes from the divergence of 2.76 divided by ($-\rho_c$):

$$\omega^2\nabla\cdot\left(\frac{\rho_f}{\rho_c(\omega)}\boldsymbol{u}\right)+\omega^2\nabla\cdot\boldsymbol{w}+\nabla\cdot\left(-\frac{1}{\rho_c(\omega)}\right)\nabla p=0 \tag{2.79}$$

Using the expressions for volumetric strain (ε) and fluid displacement (ϵ) to eliminate U (Biot, 1962):

$$\varepsilon=\nabla\cdot\boldsymbol{u} \tag{2.80}$$

$$\epsilon=-\nabla\cdot\boldsymbol{U^R}=-n\nabla\cdot(\boldsymbol{U}-\boldsymbol{u})=\frac{p}{\mathcal{M}}+\alpha\varepsilon \tag{2.81}$$

where $\mathcal{M}$ is Biot's coefficient given by:

$$\mathcal{M}=\frac{1}{nC_f+(\alpha-n)(1-\alpha)/K} \tag{2.82}$$

equation 2.79 gives:

$$\omega^2\nabla\cdot\left(\frac{\rho_f}{\rho_c(\omega)}\boldsymbol{u}\right)-\omega^2\left(\frac{1}{\mathcal{M}}p+\alpha\varepsilon\right)+\nabla\cdot\left(-\frac{1}{\rho_c(\omega)}\right)\nabla p=0 \tag{2.83}$$

so the so-called non-simplified set of equations in the frequency domain used by the 'Poroelastic Waves' interface of COMSOL Multiphysics is:

$$-\omega^2\left(\rho-\frac{\rho_f^2}{\rho_c(\omega)}\right)\boldsymbol{u}-\nabla\cdot(\sigma_{dr}(\boldsymbol{u})-\alpha p\boldsymbol{I})=\frac{\rho_f}{\rho_c(\omega)}\nabla p \tag{2.84}$$

$$-\frac{k_{eq}^2}{\rho_c(\omega)}p+\nabla\cdot\left(-\frac{1}{\rho_c(\omega)}\left(\nabla p-\omega^2\rho_f\boldsymbol{u}\right)\right)=\omega^2\alpha\nabla\cdot\boldsymbol{u} \tag{2.85}$$

where $k_{eq}=\omega\sqrt{(\rho_c/\mathcal{M})}$ is an equivalent wave number.

In order to maintain consistency with the notation so far used, according to which the coefficients are expressed in terms of Biot's parameters and frequency dependent densities (P,R,Q, $\hat{\rho}_{11}$, $\hat{\rho}_{12}$, $\hat{\rho}_{22}$) and not

the equivalent (α,$\mathcal{M}$,ρ_{av},ρ_c,ρ_f), the above equations (2.84 and 2.85) are compared term by term with equations 2.50 and 2.51, after expressing them in the non-simplified u-p formulation in the frequency domain (van Dalen, 2013):

$$\omega^2\hat{\rho}_{eq}\boldsymbol{u} + (\lambda + 2G)\nabla\nabla\cdot\boldsymbol{u} - G\nabla\times\nabla\times\boldsymbol{u} = \frac{nH_s}{R}\nabla p \qquad 2.86$$

$$\omega^2\hat{\rho}_{22}p + R\nabla^2 p = -\omega^2\hat{\rho}_{22}\frac{H_s}{n}\nabla\cdot\boldsymbol{u} \qquad 2.87$$

where the terms of external body forces are ignored and

$\hat{\rho}_{eq} = d_0/\hat{\rho}_{22}$

$d_0 = \hat{\rho}_{11}\hat{\rho}_{22}-\hat{\rho}_{12}^2$

$H_s = Q+R*(-\hat{\rho}_{12}/\hat{\rho}_{22})$

The respective terms of both sets of equations and the result of their comparison are summarized in Table 2.1. It has to be noted that some coefficient expressions are identical between the two formulations, whereas in cases where elaboration by hand was difficult, the ratio of the coefficients was calculated numerically.

Table 2.1. Comparison of the primary variables (u and p) coefficients and according results

COMSOL equation set	Van Dalen equation set	Equivalence - Numerical ratio	Equivalence - Numerical ratio ($\hat{b}=b_0$)
$\left(\boldsymbol{\rho} - \frac{\boldsymbol{\rho_f^2}}{\boldsymbol{\rho_c(\omega)}}\right)$	$\hat{\rho}_{eq}$	equivalent	equivalent
$\boldsymbol{\nabla\cdot\sigma_{dr}(u)}$	$(\lambda+2G)\nabla\nabla\cdot\hat{\boldsymbol{u}} - G\nabla\times\nabla\times\hat{\boldsymbol{u}}$	equivalent	equivalent
$\boldsymbol{\alpha} - \frac{\boldsymbol{\rho_f}}{\boldsymbol{\rho_c(\omega)}}$	$\frac{nH_s}{R}$	equivalent	equivalent
$\frac{\boldsymbol{k_{eq}^2}}{\boldsymbol{\rho_c(\omega)}}$	$\omega^2\hat{\rho}_{22}$	4.016E-16+8.403E-15i	2.835E-14 + 7.376E-14i
$\frac{\boldsymbol{1}}{\boldsymbol{\rho_c(\omega)}}$	R	3.216E-16+8.411E-15i	2.835E-14 + 7.376E-14i
$\frac{\boldsymbol{\rho_f}}{\boldsymbol{\rho_c(\omega)}} - \boldsymbol{\alpha}$	$-\hat{\rho}_{22}\frac{H_s}{n}$	4.017E-16+8.404E-15i	2.835E-14 + 7.376E-14i

It can be observed that the ratio of the respective coefficients, when elaboration was not fully accomplished, is in the order of magnitude of 10^{-15}. If one does not take into account the frequency dependency of the density and damping terms, in other words, when one assumes b_0 instead of $\hat{b}$ and hence ρ_{11}, ρ_{12} and ρ_{22} instead of $\hat{\rho}_{11}$, $\hat{\rho}_{22}$ and $\hat{\rho}_{12}$, which is also assumed in the current research, the ratio of the respective terms of the two formulations is constant and equal to 2.835E-14 + 7.376E-14i. In other words, the second equation used by COMSOL Multiphysics (2.85) is apparently equal to the equation (2.87) multiplied by the aforementioned complex number.

What is more, a difference in the numerically calculated wave velocities is noticed. In contrast to the wave velocities calculated in Section 3.1.3, COMSOL Multiphysics calculates the following so-called 'wave speeds':

$$c_{P,i} = Re(\omega/\gamma_i) \quad 2.88$$

which is not the wave velocity calculated so far. Although the value of $c_{P,i}$ for the fast wave is comparable to the previously calculated phase velocity ($c_{P.i,} = \omega/Re(\gamma_i)$), because the imaginary part of the wavenumber of the fast wave is negligible, this is not the case for the slow wave, the wavenumber of which consists of almost equal real and imaginary parts. The difference in wave speed calculated by COMSOL Multiphysics and the phase velocity can be significantly large as it can be observed by the examples presented in Table 2.2.

Table 2.2. Comparison of the 'wave speed' according to COMSOL Multiphysics with the phase velocity (slow wave)

Frequency [Hz]	$c_{P2} = Re(\omega/\gamma_i)$ [m/s]	$c_{P2} = \omega/ Re(\gamma_i)$ [m/s]
0.2	0.656	1.312
2	2.079	4.138
20	6.694	12.775
200	23.514	32.823
2000	41.964	42.713

2.3.2 Comparison with the formulation by Zienkiewicz et al.

Zienkiewicz et al. (1999) conducted extensive research regarding the governing equations of poroelastodynamics. Starting from Biot's equations, Zienkiewicz et al. expressed the wave propagation in porous medium using three equations with three independent variables ('u-p-U formulation'). For low frequencies, the convective terms (nonlinear) and the fluid acceleration relative to the soil (linear term) are assumed to be negligible. As a result, they can be omitted from the equation set (Zienkiewicz et al., 1999). In that case, a simplified u-p formulation can be derived, which is convenient for numerical approximations, due to the reasons mentioned in Section 2.3. This set of equations is exact for consolidation and can approximate very well the wave propagation in low frequencies. Except for that, if one neglects only the convective terms, the equations of motion can be expressed in u-U formulation. In this section, a comparison is made between the equations derived by Zienkiewicz et al. (1999) and the sets of equations derived in this work. First, the u-U formulation is compared to equations (2.46) and (2.47). Second, the u-p formulation is compared to the equations (2.84) and (2.85) which are used by COMSOL Multiphysics.

The full u-p-U formulation consists of the following three equations.

The first equation expresses the overall momentum balance equation for the solid-fluid mixture is:

$$\boldsymbol{S}^{\boldsymbol{T}}\boldsymbol{\sigma} - \rho\ddot{\boldsymbol{u}} - \rho_f[\dot{\boldsymbol{w}} + \boldsymbol{w}\nabla^T\boldsymbol{w}] + \rho\boldsymbol{b} = 0 \quad 2.89$$

where S is the spatial derivative matrix for two dimensions (according zero terms are neglected), **σ** is the total stress tensor, **u** is the solid matrix displacement, **w** is the fluid velocity relative to the solid and **b** is a term describing body forces which will be neglected in accordance to the assumptions so far.

It should be remarked that the terms containing the fluid velocity consist of a relative fluid-solid acceleration term and a convective term. Zienkiewicz et al. (1999) suggest to neglect both these terms. However, at this stage, only the convective term will be omitted, in order to conduct a direct comparison with the equations which COMSOL Multiphysics makes use of.

The second equation is the conservation of momentum for the fluid:

$$-\nabla p_f - \boldsymbol{\mathcal{R}} - \rho_f \ddot{\boldsymbol{u}} - \rho_f \dot{\boldsymbol{w}}/n + \rho_f \boldsymbol{b} = 0 \tag{2.90}$$

where $\boldsymbol{\mathcal{R}}$ represents the viscous drag forces and can be written as

$$\boldsymbol{k}\boldsymbol{\mathcal{R}} = \boldsymbol{w} \tag{2.91}$$

assuming Darcy seepage law. It is essential to note, that the permeability $\boldsymbol{k}$ defined used in equation 2.91 is different to the one used so far (κ), because it does not include the dynamic viscosity of the fluid. Hence, the relation between the two permeability variables is:

$$\boldsymbol{k} = \frac{\boldsymbol{\kappa}}{\eta} \tag{2.92}$$

and the unit is m^3s/kg instead of m^2.

The third equation is the mass balance equation of the flow, or, in other words, the flow conservation equation:

$$\nabla^T \boldsymbol{w} + \alpha \boldsymbol{m}\dot{\varepsilon} + S_p \dot{p} + n\frac{\dot{\rho}_f}{\rho_f} + \dot{s}_0 = 0 \tag{2.93}$$

where **m** is a vector written in the form

$$\boldsymbol{m} = [1\ 1\ 1\ 0\ 0\ 0]^T \tag{2.94}$$

and s_0 is a source term. The last two terms of equation 2.93 can be neglected, because it is assumed that the fluid density remains constant and there is no source term. In that case, equation 2.93 reduces to:

$$\nabla^T \boldsymbol{w} + \alpha \boldsymbol{m}\dot{\varepsilon} + S_p \dot{p} = 0 \tag{2.95}$$

which is equivalent with equation 2.16 for the one dimensional case, based on Verruijt (2010).

The set of equations (2.89), (2.90) and (2.95) is reduced as follows, after neglecting only the convective and external force terms:

$$\boldsymbol{S}^T \boldsymbol{\sigma} - \rho \ddot{\boldsymbol{u}} - \rho_f \dot{\boldsymbol{w}} = 0 \tag{2.96}$$

$$-\nabla p - \boldsymbol{k}^{-1}\boldsymbol{w} - \rho_f \ddot{\boldsymbol{u}} - \rho_f n^{-1} \dot{\boldsymbol{w}} = 0 \tag{2.97}$$

$$\nabla^T \cdot \boldsymbol{w} + \alpha \boldsymbol{m}\dot{\varepsilon} + S_p \dot{p} = 0 \tag{2.98}$$

Elimination of the pore pressures (p) leads to a set of equations containing only displacement variables; the so-called u-U formulation. The first step is to substitute the relative velocity (**w**) and the volumetric strain (ε) with displacement terms, according to:

$$\dot{\boldsymbol{U}}^{\boldsymbol{R}} = \dot{\boldsymbol{U}} - \dot{\boldsymbol{u}} = \boldsymbol{w}/n \tag{2.99}$$

and equation (2.80), respectively. Integration of equation (2.98) in time gives the following expression of pore pressures:

$$p = -\frac{1}{S_p}[(\alpha - n)\nabla \cdot \boldsymbol{u} + n\nabla \cdot \boldsymbol{U}] \tag{2.100}$$

To remain consistent with the different formulations so far, the term of total stress in equation (2.96) needs to be substituted by effective stress and pore pressure terms, according to the original effective stress definition (2.9). The expression for the pore pressures (2.100) is inserted in both equation (2.96) and (2.97) giving the final set of u-U formulation:

$$\boldsymbol{S}^T \boldsymbol{\sigma}' + \frac{\alpha(\alpha - n)}{S_p}\nabla\nabla \cdot \boldsymbol{u} + \frac{\alpha n}{S_p}\nabla\nabla \cdot \boldsymbol{U} - (1 - n)\rho_s \ddot{\boldsymbol{u}} - n\rho_f \ddot{\boldsymbol{U}} = 0 \tag{2.101}$$

$$\frac{\alpha - n}{S_p}\nabla\nabla \cdot \boldsymbol{u} + \frac{n}{S_p}\nabla\nabla \cdot \boldsymbol{U} - \frac{\eta n}{\boldsymbol{\kappa}}(\dot{\boldsymbol{U}} - \dot{\boldsymbol{u}}) - \rho_f \ddot{\boldsymbol{U}} = 0 \quad 2.102$$

This set of equations is identical to the original Biot equations (2.46) and (2.47).

Because of the reasons mentioned previously in this chapter, the three governing equations (2.89), (2.90) and (2.95) are reduced to the simplified u-p formulation. Not only the convective terms are eliminated, but also the relative acceleration between the two phases of the material. The system of the three equations (2.96) to (2.98) can be written as follows (Zienkiewicz et al., 1999):

$$\boldsymbol{S}^{\boldsymbol{T}}\boldsymbol{\sigma} - \rho\ddot{\boldsymbol{u}} = 0 \quad 2.103$$

$$-\nabla p - n\boldsymbol{k}^{-1}\boldsymbol{U}^{\boldsymbol{R}} - \rho_f \ddot{\boldsymbol{u}} = 0 \quad 2.104$$

$$n\nabla^T \cdot \dot{\boldsymbol{U}}^{\boldsymbol{R}} + \alpha \boldsymbol{m}\dot{\varepsilon} + S_p\dot{p} = 0 \quad 2.105$$

where the relative displacement is defined by equation (2.99). Solving equation 2.104 for $\mathbf{U^R}$ and substituting it to the other two equations, the following system of two equations is obtained:

$$\boldsymbol{S}^{\boldsymbol{T}}\boldsymbol{\sigma} - \rho\ddot{\boldsymbol{u}} = 0 \quad 2.106$$

$$\nabla^T \boldsymbol{k}\left(-\nabla p - \rho_f \ddot{\boldsymbol{u}}\right) + \alpha\nabla \cdot \boldsymbol{u} + S_p p = 0 \quad 2.107$$

The two equations above consist the 'simplified u-p formulation' of the original Biot equations. However, the frequency-domain formulation within the 'Poroelastic Waves' interface of COMSOL Multiphysics does not omit the inertia terms. Equations (2.84) and (2.85) form the 'non-simplifed u-p formulation'. Following by the same exact procedure to derive the 'simplified u-p formulation', with the only difference that the starting point is the set of equations (2.96) to (2.98), the resulting set of equations is:

$$\boldsymbol{S}^{\boldsymbol{T}}\sigma - \left(\rho + \frac{n\omega\rho_f^2}{\rho_f\omega - \frac{in}{\boldsymbol{k}}}\right)\omega^2\boldsymbol{u} + \frac{n\omega\rho_f}{\rho_f\omega - \frac{in}{\boldsymbol{k}}}\nabla p = 0 \quad 2.108$$

$$\nabla^T\left(\frac{n\nabla p}{\rho_f\omega^2 - \frac{i\omega n}{\boldsymbol{k}}} - \frac{n\rho_f\omega}{\rho_f\omega - \frac{in}{\boldsymbol{k}}}\boldsymbol{u}\right) + \alpha\nabla \cdot \boldsymbol{u} + S_p p = 0 \quad 2.109$$

The above set of equations has been derived following the procedure described in Zienkiewicz et al. (1999) by neglecting only the convective terms. It is fully equivalent with equations (2.84) and (2.85), expressed in the frequency domain. More specifically: Given the definition for ρ_c by equation 2.77 with the only difference that tortuosity is not taken into account by Zienkiewicz et al. (1999), hence τ=1, it can be concluded that equation 2.108 is identical to equation 2.84 whilst equation 2.109 to 2.85 scaled by $1/\omega^2$. Consequently, COMSOL Multiphysics makes use of the u-p formulation described by Zienkiewicz et al. (1999) but including the relative displacement terms and tortuosity as far as the frequency domain is concerned. Only the convective terms are omitted.

The validity of the assumption by Zienkiewicz et al. (1999) that the relative acceleration terms can be neglected for low frequencies is presented in Section 5.1, along with the comparison of the analytical with the numerical results. However, the simplified equations in COMSOL formulation will be presented here. To start with, when the relative acceleration between the fluid and the solid phase is not taken into account, the complex density of eq. (2.77) simplifies to

$$\rho_c(\omega) = \frac{i\omega\eta}{\kappa} \quad 2.110$$

This term is very large compared to the fluid density, so that the terms containing the ratio $\rho_f/\rho_c(\omega)$ are negligible. Hence, the 'simplified u-p formulation' of the equations of motion can be implemented by COMSOL Multiphysics in the frequency domain if equations (2.84) and (2.85) reduce to:

$$-\rho\omega^2\boldsymbol{u} - \nabla\cdot(\sigma_{dr}(\boldsymbol{u}) - \alpha p I) = 0 \tag{2.111}$$

$$-\frac{k_{eq}^2}{\rho_c(\omega)}p + \nabla\cdot\left(-\frac{\nabla p}{\rho_c(\omega)}\right) = \omega^2\alpha\nabla\cdot\boldsymbol{u} \tag{2.112}$$

This set of equations is identical to the 'simplified u-p formulation' by Zienkiewicz et al. (1999), namely equations (2.106) and (2.107). The effect of the omission of relative acceleration will be investigated numerically in Section 5.1.

2.3.3 Equations in time domain

When non-linearity is introduced, the dynamic response requires revision of the mechanical properties at each time step. More specifically, the shear modulus (G) will be defined as a function of shear stress or strain. As a result, frequency domain analysis is not applicable, and therefore, the governing equations should be transformed into time domain. To accomplish this, equations 2.86 and 2.87 are elaborated, in order to isolate the frequency terms and replace (iω) and ($-\omega^2$) terms by (d/dt) and (d^2/dt^2) respectively. This procedure results in the following time-domain equations:

$$\begin{aligned}(\rho_{11}\rho_{22}-\rho_{12}^2)\frac{\partial^4\boldsymbol{u}(t)}{\partial t^4} + \rho b_0\frac{\partial^3\boldsymbol{u}(t)}{\partial t^3} + \rho_{22}\frac{\partial^2\sigma'(t)}{\partial t^2} + b_0\frac{\partial\sigma'(t)}{\partial t}\\ = -n\frac{\partial^2}{\partial t^2}\left[\left(\frac{\alpha-n}{n}\rho_{22}-\rho_{12}\right)\nabla p(t)\right] - b_0 n\frac{\partial}{\partial t}\left[\frac{\alpha}{n}\nabla p(t)\right]\end{aligned} \tag{2.113}$$

$$-\rho_{22}\frac{\partial^2 p(t)}{\partial t^2} - b_0\frac{\partial p(t)}{\partial t} + R\nabla^2 p(t) = \left(\frac{Q\rho_{22}-R\rho_{12}}{n}\right)\frac{\partial^2\nabla\cdot\boldsymbol{u}(t)}{\partial t^2} + b_0\left(\frac{Q+\mathrm{R}}{n}\right)\frac{\partial\nabla\cdot\boldsymbol{u}(t)}{\partial t} \tag{2.114}$$

The first equation contains time derivatives of the third and fourth order which are not convenient for standard numerical solvers. Alternatively, the u-U formulation in time domain is used. The time domain equations in u-U formulation are the following (Zienkiewicz et al., 1999):

$$\boldsymbol{S}^{\boldsymbol{T}}\boldsymbol{\sigma}' + \frac{\alpha(\alpha-n)}{S_p}\nabla\nabla\cdot\boldsymbol{u} + \frac{\alpha n}{S_p}\nabla\nabla\cdot\boldsymbol{U} - (1-n)\rho_s\ddot{\boldsymbol{u}} - n\rho_f\ddot{\boldsymbol{U}} = 0 \tag{2.115}$$

$$\frac{\alpha-n}{S_p}\nabla\nabla\cdot\boldsymbol{u} + \frac{n}{S_p}\nabla\nabla\cdot\boldsymbol{U} - \frac{\eta n}{\boldsymbol{\kappa}}\left(\dot{\boldsymbol{U}}-\dot{\boldsymbol{u}}\right) - \tau\rho_f\ddot{\boldsymbol{U}} + (1-\tau)\rho_f\ddot{\boldsymbol{u}} = 0 \tag{2.116}$$

where τ is the tortuosity. If τ=1 the system of equations drops to the set of equations (2.101) and (2.102).

Although the above set of equations is appropriate for a time-domain analysis, the software package COMSOL Multiphysics makes use of the u-p formulation. The set of equations that COMSOL Multiphysics uses by default in the 'Poroelasticity' interface is the following:

$$-\nabla\cdot\boldsymbol{\sigma} = \boldsymbol{F_v} \tag{2.117}$$

$$\rho_f S_p\dot{p} + \nabla\cdot\left(\rho_f\boldsymbol{u_D}\right) = Q_m - \rho_f\alpha\dot{\varepsilon} \tag{2.118}$$

where Q_m is a mass source term (nil) and $\mathbf{u_D}$ is the Darcy's velocity field, equal to:

$$\boldsymbol{u_D} = -\frac{\boldsymbol{\kappa}}{\eta}(\nabla p) \tag{2.119}$$

Equations (2.117) and (2.118) can represent exactly the quasi-static consolidation model. However, for dynamic problems they are not appropriate, because they do not take into consideration

acceleration/inertia terms. The contribution of the solid acceleration was found by Chan (1988) to be significant. Therefore, the inclusion of acceleration terms is mandatory, although it will render the final equation to be non-symmetric (Zienkiewicz et al. 1999). This leads to a u-p formulation which can simulate the wave propagation in porous media for the low-frequency range more effectively, according to the assumptions introduced by Zienkiewicz et al. (1999):

$$-\nabla \cdot \boldsymbol{\sigma} = -\rho \ddot{\boldsymbol{u}} + \rho \boldsymbol{g} \tag{2.120}$$

$$\rho_f S_p \dot{p} + \nabla \cdot \left(\rho_f \boldsymbol{u_D}\right) = Q_m - \rho_f \alpha \dot{\varepsilon} \tag{2.121}$$

In equation (2.120) the acceleration terms are introduced as external (body) forces and equation (2.121) is identical, though the Darcy's velocity field is now enhanced with inertia terms and is defined as:

$$\boldsymbol{u_D} = -\frac{\boldsymbol{\kappa}}{\eta}\left(\nabla p + \rho_f \ddot{\boldsymbol{u}} + \rho_f \boldsymbol{g}\right) \tag{2.122}$$

Equations (2.120) and (2.121) are the set of equations of motion for the numerical solution of the cylindrical wave propagation in porous medium in the time domain and are in accordance with the u-p formulation introduced by Zienkiewicz et al. (1999), and more specifically with equations (2.106) and (2.107) enhanced with the gravitational load. It has to be noted that equation (2.121) is the same as equation (2.107), but multiplied by the fluid density (ρ_f).

2.4 Summary

In this chapter the mathematical formulations used for both the analytical solution and for the numerical solution of the pressuremeter test is developed. Combining the cylindrical cavity expansion mechanism with the poroelastic theory by Biot (1956) the set of governing equations for every analysis stage has been presented and various versions found in the literature are compared to each other and with the governing equations used by the finite element platform COMSOL Multiphysics. The governing equations are summarised in Table 2.3:

Table 2.3. Summary of the governing equations used for the analytical solutions and the numerical approximation

1. 1D infinitely long soil bar (Verruijt, 2010) – Equations (2.5) to (2.8)

$$\frac{\partial[(1-n)\rho_s]}{\partial t} + \nabla \cdot [(1-n)\rho_s \dot{\boldsymbol{u}}] = 0$$

$$\frac{\partial \rho_s}{\partial t} = \frac{\rho_s C_s}{1-n}\left(\frac{\partial \boldsymbol{\sigma}}{\partial t} - n\frac{\partial p}{\partial t}\right) = 0$$

$$-\frac{\partial n}{\partial t} + C_s\left(\frac{\partial \boldsymbol{\sigma}}{\partial t} - n\frac{\partial p}{\partial t}\right) + \nabla \cdot [(1-n)\dot{\boldsymbol{u}}] = 0$$

$$n\left(C_f - C_s\right)\frac{\partial p}{\partial t} + C_s\frac{\partial \boldsymbol{\sigma}}{\partial t} + \nabla \cdot \dot{\boldsymbol{u}} + \nabla \cdot \left[n\left(\dot{\boldsymbol{U}} - \dot{\boldsymbol{u}}\right)\right] = 0$$

2. Cylindrical axisymmetric poroelasticity u-U formulation (Biot, 1956) – Equations (2.46) and (2.47)

$$\left(\rho_{11}\ddot{\boldsymbol{u}} + \rho_{12}\ddot{\boldsymbol{U}}\right) + b_0\left(\dot{\boldsymbol{u}} - \dot{\boldsymbol{U}}\right) = (A+2N)\nabla\nabla \cdot \boldsymbol{u} + Q\nabla\nabla \cdot \boldsymbol{U}$$

$$\left(\rho_{12}\ddot{\boldsymbol{u}} + \rho_{22}\ddot{\boldsymbol{U}}\right) - b_0\left(\dot{\boldsymbol{u}} - \dot{\boldsymbol{U}}\right) = Q\nabla\nabla \cdot \boldsymbol{u} + R\nabla\nabla \cdot \boldsymbol{U}$$

3. Poroelasticity simplified and non-simplified u-p formulation (COMSOL Multiphysics 'Poroelastic Waves' interface in frequency domain) – Equations (2.84) and (2.85)

$$-\omega^2\left(\rho - \frac{\rho_f^2}{\rho_c(\omega)}\right)\boldsymbol{u} - \nabla \cdot (\sigma_{dr}(\boldsymbol{u}) - \alpha p I) = \frac{\rho_f}{\rho_c(\omega)}\nabla p$$

$$-\frac{k_{eq}^2}{\rho_c(\omega)}p + \nabla\cdot\left(-\frac{1}{\rho_c(\omega)}\left(\nabla p - \omega^2\rho_f\boldsymbol{u}\right)\right) = \omega^2\alpha\nabla\cdot\boldsymbol{u}$$

4. Poroelasticity non-simplified u-p formulation (van Dalen, 2013) – Equations (2.86) and (2.87)

$$\omega^2\hat{\rho}_{eq}\boldsymbol{u} + (\lambda + 2G)\nabla\nabla\cdot\boldsymbol{u} - G\nabla\times\nabla\times\boldsymbol{u} = \frac{nH_s}{R}\nabla p$$

$$\omega^2\hat{\rho}_{22}p + R\nabla^2 p = -\omega^2\hat{\rho}_{22}\frac{H_s}{n}\nabla\cdot\boldsymbol{u}$$

5. Poroelasticity simplified u-p formulation (Zienkiewicz et al., 1999) – Equations (2.106) and (2.107)

$$\boldsymbol{S}^{\boldsymbol{T}}\boldsymbol{\sigma} - \rho\ddot{\boldsymbol{u}} + \rho\boldsymbol{b} = 0$$

$$\nabla^T\mathbf{k}\left(-\nabla p - \rho_f\ddot{\boldsymbol{u}} - \rho_f\boldsymbol{b}\right) + \alpha\nabla\cdot\boldsymbol{u} + S_p p = 0$$

6. Poroelasticity simplified u-p formulation in the time domain (Zienkiewicz et al., 1999) and (COMSOL Multiphysics 'Poroelasticity' interface) – Equations (2.120) to (2.122)

$$-\nabla\cdot\boldsymbol{\sigma} = -\rho\ddot{\boldsymbol{u}} + \rho\boldsymbol{g}$$

$$\rho_f S_p\dot{p} + \nabla\cdot\left(\rho_f\boldsymbol{u_D}\right) = Q_m - \rho_f\alpha\dot{\varepsilon}$$

where

$$\boldsymbol{u_D} = -\frac{\boldsymbol{\kappa}}{\eta}\left(\nabla p + \rho_f\ddot{\boldsymbol{u}} + \rho_f\boldsymbol{g}\right)$$

3

Results and discussion of the analytical solution

In this chapter, the results of the analytical solution of the linear poroelastic model are presented and discussed. First, the solution is applied to the one-dimensional soil bar in order to get more insight into the ground response and the characteristics of the two different wave modes. More specifically, a parametric study was conducted for two characteristic frequencies and the influence of the various soil parameters on the response is evaluated. Special attention is paid on the effect of the degree of saturation. The analysis focuses afterwards on the amplitude ratio and the phase velocity of the two different waves propagating in the poroelastic medium. As already mentioned, these waves were predicted by Biot (1956). Afterwards, the solution already presented in cylindrical coordinatesis compared with the cavity expansion solution according to linear elasticity for drained and undrained conditions. The effect of the radius of the cavity, as well as the pore pressure are of high interest.

3.1 Infinitely long soil bar

In this section, the results obtained from the analysis of the 1D wave propagation in a poroelastic medium are presented. The load is sinusoidal according to the boundary conditions (equations (2.32) and (2.33)). The amplitude of the load is chosen to be p_0 = 770kN/m^2, because this load causes 1cm displacement at the boundary where it is applied according to linear elasticity for the soil properties selected. These are summarized in Table 3.1. The parametric study is conducted for two frequency values: f = 5Hz and f = 0.25Hz. The spatial domain of the analysis is selected to be equal to 2km discretised every 20cm so that the evolution of stresses and displacements with distance becomes clear. The time steps are selected according to the value of frequency applied for each analysis. Therefore, the first set of analyses (f=5Hz) assumes timeframe of 1s with dt=0.002s whereas the second set (f=0.25Hz) assumes timeframe of 10s with dt=0.02s.

Table 3.1. Soil properties selected for the analysis

Soil Property	Minimum value	Average value	Maximum value
Young's modulus, E (Pa)	10^6	10^7	10^8
Poisson ratio, v	0.3	0.3	0.3
Porosity, n	0.3	0.375	0.45
Hydr. Conductivity, k (m/s)	10^{-6}	$5*10^{-4}$	10^{-3}
Fluid Compressibility, C_f (1/Pa)	$9.919*10^{-8}$	$4.5*10^{-10}$	-

The analysis focuses on the relative displacement of the fluid and solid phases of the soil. In order to draw relevant conclusions, parametric investigation of the soil properties is conducted for both frequencies under examination. More specifically, the soil parameters of porosity, Young's modulus, permeability and fluid compressibility are modified to measure the influence they have on the ground response.

For all cases the density values selected for the grains and the pore fluid are:

$\rho_s = 2670 kg/m^3$

$\rho_f = 1000 kg/m^3$

The results of each case are presented in the Appendix B. They illustrate the time and space development of pore pressures, effective stresses and solid and fluid phase displacements. In addition, the amplitude of the displacements is plotted in terms of distance as well. This section focuses on the displacement over the course of time at the boundary which the pressure is applied on, in order to specify the relative movement of the fluid and the solid matrix. Additionally, the difference in the displacement of the fluid and solid caused by each wave is plotted for r=a according to the following formulas:

$$U_{P1} - u_{P1} = Im\left\{\frac{A_U e^{-(\omega/c)(r_1 - iq_1)x} e^{i\omega t}}{i\omega}\right\} - Im\left\{\frac{A_u e^{-(\omega/c)(r_1 - iq_1)x} e^{i\omega t}}{i\omega}\right\} \quad 3.1$$

$$U_{P2} - u_{P2} = Im\left\{\frac{B_U e^{-(\omega/c)(r_2 - iq_2)x} e^{i\omega t}}{i\omega}\right\} - Im\left\{\frac{B_u e^{-(\omega/c)(r_2 - iq_2)x} e^{i\omega t}}{i\omega}\right\} \quad 3.2$$

and the overall relative displacement $U-u|_{r=a}$ as well.

3.1.1 High frequency of excitation: f = 5Hz

First, the permeability and stiffness of the ground are investigated. The permeability is reduced to $k = 10^{-6} m/s$, which corresponds to fine sandy material. The Young's modulus is therefore modified accordingly to E = 1MPa. The wave propagation velocity is calculated equal to c = 25.6645 m/s in this case for the overall porous medium. The phase velocity of the first kind wave is c_{P1} = 1615.7 m/s, whereas the phase velocity of the second wave is c_{P2} = 0.1091 m/s. The definition of the phase velocity will be discussed in Chapter 3.1.3. Afterwards, the permeability is increased to $k = 10^{-2}$ m/s. The Young's modulus is selected accordingly, equal to E = 100MPa. The phase velocity of the first kind wave is c_{P1} = 1643.2 m/s while of the second kind is c_{P2} = 107.26 m/s. Figure 3.1 illustrates the displacement of the two phases of the ground at the cavity boundary for both sets of parameters. The two components respond in phase in the low permeability case and the amplitudes of both are also equal. In contrast to this, the amplitudes are not equal for the high permeable material, and there is also a phase shift observed, which was not the case previously. The effect of the second kind wave is more prominent in this case.

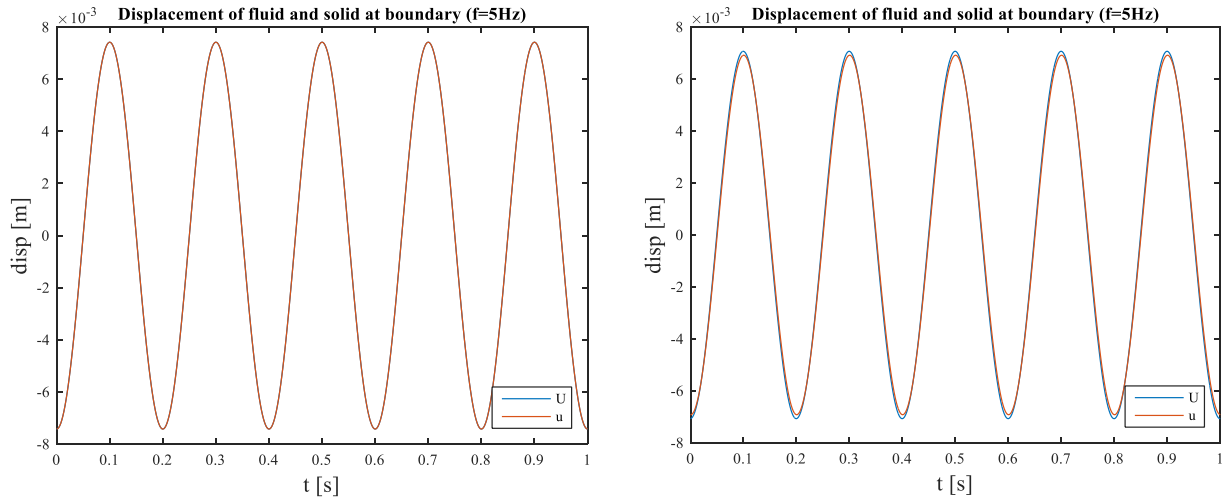

Figure 3.1. Fluid and solid displacement at the cavity for $k=10^{-6} m/s$ and $k=10^{-2} m/s$

Therefore, the relative displacement of the solid and fluid caused by the two waves and the overall one, which is actually the summation of the two, are plotted, according to equations (3.1) and (3.2). Figure 3.2 confirms the absence of the relative displacement, since it is of 10^{-8} order of magnitude. This slight relative displacement is caused by the wave of the first kind, because the imaginary part of its wavenumber is not absolutely nil. Although the second-kind wave is practically absent for such low permeability, for the highly permeable material the relative displacement caused by it is prominent. In the second graph of Figure 3.2 the phase shift of the slow wave can be detected, and this phase shift determines the phase shift of the overall relative displacement.

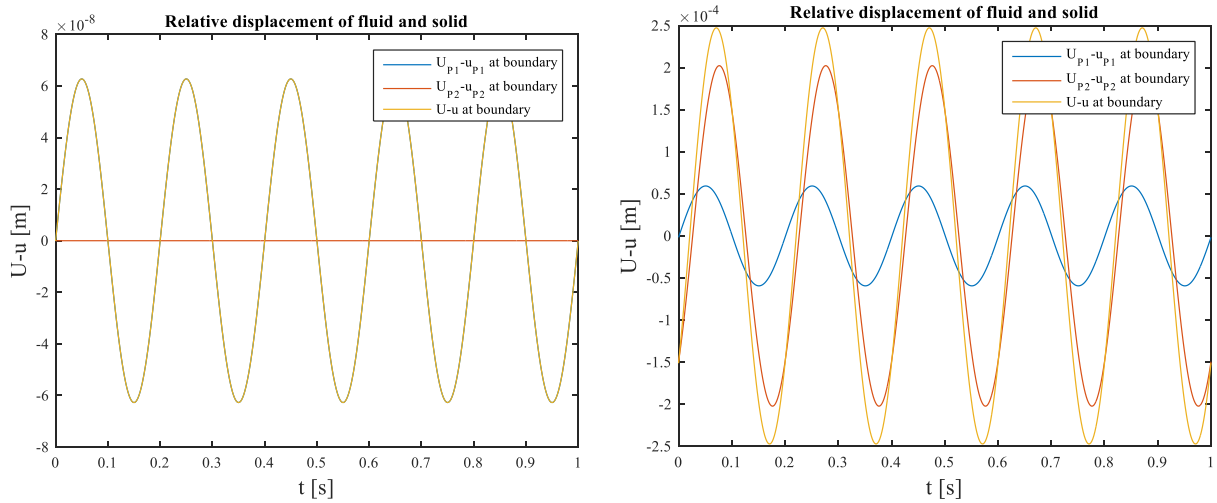

Figure 3.2. Relative displacement of fluid and solid at cavity for both propagating waves: k=10^{-6}m/s and k=10^{-2}m/s

Regarding the nearly saturated soil, the pores are assumed to contain air bubbles of 1% of the total void volume; i.e. degree of saturation S = 99%. This amount of air increases the fluid compressibility from $C_{f,w}$ = $5*10^{-10}$ m^2/N (compressibility of water) to $C_{f,eff}$ = $S*C_{f,w}+(1-S)*C_{air}$ = $0.99*5*10^{-10}+0.01*9.869*10^{-6}$ = $9.919*10^{-8}$ m^2/N. The effective fluid compressibility ($C_{f,eff}$) is calculated according to Vardoulakis and Beskos (1986). The phase velocity of the wave of first kind is c_{P1} = 149.16 m/s while of the second kind is c_{P2} = 5.93 m/s. At the cavity, the relative displacement of the two phases of the porous material is characterized by slightly different amplitude, but the phase shift is zero between the fluid and the solid matrix, as can be seen in Figure 3.3.

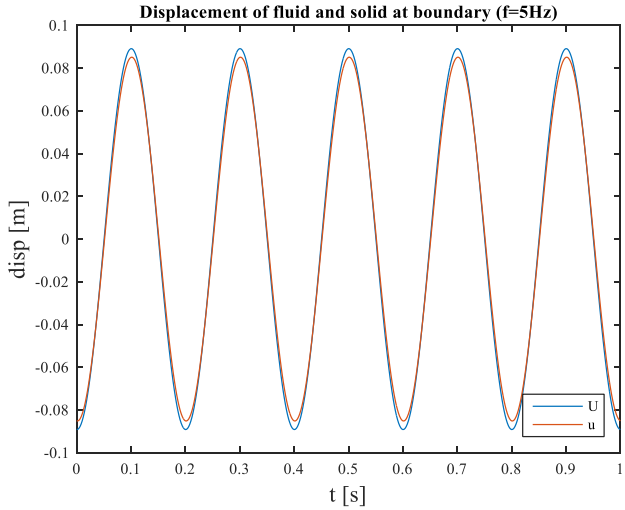

Figure 3.3. Fluid and solid displacement at the cavity for unsaturated soil (1% air content) and k=5·10^{-4}m/s

The relative displacement at the cavity is about 4.5mm out of the 9cm of amplitude and is caused mainly by the wave of second kind, as presented in Figure 3.4, where the relative displacement caused by the wave of first kind is very small.

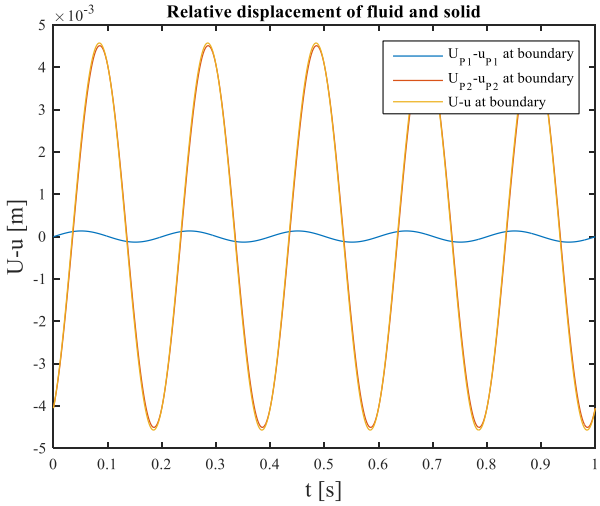

Figure 3.4. Relative displacement of fluid and solid at cavity for both propagating waves (1% air content) and k=5·10^{-4}m/s

The effect of the porosity of the saturated material is examined as well. Materials of high (n=0.45) and low (n=0.30) porosity are investigated. For the high porosity material the phase velocity of the first kind wave is c_{P1} = 1525 m/s while of the second kind is c_{P2} = 7.7 m/s. However, for the low porosity material, the phase velocity of the first kind wave is c_{P1} = 1756 m/s while of the second kind is c_{P2} = 7.71 m/s. The change in porosity has minor effect on the phase velocities of both wave modes and especially the slow one.

The two phases of the material move in phase with an almost negligible amplitude difference for both porosity extremes, as presented in Figure 3.5.

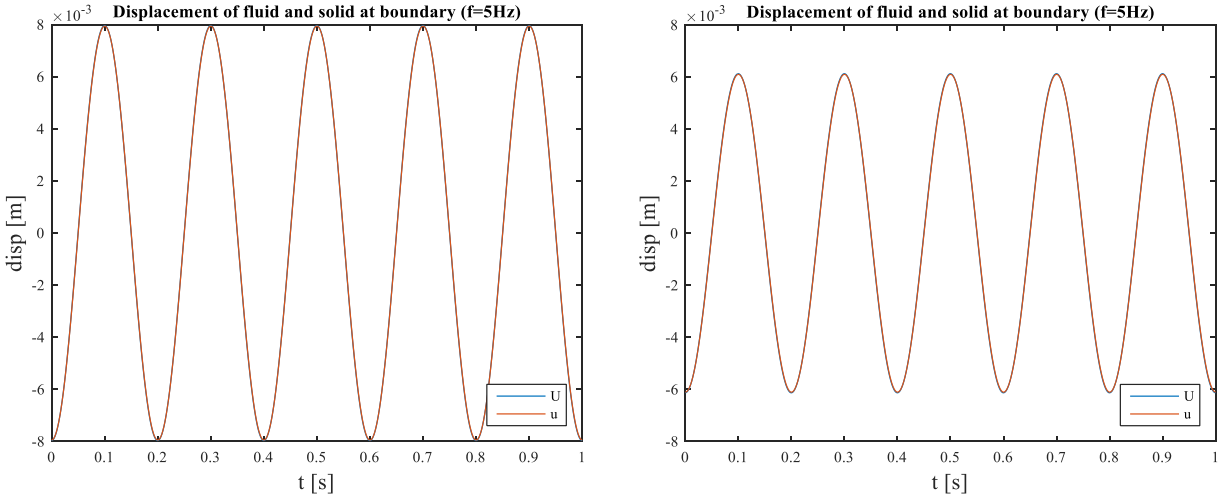

Figure 3.5. Fluid and solid displacement at the cavity (n=0.45 and n=0.30)

The aforementioned almost negligible amplitude difference between the two phases is pointed out in Figure 3.6. It becomes obvious that the difference is of a 10^{-5} order of magnitude, whereas the overall amplitudes are 6-8mm. The contributions of the two waves are approximately identical for both porosity extremes.

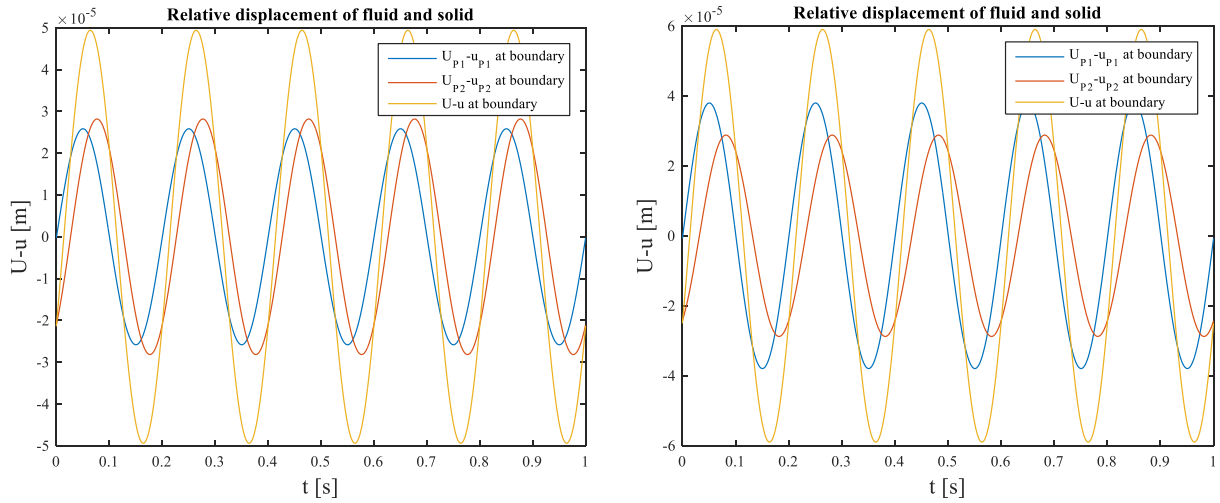

Figure 3.6. Relative displacement of fluid and solid at cavity for both propagating waves (n=0.45 and n=0.30)

3.1.2 Low frequency of excitation: f = 0.25Hz

Following an analogous procedure as for the higher frequency excitation, a fine sandy material is first compared to fine gravel. The permeability of the first material is k = 10^{-6} m/s and the Young's modulus E=1MPa. The permeability of the second material is increased to k=10^{-3} m/s, while the Young's modulus is E=100MPa. For the sand, the phase velocity of the first kind wave is c_{P1} = 1615.7 m/s, while the phase velocity of the second wave is c_{P2} = 0.024 m/s. The phase velocities of the two partial waves in this case of the gravel are c_{P1} = 1643.3 m/s and c_{P2} = 7.585 m/s. Compared to the high frequency, the velocity of the wave of first kind is equal to the one caused by high frequency excitation, but the one of the wave of second kind is almost four times lower for both materials.

Equivalently to the larger frequency excitation, the two phases of the low-permeability porous material move in phase with the same amplitude, as presented in Figure 3.7. However, when the frequency is low, the relative fluid-solid displacement is smaller in the highly permeable material compared to the high frequency. The differences in amplitude and phase shift of the solids and fluid seem to be almost negligible.

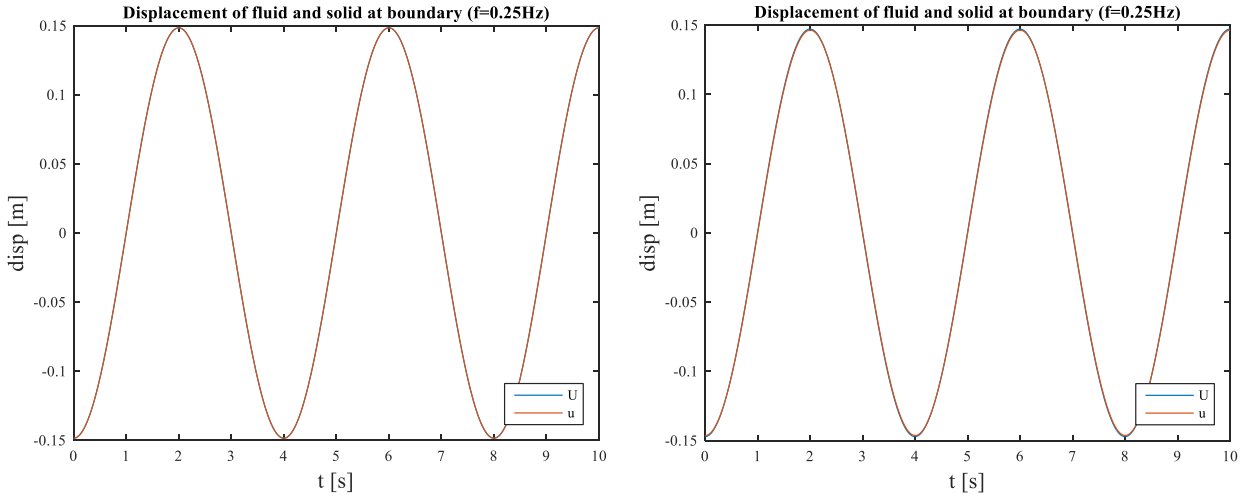

Figure 3.7. Fluid and solid displacement at the cavity (k=10^{-6}m/s vs. k=10^{-3}m/s)

Figure 3.8 presents in more detail the above mentioned observation. For the low permeability case, the amplitude difference of the fluid and the solid phase is of 10^{-8} order of magnitude while for the high permeability the overall amplitude difference of the two phases is about 1mm, and is caused mainly by the wave of second kind.

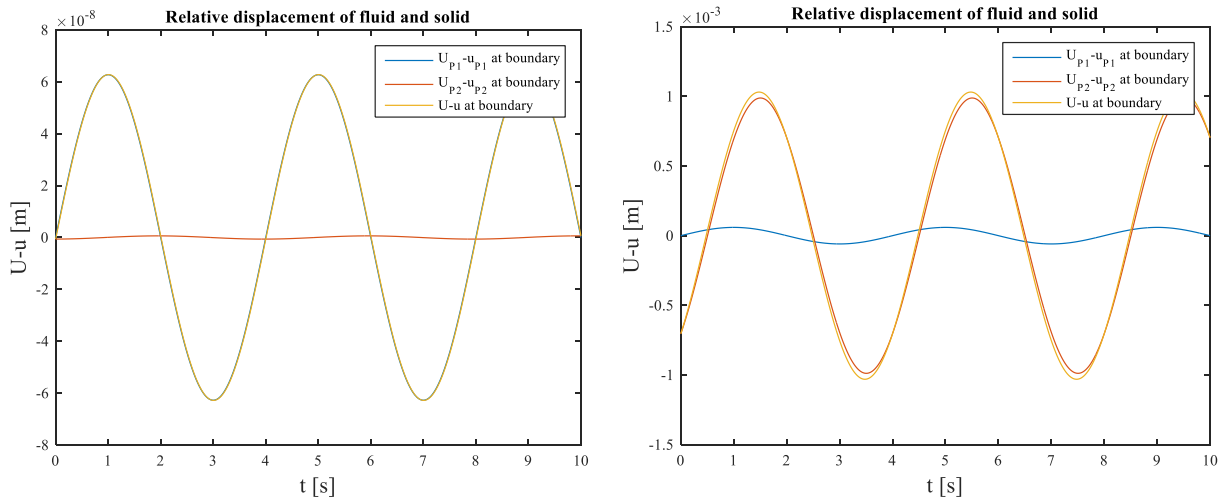

Figure 3.8. Relative displacement of fluid and solid at cavity for both propagating waves (k=10^{-6}m/s vs. k=10^{-3}m/s)

The next analysis assumes that the pores include 1% of the total pore volume entrapped air. In this case the fluid compressibility is increased to C_f = 9.919*10^{-8} m^2/N for confining pressure of 101.3 kPa (1atm). The phase velocity of the first kind wave is c_{P1} = 149.17 m/s while of the second kind is c_{P2} = 1.327 m/s. Similarly to the previous case, the phase velocity of the wave of first kind is almost equal with the one of high frequency. The wave of second kind is almost four times smaller in this case as well.

In comparison with the previous cases, the relative displacements of the fluid to solid matrix follows the same pattern. At the cavity, both material components move almost in phase with a small amplitude difference compared to the overall displacement (Figure 3.9).

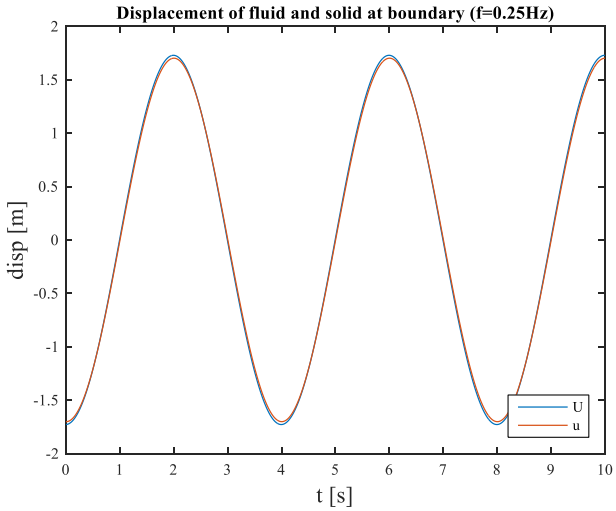

Figure 3.9. Fluid and solid displacement at the cavity for unsaturated soil (1% air content)

From Figure 3.10 it becomes obvious that the contribution of the first kind wave to the relative displacement of the two components is almost negligible. The slow wave is the one that causes the fluid move with both different amplitude and different phase shift to the solid material.

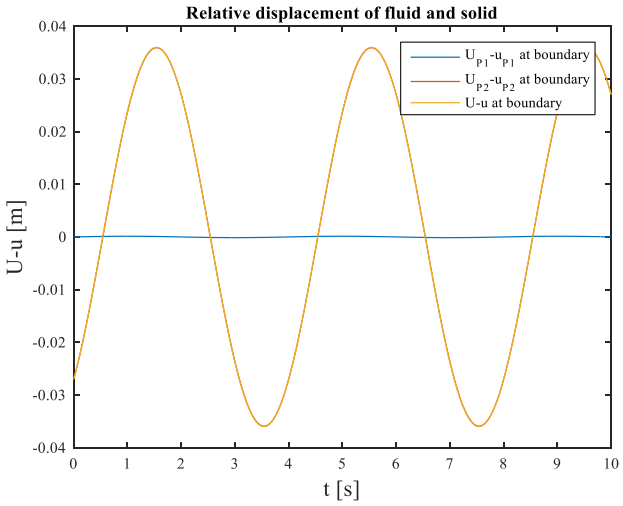

Figure 3.10. Relative displacement of fluid and solid at cavity for both propagating waves (1% air content)

Finally, the effect of porosity of the material is examined for low frequency excitation. The results follow exactly the same pattern as for the high-frequency excitation and hence will not be presented here. It was observed that the phase velocity of the second wave is approximately four times smaller while the one of the first-kind wave are approximately the same. In addition, the poroelastic effect is less dominant for this low-frequency analysis.

In general, it can be concluded that the porosity is a less sensitive parameter compared to the rest of the parameters investigated. More specifically, the permeability, degree of saturation and frequency can magnify the poroelastic effect. The latter is not only assessed by the difference in displacement of the solid and the fluid phase, but also by measuring the pore fluid pressure for various frequencies. This will be accomplished in Section 3.2.

3.1.3 Characteristics of the propagating waves

As already mentioned in Chapter 2.1.2, the equations of motion describe the propagation of two compression waves, a fast one (P1-wave) and a slow one (P2-wave). The phase velocity of each wave was calculated during the previous parametric analysis. The phase velocity describes the rate at each points of constant phase travel through the medium (Kramer, 1996). This term is defined to distinguish the aforementioned rate from the rate that a packet of waves travel through the medium. This packet of waves is produced by a transient disturbance and the corresponding speed is called group speed. In other words, it is the overall wave group that propagates with the group velocity (Metrikine and Vrouwenvelder, 2015). In the present work, as already observed from the results of the previous section, there are two waves propagating with different phase velocities. In the next sections, apart from the frequency of the forced vibration, oscillation in the natural frequency will be observed as well, as a result of the transient analysis. Therefore, It is meaningful in this stage to distinguish the phase velocity of each Biot wave. More specifically, in this section, it is explained how the phase velocities and the amplitude ratio of the two waves vary depending on the frequency.

According to equation (2.28), for instance, the component of the P1 wave is:

$$p = A_p e^{-(\omega/c)(r_1 - iq_1)x} e^{i\omega t} \tag{3.3}$$

which consists of a (complex) amplitude term (A_p), propagation in time ($e^{i\omega t}$) and propagation in space ($e^{-(\omega/c)(\mathrm{Im}(\gamma 1)-i\mathrm{Re}(\gamma 1))x}$). Elaboration of the space propagation exponential term gives:

$$e^{-(\omega/c)(Im(\gamma_1)-iRe(\gamma_1))x} = e^{\frac{i\omega}{c}*Re(\gamma_1)x-\frac{\omega}{c}*Im(\gamma_1)x} \quad 3.4$$

The first part of the exponent is imaginary and determines the amplitude decay, whereas the second part is the actual wave number. Bearing in mind that a propagating wave in space contains the term $e^{i\ell x}$, the combination with eq. (3.4) gives:

$$\ell = \frac{\omega}{c}Re(\gamma_1) = \frac{\omega}{c_P} \Rightarrow c_P = \frac{c}{Re(\gamma_1)} \quad 3.5$$

A second way to determine the phase velocity of the partial waves is by considering that the propagation in space terms is

$$e^{-i\omega S_{P1}x}$$

where S_{P1} is the slowness of the wave and can be generally calculated according to van Dalen (2013). Hence, in combination with the first part of equation (3.5):

$$c_{ph} = \frac{1}{Re(S_{P1})} \quad 3.6$$

Equations (3.5) and (3.6) result in the same values for different frequencies. Similarly, the phase velocity of the wave of second kind can be calculated for a possible shear wave, which does not exist in this case. Figure 3.11 illustrates the phase velocities of the compression and shear waves. There is a critical value of frequency, the rollover frequency, where the inertia and the viscous effects are of the same order of magnitude (van Dalen, 2013). The value of that frequency is:

$$\omega_c = \frac{\eta n}{\kappa \rho_f \tau} = 3270 rad/s \quad 3.7$$

for the selected average soil properties which are mentioned in Table 3.1.

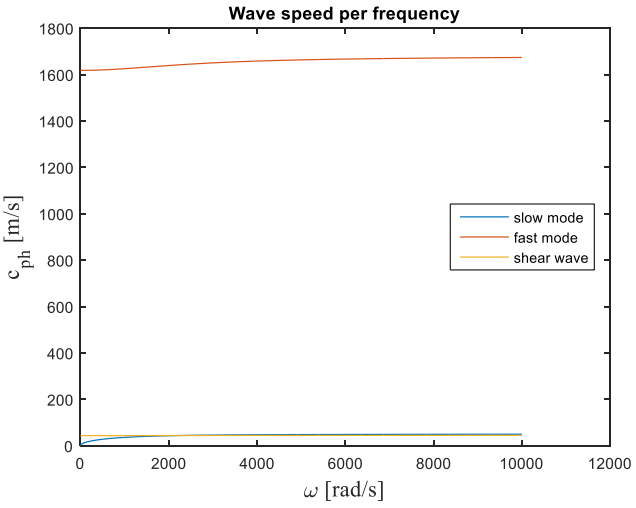

Figure 3.11. Phase velocities of all partial waves for various frequencies

In addition, one can calculate the amplitude ratios caused for various frequencies between pore fluid and solid matrix by considering equations (2.29) and (2.31):

$$w = w_{P1} + w_{p2} \quad 3.8$$

$$v = v_{P1} + v_{p2} = \beta_{P1} w_{P1} + \beta_{P2} w_{p2} \quad 3.9$$

where β_{P1} and β_{P2} are complex numbers which are calculated using equations (3.22) and (3.23) of van Dalen (2013). Figure 3.12 shows the frequency dependence of the absolute value of the amplitude ratio (pore fluid displacement over solid matrix displacement) for the three propagating waves. For frequencies tending towards zero the fast mode and the shear wave cause the two material components to vibrate with the same amplitudes. The slow wave causes relative flow of the fluid which is 1.7 times greater than the solid matrix. When the frequency is equal to the rollover frequency, the curves exhibit an inflection point.

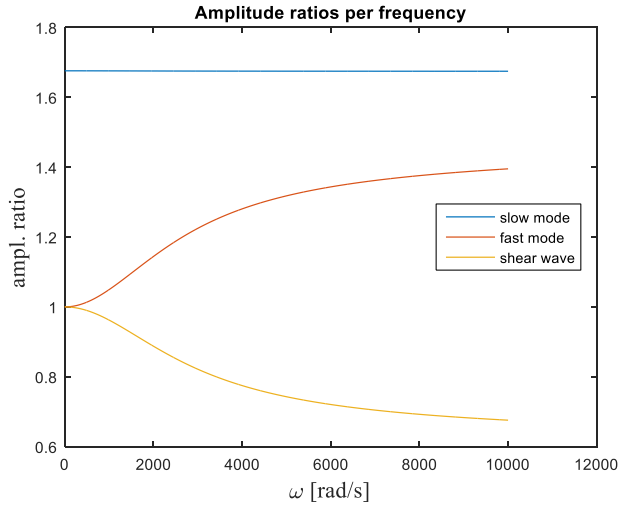

Figure 3.12. Solid matrix over the pore fluid displacement ratio for the three propagating waves and for various frequencies

3.1.4 The influence of air content on the displacement

In Chapter 2.1.2 it was observed that the displacement in the porous medium of both the solid and the fluid phases can increase significantly when 1% of air content is entrapped in the pores. In this section, the displacement of the boundary, which is where the excitation is applied, is calculated for various air contents or, in other words, for various effective fluid compressibility. In general:

$$\frac{1}{K_{f,eff}} = \frac{S}{K_f} + \frac{(1-S)}{K_{air}} \Rightarrow C_{f,eff} = S \cdot C_f + (1-S) \cdot C_{air} \qquad 3.10$$

where K_i are bulk moduli and C_i the respective compressibilities.

It has to be noted that the present analysis is an approximation of the behaviour of the nearly poroelastic medium, based only on the effective compressibility of the pore fluid. In fact, the response is expected to be more complex due to the development of an extra pressure between the water and the air bubbles; the capillary pressure. This component is expected to add extra stiffness to the overall response. However, the detailed analysis of this phenomenon lies beyond the scope of the present research.

According to equation (3.10) the effective fluid compressibility is determined for various degrees of saturation. The range of the latter is S=95-100%. For each degree of saturation, the maximum fluid displacement is calculated at the boundary. The fluid displacement option has been chosen instead of the solid particles because, as proven by Figure 3.3 and Figure 3.9, that it is slightly larger. The analyses conducted for both the low (f=0.25Hz) and the high (f=5Hz) frequencies and the respective results are summarized in Table 3.2.

Table 3.2. Various air content and the respective displacement on the boundary for both the low and high frequency

Saturation (%)	Air Content (%)	$C_{f.eff}$ (m^2/N)	u_{max} (m) (f=5Hz)	u_{max} (m) (f=0.25Hz)
100	0	5E-10	0.00096	0.019
99.5	0.5	4.98425E-08	0.0089	0.174
99	1	9.9185E-08	0.0115	0.224
98.5	1.5	1.48528E-07	0.0132	0.255
98	2	1.9787E-07	0.0144	0.277
97.5	2.5	2.47213E-07	0.0153	0.292
97	3	2.96555E-07	0.016	0.3
96.5	3.5	3.45898E-07	0.0165	0.314
96	4	3.9524E-07	0.017	0.322
95.5	4.5	4.44583E-07	0.0173	0.329
95	5	4.93925E-07	0.0176	0.335

The respective displacements are plotted against the compressibility (Figure 3.13) and the degree of saturation (Figure 3.14). It can be observed that increase in air content indicates that the fluid is more compressible and the displacements are larger. However, the increase in displacements is rapid when the fluid is almost saturated and for large amounts of entrapped air it is asymptotic to a certain value (linear figures in the logarithmic compressibility values and exponential in the linear scale of the degree of saturation); the air content does not then play a significant role.

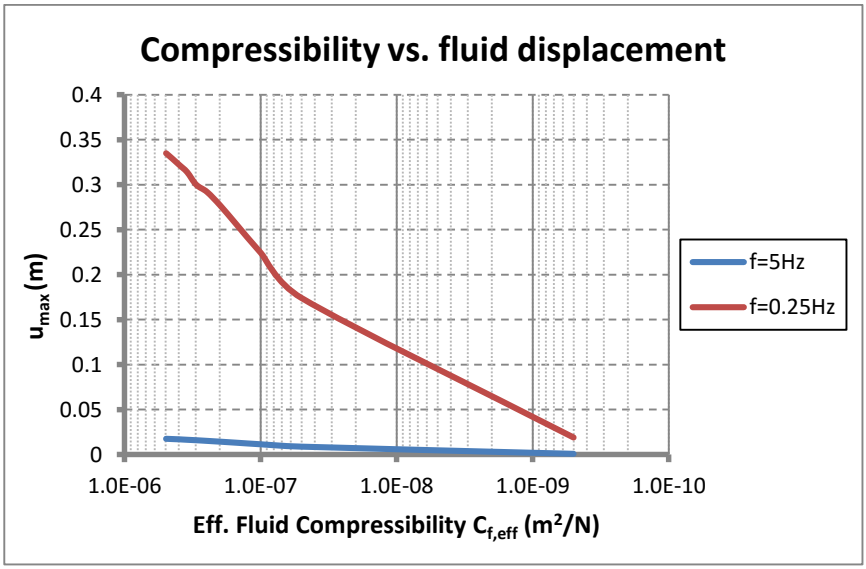

Figure 3.13. Fluid displacement on the loaded surface for various fluid compressibility (logarithmic) and both frequencies

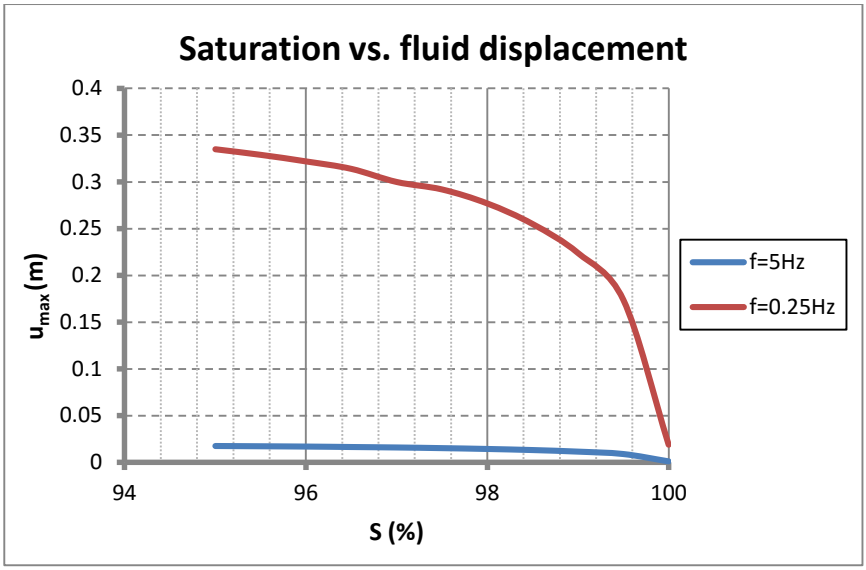

Figure 3.14. Fluid displacement on the loaded surface for various degree of saturation and both frequencies

3.2 Cylindrical axisymmetric cavity expansion in poroelastic medium

The solution of the governing equations which has been derived in Section 2.2.1, namely Equations (2.71) and (2.72), for 770kN/m^2 cavity pressure amplitude and 5Hz frequency is illustrated by the following figures over distance and time. The cavity radius is equal to r_0=0.1m. The displacement of the cavity is slightly larger than 1cm and it decays rapidly, as shown in Figure 3.15. The effect of geometrical damping is present in this case, in contrast to the one dimensional analysis.

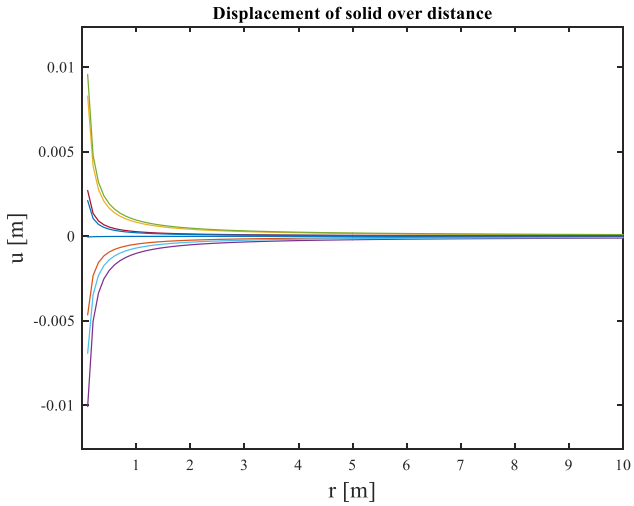

Figure 3.15. Displacement of the solid particles within 10m from the cavity and various time snapshots

Figure 3.16 illustrates the response over time of various positions away from the cavity. The phase shift is almost negligible in this case.

Furthermore, in order to determine the pore fluid oscillations, the difference of the displacements (U-u) is plotted in Figure 3.17. The largest difference in displacement is observed at 30cm away from the cavity and it is about two orders of magnitude lower than the total displacement of the solid particles, estimated by comparing the maximum value of 10^{-5}m with the corresponding value of u from Figure 3.15. In general, the relative displacement is expected to be the largest at the cavity. This was not observed here because of the boundary condition chosen (u=U at r=r_0) to derive the solution.

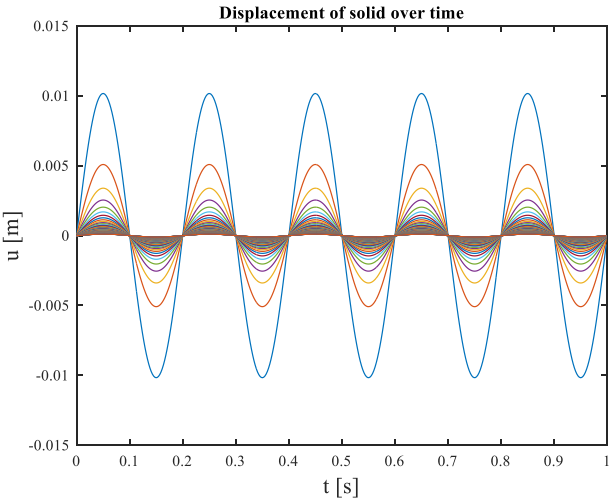

Figure 3.16. Displacement of solid particles over time for various locations from the cavity

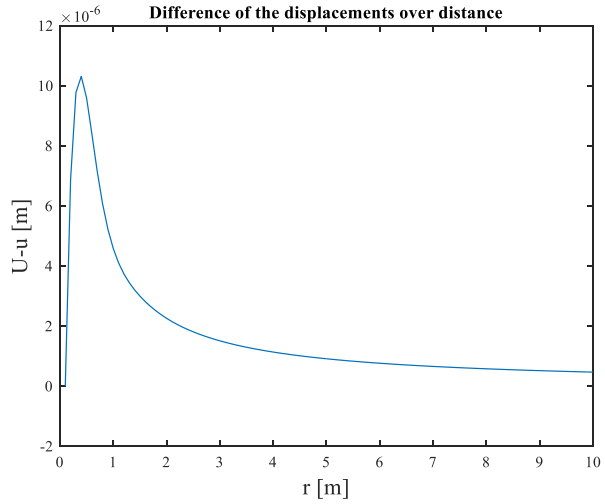

Figure 3.17. Difference of pore fluid and solid particles displacement within the first 10m from the cavity

Although the relative displacement seems to be negligible for the specific characteristics of soil and excitation, it is proven to be present at short distances from the cavity. The influence of the poroelastic effect is examined later in this section in the frequency domain for various soil and cavity properties.

3.2.1 Fully saturated poroelastic medium

The displacement of the cavity in the frequency domain is compared with the respective linear elastic solution. The derivation of the analytical linear solution has been derived in Section 1.2.3. Two different approaches are considered for the linear elastic model: drained and undrained responses. First, fully drained analysis is considered. Assuming a soil specimen which is exposed to atmospheric pressure, the fluid contained in the pores can flow freely out of the solid matrix. The response is governed by the Young's modulus and the Poisson ratio, which are the basis to calculate the Lamé constants. Second, the elastic parameters calculated for the drained case are applied to the poroelastic model. It has to be noted that in this case there are more parameters that govern the solution, such as permeability, compressibility of the components, porosity and fluid viscosity, which are not influential in the drained behaviour. Finally, undrained conditions are considered in the linear elastic model. According to them, if a saturated soil

specimen is considered sealed, the fluid cannot flow out of the interstitial space. This leads to decreased compressibility. The undrained elastic parameters are calculated as follows:

The undrained bulk modulus is determined by the Biot constants R and Q as follows (Detournay and Cheng, 1993):

$$K_u = \frac{(Q+R)^2}{R} + K \tag{3.11}$$

This value differs by 4G/3 from the undrained P-wave modulus (denoted as H by Biot), which is the 1D stiffness. The shear modulus (G) remains equal to the drained case, because the fluid does not offer any additional shear stiffness to the system. Using these variables (K_u and G), the undrained Young's modulus and the Poisson ratio are calculated as follows, so that the equivalent undrained Lamé constants can be determined (only λ because the shear modulus μ=G remains unchanged):

$$E_u = \frac{9K_uG}{3K_u+G} \tag{3.12}$$

$$v_u = \frac{3K_u-2G}{2(3K_u+G)} \tag{3.13}$$

In Figure 3.18 the amplitude and the phase shift of the displacement of the cavity is plotted for a frequency range of f = 0-200Hz. At frequencies close to zero (static case), the poroelastic model predicts approximately equal displacements to the linear elastic drained model. However, at frequencies close to the resonance, the poroelastic model predicts more than double displacement. The undrained linear elastic analysis predicts equal amplification to poroelasticity, but at a much lower frequency.

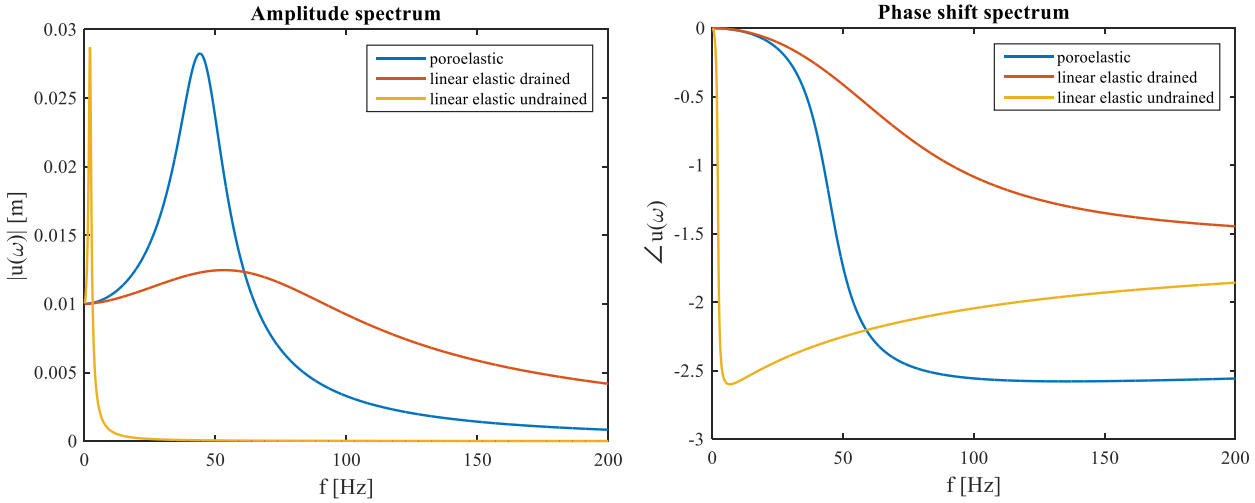

Figure 3.18. Comparison of the amplitude and phase shift spectrum of the poroelastic model with the linear elastic; both drained and undrained analysis

As the frequency becomes larger, the amplitude of the cavity displacement attenuates faster according to the poroelastic model than according to drained linear elastic analysis and much slower than according to undrained analysis. The latter is associated with the Poisson ratio. As the incompressible limit is reached (v=0.5) the response becomes very stiff so that the amplitude decays very fast (Verruijt, 2010). Furthermore, the phase shift calculated using the two models is compared. According to all models, the response of the cavity gets out-of-phase at the respective resonance frequency. The transition is much smoother according to the drained linear elastic model, leading to a value of (-π) at high frequencies. The poroelastic model predicts a phase shift of about (-5π/6) at high frequencies. Finally, according to

undrained analysis the response is never in phase. Already at very low frequencies it becomes (-5π/6) and then increases, to reach the value of (-π) asymptotically at very high frequencies.

3.2.2 Partially saturated medium

In this section, the effect of the fluid compressibility is evaluated. First, 1% air inclusion in the pores, which results in a pore fluid compressibility of C_f=9.9*10^{-8}m^2/N, is assumed to apply. Figure 3.19 illustrates the amplitude and the phase shift of the response of such material in the frequency domain according to the poroelastic model and the linear elastic. The poroelastic response lies between the linear elastic drained and undrained analysis. In particular, according to poroelasticity, resonance occurs at about the same frequency as the drained linear elastic case, but with larger peak amplitude which is equal to the undrained analysis, the only difference being that undrained resonance peak occurs in lower frequencies. Regarding the phase shift, the response goes out of phase in all three models. According to poroelasticity, this occurs later than with the undrained linear elastic model and earlier than in the drained analysis.

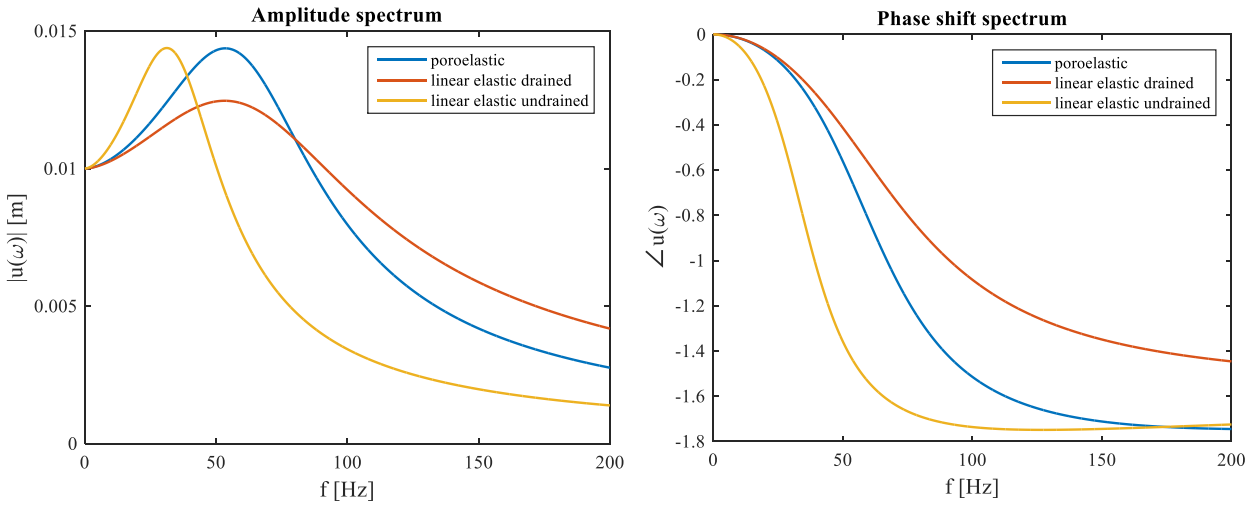

Figure 3.19. The amplitude and phase shift spectra of a non-saturated (S=99%) material response (poroelastic vs. linear elastic model)

3.2.3 Highly permeable saturated poroelastic medium

Figure 3.20 presents a comparison between the amplitude spectra corresponding to a highly permeable material with hydraulic conductivity k=10^{-3}m/s (loose marine sand) and a material with low hydraulic conductivity (k=10^{-6}m/s), analysed using the poroelastic model and the linear elastic model. At the cavity boundary, the resonance peak amplitude of the poroelastic response is almost the same in both cases, meaning that permeability does not significantly influence the cavity response. More specifically, the peak resonance amplitude of the rather impermeable material is almost equal to the resulting amplitude of the undrained analysis, as it was expected. For the more permeable material the resonance peak amplitude was expected to converge to the drained analysis but it only reduces slightly, compared to the impermeable material. Similar pattern is observed for the phase shift as well, and therefore the perspective figures are not presented here.

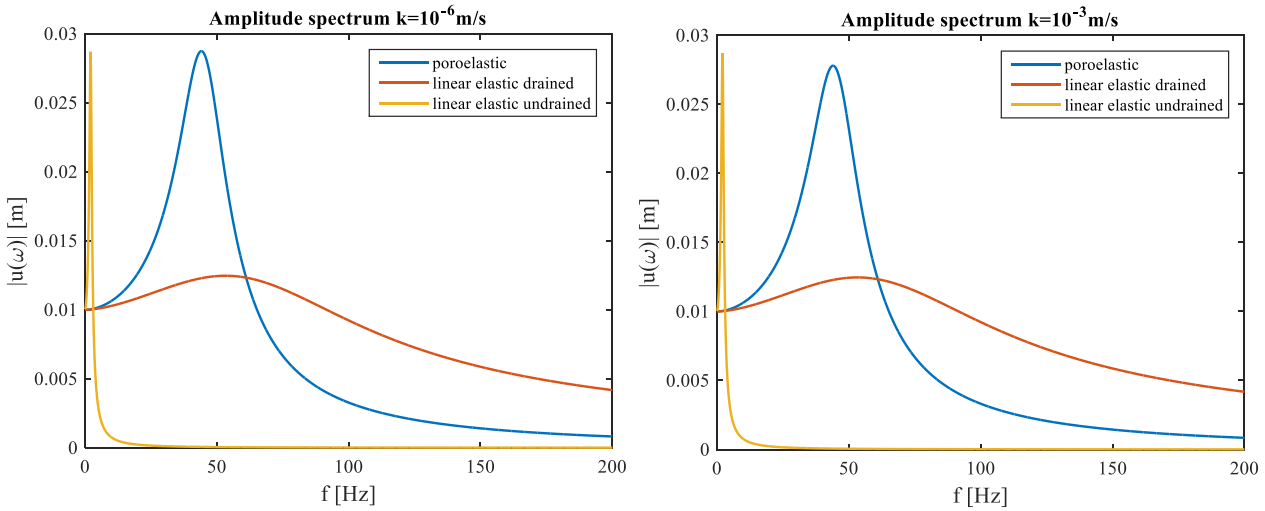

Figure 3.20. The amplitude and phase shift spectra of a highly permeable material response (poroelastic vs. linear elastic model)

3.2.4 Influence of the cavity radius

In this part, the respective spectra are displayed for a cavity with a radius of 5m, a characteristic value for a monopile, for instance. Figure 3.21 illustrates the amplitude and phase shift spectra of the large diameter cavity. Because the dimensions of the domain are larger, the absolute amplitude values are relatively larger in the larger radius case. However, the resonance frequencies are much lower compared to the small cavity. The ratio between the peak and static amplitude is slightly larger in the large radius case. In general, though, the same pattern as in the small cavity case is followed according both to poroelasticity and to the linear elastic analyses. The only significant difference is observed in the phase shift, which increases dramatically as the frequency increases, in the poroelastic case.

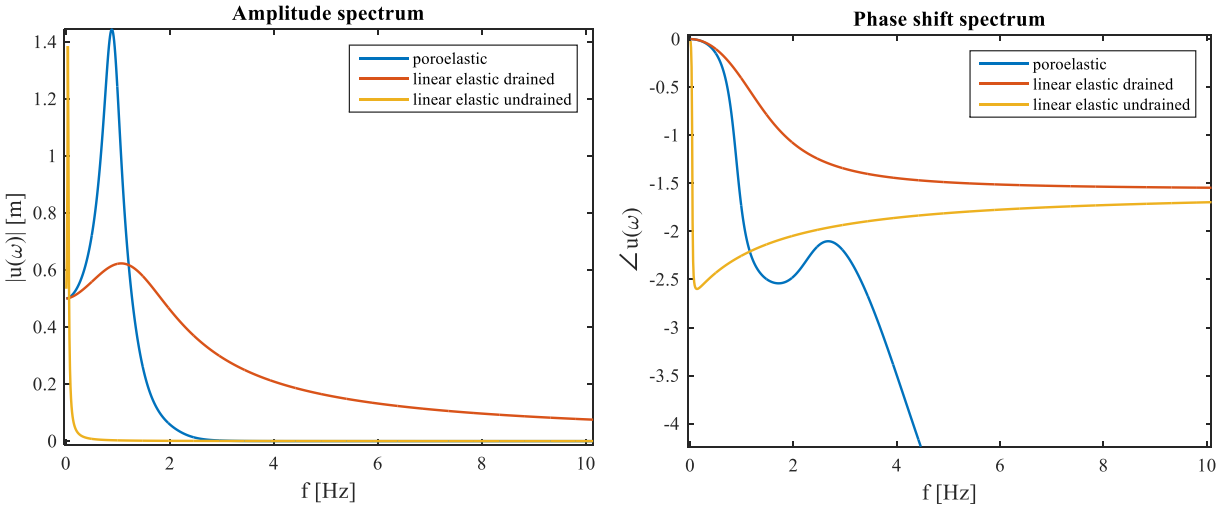

Figure 3.21. The amplitude and phase shift spectra for 5m cavity radius (poroelastic vs. linear elastic model)

It has to be noted that by comparing Figure 3.21 with Figure 3.18, the spectra can be seen to have shifted to lower frequencies when the radius of the cavity increases. However, the poroelastic response lies between the undrained and the drained elastic response. Consequently, the response figures are qualitatively equivalent. However, if one focuses on a specific frequency, the response of a CPM cavity can be comparable to the drained analysis, but the response of an offshore wind turbine, for instance, is rather comparable to the undrained.

This observation is of high interest when physical modelling of monopile structures under dynamic loading is conducted. It can be accomplished using the dynamic cone pressuremeter test. However, for such applications one has to extrapolate the results accordingly. The test should be conducted at larger frequencies than the ones that it attempts to model when the target radius is larger than the probe. However, this needs further investigation due to the fact that up to now the damping due to friction between the grains has not been analysed. This might change the response even more.

3.2.5 Pore pressures calculation

This part deals with the pore pressure development at various frequencies. We concentrate on the cavity boundary for this calculation as well, where the water seepage is more intensive. The pore pressures are determined using the following equation (van Dalen, 2013) and they are related to the derivatives of the displacements:

$$p = -\frac{Q\varepsilon + R\epsilon}{n} \tag{3.14}$$

where (ε) is the volumetric strain of the solid phase and (ϵ) of the fluid; they have both been defined by equations 2.48 and 2.49. Figure 3.22 illustrates the maximum pore pressures developed on the cavity boundary and the phase shift. Specifically for the pore pressure amplitude, the applied total stress is also plotted, so that the comparison of the two is clarified. It can be concluded that the pore pressures are likely to peak at values larger than the applied pressure, depending on frequency. For zero frequency (static case) the pore pressures are nil; only the applied pressure is transferred to the solid phase. On the other hand, for very high frequencies, the applied pressure is only borne by the fluid (pore pressures equal to applied pressure). Regarding the phase shift, unlike the displacements, the pore pressure exhibits an out-of-phase oscillation at low frequencies whilst for high frequencies the pressure tends to have zero phase shift.

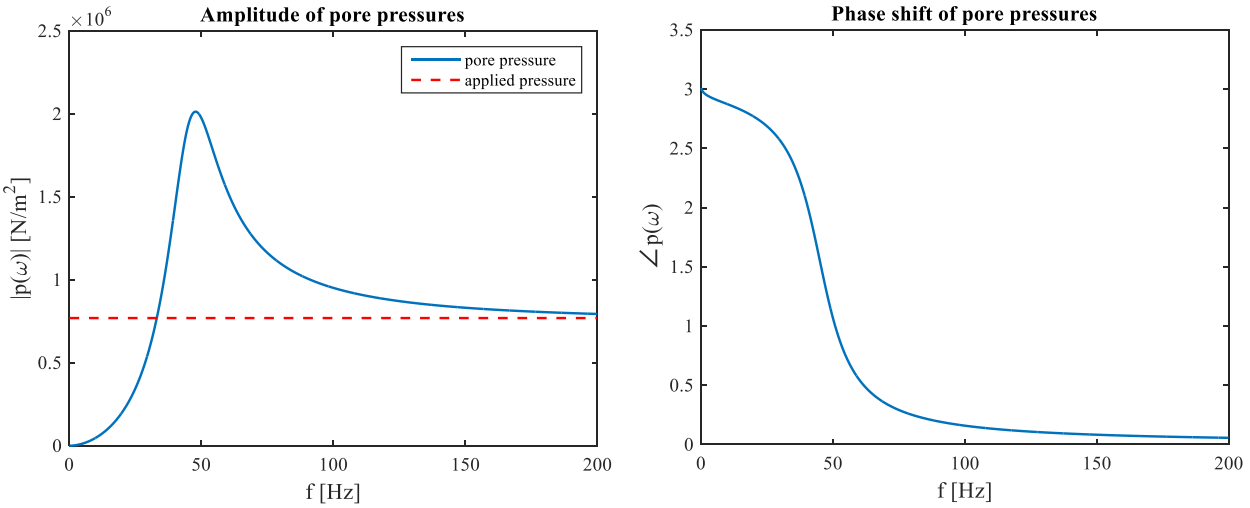

Figure 3.22. Amplitude and phase shift spectra of pore pressures

3.2.6 Dynamic stiffness determination

The response so far determined can be confirmed by the calculation of the dynamic stiffness for various frequencies. The dynamic stiffness is the ratio of the force excited to the system over the respective displacement:

$$|\hat{k}_{dyn}| = \frac{2\pi r_0 p_0}{|u|} \tag{3.15}$$

where the time terms have been cancelled out and thus, the amplitudes of the force and the solid particles' displacement are taken into account. Figure 3.23 indicates that the dynamic stiffness exhibits a minimum value where the resonance has been observed. The system responses the least stiff to that specific excitation frequency. For zero frequency (static case) there is a static stiffness value, unlike in the one-dimensional case, where the static stiffness is zero (infinite displacement).

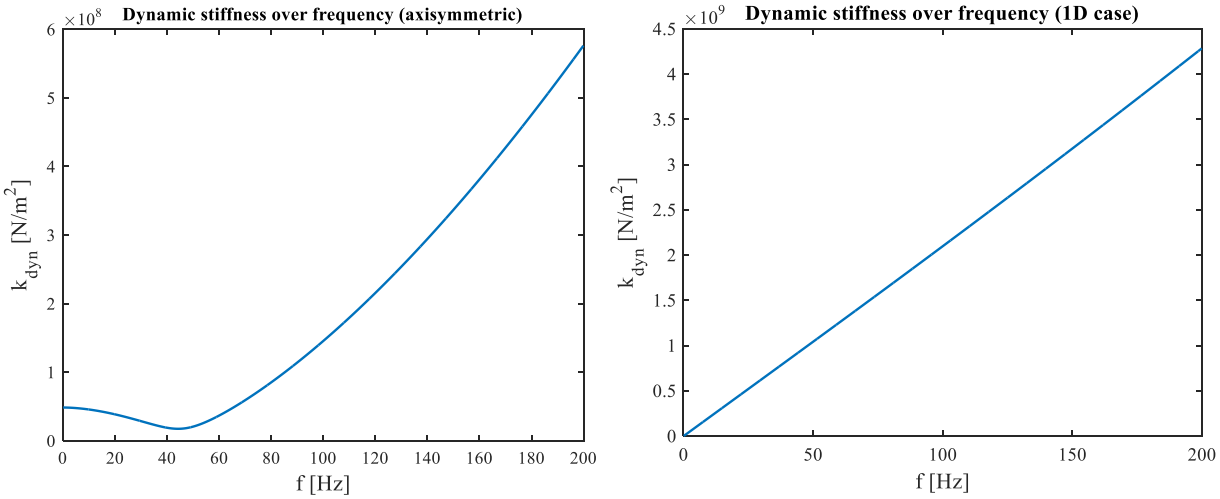

Figure 3.23. Dynamic stiffness of the system per frequency (axisymmetric vs. 1D problem)

3.2.7 Energy dissipation in poroelasticity

The force-displacement graph for cyclic loading indicates the energy dissipated per cycle as the area enclosed by the curve. The larger the area the more energy is dissipated per unit volume and the more intense the viscous damping is as well. For elastic response under harmonic loading, this area remains constant for every cycle. Consequently, one cycle is enough to determine this area. Two different cavity radii are under examination (r_0=0.1m and r_0=5m). It has to be noted that the dissipated energy is mainly due to radiation damping and is dependent on frequency. For the poroelastic analysis, additional dissipation occurs due to Biot viscous damping.

In Figure 3.24, the small cavity is considered to compare the respective force-displacement curve according to poroelasticity with the linear elastic case, for both drained and undrained analysis. Four different frequencies of excitation are examined: 0.25, 1, 5 and 25 Hz. The results indicate that for low frequencies the energy dissipated per cycle is considerably less than for high frequencies. More particularly, at very low frequencies (f=0.25Hz) the results of the three models are almost identical to each other. As frequency becomes larger (f=1Hz), the energy dissipation according to undrained linear elastic analysis is considerably larger than the drained elastic case, which is still similar to the poroealstic model. For larger frequency (f=5Hz), the poroelastic model slightly deviates from the drained linear elastic analysis, but still the energy dissipated per cycle is still comparable. In sharp contrast to this, if undrained conditions are assumed, the response is completely different. For even higher frequencies, for example when f=25Hz, the poroelastic model predicts larger damping and energy dissipation per cycle than the drained elastic model, whilst the undrained one predicts almost no energy dissipation, because the displacement is small compared to the other analyses. These results are in accordance with the amplitude spectra for all these models, which were presented in Section 3.2.1. For frequencies larger than the resonance frequency, the ellipsoidal curve is flipped, as a result of out-of-phase response. It has to be

noted that this is only related to the phase of the response and not to expansion of the material, which is definitely not the case.

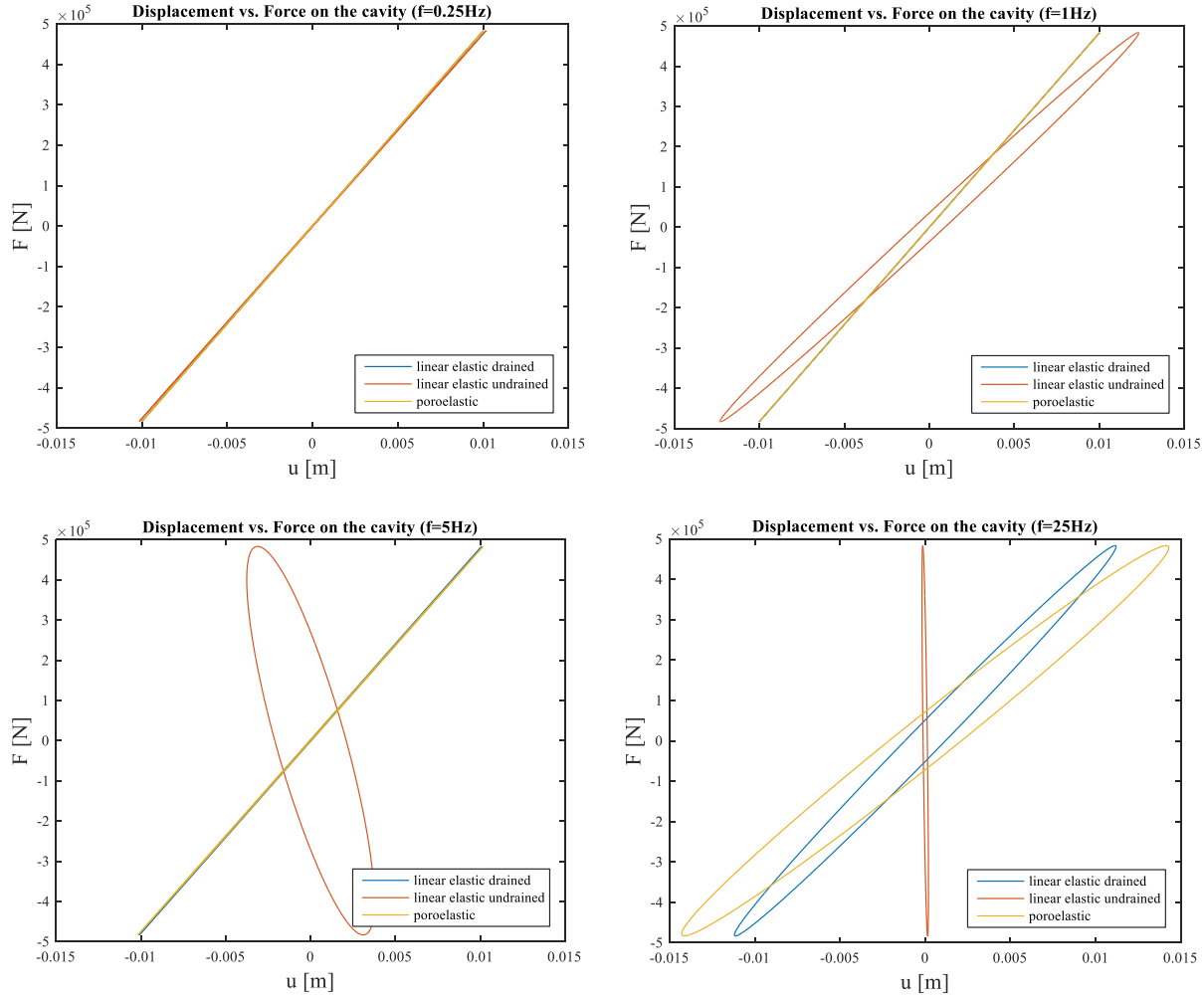

Figure 3.24. Force-displacement graphs for various frequencies and small cavity radius (r_0=0.1m): Poroelasticity is compared to linear elasticity (both undrained and drained conditions)

The next set of graphs which is represented in Figure 3.25 illustrates the energy dissipation for various frequencies, considering the large cavity radius (r_0=5m). The graphs follow the same pattern as for the small cavity, but the damping area grows more rapidly at lower frequencies. More specifically, the force-displacement graph for poroelastic behaviour deviates from the drained elastic already at a frequency of 0.25Hz, and the response is completely different at 1Hz. Accordingly, the undrained behaviour graph is almost completely degenerated (converged to zero displacement) at f = 0.25Hz. For frequencies larger than about 3Hz the poroelastic graph is degenerated as well and only the drained one still exhibits a significant damping area. The degeneration occurs due to very small – almost zero – displacements predicted for such frequencies, as they are reflected in Figure 3.21.

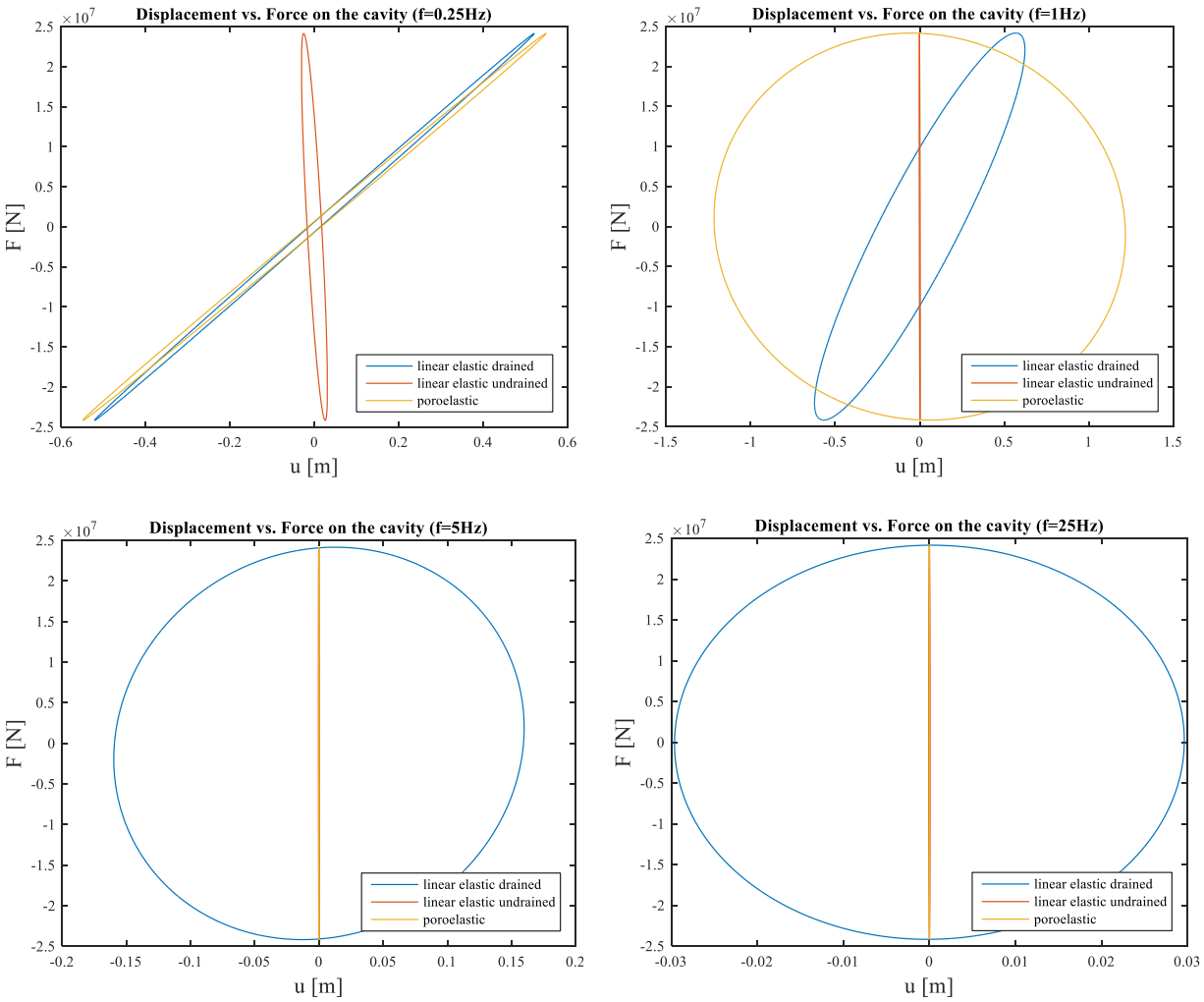

Figure 3.25. Force-displacement graphs for various frequencies and large cavity radius (r_0=5m): Poroelasticity is compared to linear elasticity (both undrained and drained conditions)

4

The numerical model

As already mentioned, apart from the analytical solution of the linear poroelasticity, a numerical approximation is implemented as well. The scope for a numerical analysis is to simulate the ground response in a more realistic way, because the soil almost never behaves linearly. The numerical model is built using the software package COMSOL Multiphysics. This package involves a powerful interactive user-friendly environment to study scientific and engineering problems. The build-in physics interfaces and material properties provide the user with a simple and effective way to build the model under examination and possibly couple different physics modes. Thus, it allows physical quantities instead of equations to be defined. The implemented equations though are modifiable, and therefore the user can adjust the simulator to their needs. Various types of studies can be conducted including stationary or time-dependent, linear or non-linear, frequency-dependent or eigenvalue problem analyses. As a result, COMSOL Multiphysics consists an appropriate environment to carry on with the finite element analysis of the case under research in this dissertation.

To start with, the cavity expansion problem is studied in the frequency domain according to Section 2.3, and more specifically according to the equations of motion (2.84) and (2.85). Afterwards, the analysis is conducted in the time domain, because of the reasons described in Section 2.3. The governing equations in this case are (2.120) and (2.121). The main purpose of a time-domain simulation is the inclusion of soil nonlinearity. The latter is introduced through dependency of the shear modulus on shear strain invariants. More details about the nonlinear model will follow in this chapter.

4.1 Linear poroelastic analysis in the frequency domain

The scope of this first analysis is to build a trustworthy model in terms of geometry and material properties in order to use it in the following. The main advantage is that there is an analytical solution already to be compared with, so that the numerical error can also be quantified. Additionally, a numerical solution using the u-p approximation by Zienkiewicz et al. (1999), which does not take into account the relative acceleration of the fluid and the solid matrix, can be conducted in order to confirm validity of this assumption in the frequency range under investigation.

For the frequency domain analysis the ‘Poroelastic Waves’ interface is chosen, which has the capabilities to model linear elastic wave propagation in a poroelastic medium. It includes special features to model domains of porous material as well as boundary conditions for possible porous-fluid and porous-solid interaction (COMSOL User’s Guide). The domain is cylindrical axisymmetric, thus the “2D axisymmetric” geometry feature is selected, which by default involves modelling in the r-z coordinate system. Therefore, a cavity of 10cm radius is modelled, in accordance to the radius chosen so far. The cavity is infinitely long, thus a height of 50m is arbitrarily chosen. The width of the domain is selected to be 100m. The

aforementioned geometry features are modelled as rectangles, so only a 'slice' of the cylinder is analysed. This 'slice' is assumed to be repeated in 360° around the z-axis.

Regarding the material properties, these are set equal to the average material properties chosen so far (see Table 3.1). The core linear elastic material properties are selected to be the bulk modulus (K) and the shear modulus (G), in order to maintain consistency with the analytical solution. In any case, these variables take place in the definition of Biot parameters. However, it is more logical to define the material linear elasticity through the Young's modulus (E) and Poisson's ratio (ν). Therefore, the latter are defined as model parameters and the bulk and shear modulus are expressed as functions of them. This allows possible further parametric investigation on Young's modulus, relative to the one conducted in Section 2.1.2. In the same way, more soil parameters, such as the porosity, hydraulic conductivity, fluid compressibility are defined in the section 'Parameters' for a possible parametric sweep.

As per the boundary conditions, because poroelasticity couples solid mechanics and fluid flow according to Darcy's law, the boundary condition at the cavity needs to be defined both by a prescribed mechanical condition, in terms of either load or displacement, and by a prescribed hydraulic condition. Hence, for the cavity boundary the loading condition was selected sinusoidal pressure with an amplitude of 770kPa, which is identical to the pressure applied for the analytical solution. Additionally, the cavity is impermeable, so the second boundary condition is a no-flow condition. In COMSOL Multiphysics these two boundary conditions are combined under the selection of the 'Septum Boundary Load'. This node prescribes an impermeable membrane which is subjected to pressure. The user has to define the surface density, which in this case is assumed nil, and the amplitude of the total pressure, which is already mentioned. At r=100m the domain is connected to a Perfectly Matched Layer. The latter is a domain boundary which allows fast attenuation of the incoming waves, so that no reflection occurs. Its origin was the equivalent problem of the electromagnetic wave propagation and it is an evolution of the matched layer, able to absorb waves incident at any angle (Berenger, 1994). The principal of a Perfectly Matched Layer (PML) is the same as the absorbing boundary layer: A wave is attenuated and decays exponentially, based on complex coordinate stretching:

$$\bar{x} = x + i\not{f}(x) \Rightarrow \partial\bar{x} = \left(1 + i\frac{\partial\not{f}}{\partial x}\right)\partial x, \qquad \frac{\partial\not{f}}{\partial x} = \frac{\sigma_x(x)}{\omega} \tag{4.1}$$

where $\sigma_x(x)$ is a step function (Johnson, 2007). This complex x-contour, which in the particular case is replaced by the r-contour, changes the oscillating waves into exponentially decaying waves outside the domain of interest without reflections. In other words, the PML imposes a complex-valued coordinate transformation to the selected domain that effectively makes it absorbing at a maintained wave impedance, and thus eliminating reflections at the interface (COMSOL Multiphysics User's Guide).

In general, the PML works perfectly only for exact wave equations. When it has to do with discretization, like the present analysis, small reflections still occur between the real domain and the PML because the discretization is still an approximation of the exact problem. Reflections can be made arbitrarily small as long as the medium is slowly varying, i.e. absorption has to be "turned on" more and more slowly. In this case, reflections tend to zero because of an adiabatic theorem (Johnson, 2007). For the present analysis, the PML is selected to extend to 200m, that means that its width is identical to the real domain. The boundary at r=200m has to be free, so the width of the PML is necessary to be large enough, that the reflected attenuating waves at r=200m do not re-enter the main domain for the selected value of the scaling factor.

Regarding the boundary conditions along the wave propagation direction (i.e. z=-25m and z=25m) are set to rollers, so that the whole domain oscillates along the r-direction. Afterwards, both domains are meshed. The mesh is selected mapped, with five elements within the PML and six waves per wavelength within the main domain of analysis. When one chooses for a fixed number of elements per wavelength, this number varies from six to ten (Marburg, 2002). The most critical wavelength is the shortest one, which corresponds to the phase velocity of the slow wave at the largest frequency under examination (100Hz) according to:

$$\ell = \frac{c_P}{f} \tag{4.2}$$

This leads to elements 2.7cm wide. Figure 4.1 presents the discretised computed domain and the Perfectly Matched Layer as well as the boundary load on the cavity and the rollers along the long sides, which prevent vibrations in the z-direction. It has to be noted that gravity has not been taken into account in the linear elastic analyses.

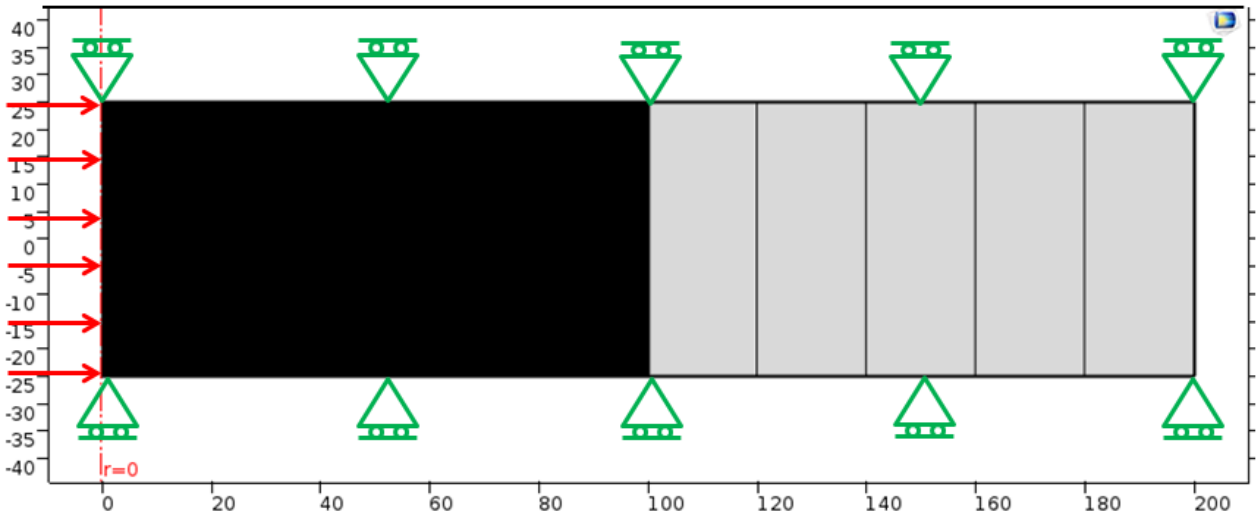

Figure 4.1. The discretised domains and the structural boundary conditions (horizontal axis: length, vertical axis: depth)

4.2 Linear elastic analysis in time domain

In this section, the linear poroelastic analysis is executed in the time domain, as an elementary stage before a nonlinear model can be introduced. For this model, the equations of motion have been derived in Section 2.3.3, with the appropriate additions of inertia and gravity effects. The inertia terms and the gravitational load are defined as body loads, so that they contribute to the first governing equation (2.120). The Darcy's velocity field taking part in the second equation is also enhanced with inertia terms, as a result of the substitution of the fluid momentum balance equation into the conservation of flow equation (see also Equation (2.122)).

Generally, the initial conditions should be incorporated in the analysis following the generation of the FE mesh and prior to any further analysis (Alliguer et al., 2015). This is to initialise the stresses in the most accurate way, representing the geological history of the material. According to Alliguer et al. (2015), two steps are required to accomplish this. First, one has to estimate the stress state at each Gauss point. Second, the global equilibrium has to be verified and the forces must balance before any further analysis. Both of these steps are conducted in a stationary way. However, for the present analysis only the gravitational loads will be applied as overburden pressure at the first study step and the stresses will be

applied as initial values for the time-domain analysis. Hence, the simulation consists of two study steps. These are the following:

- Application of gravitational load (stationary)
- Transient simulation of the cavity expansion (time domain)

One has to ensure that the effective stresses, which are the ones who determine the mechanical behaviour, should be precisely calculated and linked between the study steps. Consequently, the domain needs to be placed at a depth of 10m. Additionally, he cavity is assumed to be 0.50m long and the width of the domain is arbitrarily selected to be 30m.

The first study step assumes gravitational load acting on the domain. The load is modelled as a continuous boundary load which represents the weight of the overburden acting on the upper boundary (z=-9.75m). This is the mechanical boundary condition of the upper boundary. The self-weight of the domain is being ignored for the present analysis, since it is much smaller than the weight of the overburden. The rest of the mechanical boundary conditions include rollers along the lower boundary at z=-10.25m in order to avoid infinite displacements in the z-direction and along the side boundaries to allow sliding and hence vertical displacements of the domain as the vertical load is introduced. Regarding the hydraulic boundary conditions, constant hydrostatic pressure (Dirichlet boundary condition) is set to all the boundaries. It is assumed that the gravitational load is established and the equilibrium is gained before the cavity of the pressuremeter expands. In other words, it simulates the prebored pressuremeter test assuming that there is no gap between the borehole and the probe. In addition, this approach allows for water outflow of the domain when pore water pressure deviates from the hydrostatic. The initial conditions are zero displacement and hydrostatic pore pressure. The gravitational load is applied in a stationary way and the domain is simulated using the 'Poroelastic' interface. The mesh is implemented by using quadratic free triangular elements and the density is chosen as 'Coarser'. This option allows for accurate results and at the same time it does not consume much time and memory. Part of the mesh is shown by Figure 4.2. The gravitational load causes a settlement of -0.08mm.

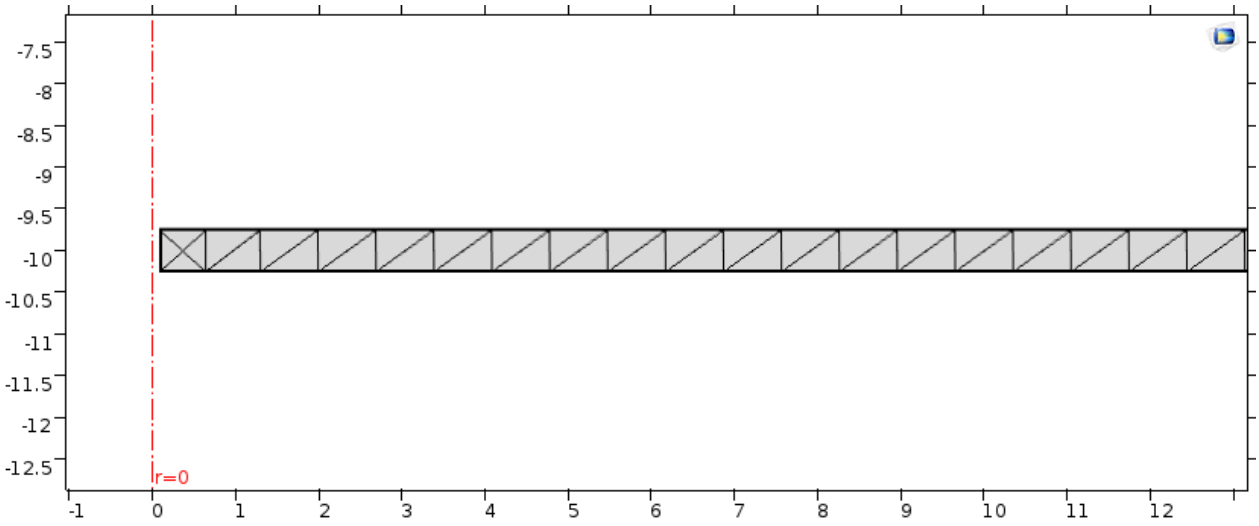

Figure 4.2. Partial view of the domain during the first stage (application of gravitational load) and the respective mesh (horizontal axis: length, vertical axis: depth)

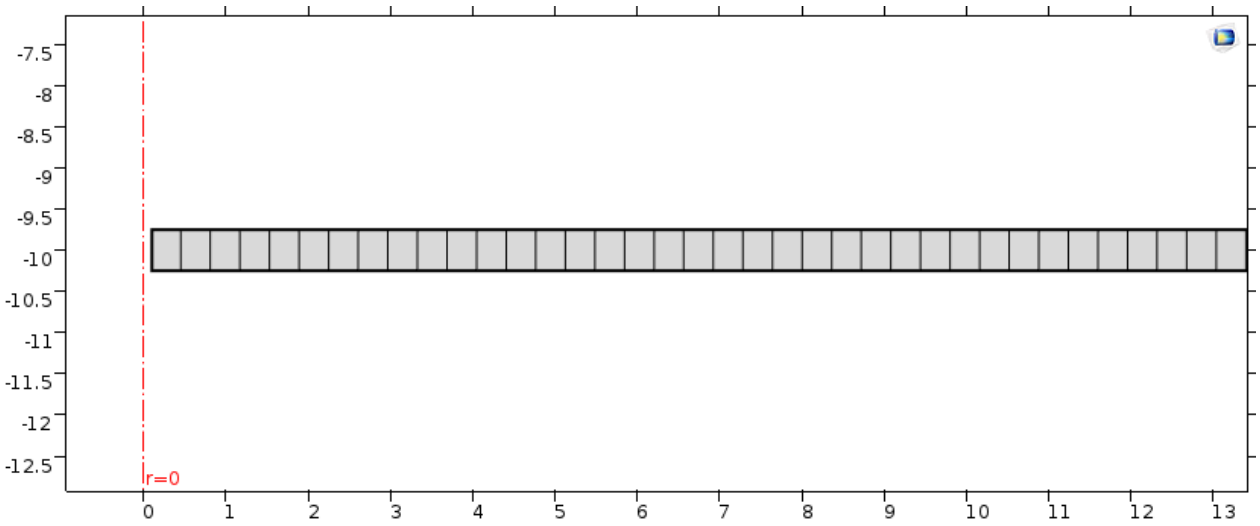

Figure 4.3. Partial view of the domain during the second stage (cavity expansion) and the respective mesh (horizontal axis: length, vertical axis: depth)

For the second stage, the domain has its final form and the sinusoidal load at the cavity is activated. The effective stresses calculated in the first study are set as initial stresses for this stage, while the initial strains are set equal to zero. The mechanical boundary conditions include rollers along the upper and lower boundary. Additionally, at the cavity both the radial effective stress and the cavity expansion load are implemented. Finally, the Perfectly Matched Layer, which was used in the frequency domain analysis, is replaced by a symmetrical condition along the boundary opposing the cavity because the PML exhibits limitations, as already described in Section 4.1. The hydraulic boundary conditions include no flow at the cavity and hydrostatic boundary conditions along the rest of the boundaries. The mesh in this case is selected mapped, in accordance with the frequency-domain analysis (Figure 4.3).

The boundary conditions for each stage are summarised in the following table:

Table 4.1. Boundary condition for each stage of the time-dependent analysis

	Stage 1: Stationary		Stage 2: Time dependent	
Boundary	**Mechanical**	**Hydraulic**	**Mechanical**	**Hydraulic**
Left (cavity)	Rollers	Hydrostatic	Boundary load + Effective stress	No flow
Right	Rollers	Hydrostatic	Symmetry	Hydrostatic
Upper	Load (overburden)	Hydrostatic	Rollers	Hydrostatic
Lower	Rollers	Hydrostatic	Rollers	Hydrostatic

The initial stresses are also taken into account at this stage in order to calculate the shear modulus (G). The latter is calculated according to Hardin (1978):

$$G = G_{max} = \frac{A * OCR^{k}}{F(e)} p_{atm} \left(\frac{p'}{p_{atm}} \right)^{\bar{n}} \quad 4.3$$

where

A is a dimensionless parameter (usually equal to A=625),

OCR is the overconsolidation ratio (OCR=1 for sand),

k is an exponent or OCR as a function of plasticity index (here k=0 for PI=0%)

$F(e)=0.3+0.7e^2$ is a function of the void ratio of the poroelastic material,

e=n/(1-n) is the void ratio

p_{atm}=1atm=101.325kPa is the atmospheric pressure

$p'=(\sigma_z'+2\sigma_r')/3=(\sigma_z'+2K_0\sigma_z')/3=(2K_0+1)\sigma_z'/3$ is the mean effective stress,

$K_0=v/(1-v)$ is the coefficient of earth pressure and

$\bar{n}$=0.5 is an exponential coefficient

The specific value for the shear modulus is obviously dependent on depth, which is introduced via the mean effective pressure. In a microscopic view, the confining pressure is larger at greater depths. The opposite happens when the void ratio increases. The pores are larger in this case and therefore the contact surface of the solid particles becomes smaller. In equation (4.3) the shear modulus is also mentioned as G_{max} because it will be used as the initial shear modulus for the nonlinear model. The latter will be in detail explained in the following chapters. It also becomes obvious from the expression for the shear modulus that, the deeper the probe is inserted, the stiffer the poroelastic response. It is also essential to be noted that the bulk modulus (K) is calculated as a function of the shear modulus (G) assuming the Poisson ratio of the frame to be constant with depth. Hence:

$$K = \frac{2G(1+\nu)}{3(1-2\nu)} \tag{4.4}$$

4.3 The nonlinear elastic hyperbolic model

4.3.1 Basic theory principles

So far, the definition of stresses and strains as well as the constitutive equations are based on the small (infinitesimal) deformation assumption. More specifically, the deformation of a representative elementary volume is small compared to the volume itself, such that only the first order variation terms of the deformation are retained in defining the stresses and strains. In other words, stresses and strains are considered at fixed locations of a fixed spatial frame as the first derivatives of the local deformation. When deformations become large, one should consider higher order derivatives and also the fact that the material no longer occupies the original space, so that a material frame (Lagrangian frame) instead of the previous spatial frame is necessary. These considerations lead to a finite or large deformation theory, with geometric nonlinearity. (Cheng, 2016)

However, many experimental results have shown that, even within the small deformation range, the volumetric response of porous rocks to the change of total pressure and pore pressure is nonlinear (Cheng, 2016). The extent of this statement to other poroelastic materials, such as the porous sandy material considered in the present research, will be taken into consideration from now on. Therefore, the linear constitutive relations presented so far are merely approximations. In fact, it is almost impossible to apply any effective stress to a solid matrix of a granular soil without any slippage or rearrangement.

Subsequently, the nonlinear analysis will focus in the small-strain range, where the material does not exhibit geometric nonlinearity. The stresses are linked to the strains according through the Cauchy tensor instead of the second Piola-Kirchhoff tensor. Moreover, as opposed to hyperelastic materials, which exhibit nonlinearities at moderate to large strains, the sand is assumed to obey a nonlinear law even at

infinitesimal strains. This type of material is named 'nonlinear elastic material'. Additionally, the nonlinear elastic materials include neither strain rate nor stress rate in the constitutive equations. This feature allows for the addition of linear viscoelasticity in the model.

The nonlinear soil behaviour is often expressed through stress or strain dependency of their stiffness. In particular, one of the stiffness parameters, decreases with amplification of strain. In the present analysis, the decreasing stiffness parameter is the secant shear modulus (G_s). The volumetric shtiffness parameter, namely the bulk modulus (K) is calculated as a function of the secant shear modulus, assuming that the Poisson ratio is kept constant. The relationship between the shear modulus and the strain amplitude is typically characterised by a normalised modulus reduction curve (Darendeli, 2001). For the nonlinear analysis of the present work the hyperbolic model is selected. The maximum secant shear modulus for low strains is calculated by equation (4.3). This value is valid only for a very small range of shear strains. Outside this purely linear elastic region, as the shear stress increases towards failure, the stiffness is a function of the shear stress level (Fahey and Carter, 1992). Hardin and Drnevich (1972a and 1972b) stated that the prefailure behaviour of sand can be represented by a hyperbolic model reasonably.

For shear strain less than γ=0.001% the soil exhibits practically pure linear elastic behaviour. The shear modulus is constant and equal to G_{max} while energy dissipates only because of friction between the particles and/or viscosity (Darendeli, 2001). Because the latter is not taken into account by the present model, the material exhibits linear behaviour for that range of strain. The shear strain at which the shear modulus decreases to a value of $G=0.98G_{max}$ is called the elastic threshold strain. For strains larger than this value the material behaves still elastic but not linear. The strain amplitude at which the strains become irreversible is called threshold cyclic strain and for strains larger than this level the material exhibits volume change (Darendeli, 2001). For the present research, the material is assumed not to reach the threshold cyclic strain.

The stiffness reduction curves by Darendeli (2001) are based on the hyperbolic model developed by Hardin and Drnevich (1972a and 1972b) and will be adopted for the present nonlinear analysis. The modifications by Darendeli (2001) are utilised to represent a normalised modulus reduction curve as:

$$\frac{G}{G_{max}} = \frac{1}{1 + \left(\frac{\gamma}{\gamma_{ref}}\right)^{\beta}} \tag{4.5}$$

where

G/G_{max} is the normalised shear modulus

γ is the shear strain

γ_{ref} is the reference shear strain

β is a curvature coefficient

The simplicity of this constitutive model lies in the determination of only two parameters: the reference shear strain and the curvature coefficient. The latter are estimated following the proposed method by Darendeli (2001) as follows:

$$\gamma_{ref} = (\varphi_1 + \varphi_2 * PI * OCR^{\varphi_3}) p'^{\varphi_4} \tag{4.6}$$

and

$$\beta = \varphi_5 \tag{4.7}$$

where ϕ_1 through ϕ_5 are parameters which relate the reduction curve to the soil type and loading conditions and have been defined statistically after tests on samples of various materials and locations by Darendeli (2001) as follows:

ϕ_1=0.0352

ϕ_2=0.0010

ϕ_3=0.3246

ϕ_4=0.3483

ϕ_5=0.9190

For values of the plasticity index (PI=0), the overconsolidation ratio (OCR=1) and the mean effective stress identical to the calculation for G_{max} (Section 4.2) the above equations result in:

γ_{ref}=0.03%

β=0.919

These values result in the following strain reduction curve (Figure 4.4):

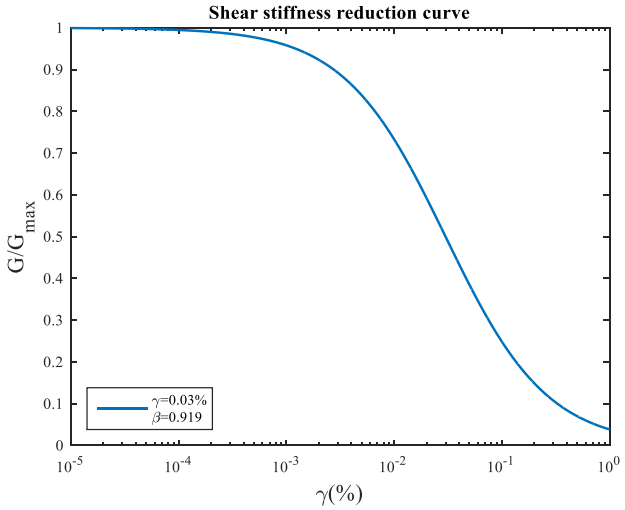

Figure 4.4. Shear modulus reduction curve (γ_{ref}=0.03%)

It becomes obvious that the shear modulus degrades even for very low strains. This is a result of the curvature exponential coefficient (β). This coefficient is a function of the soil plasticity index which cannot be defined for sands. Hence, the value of the coefficient is relatively low compared to soils with a higher plasticity index, such as clays. For the latter, one would observe a more extensive flattening area before the shear modulus reduces. The physical consequence is that the nonlinear effects are more dominant for sands than for more plastic soils.

4.3.2 Single-element testing

The FEM platform COMSOL Multiphysics can model the poroelastic behaviour accurately, as it has been proven so far. However, nonlinear behaviour cannot be directly implemented by the 'Poroelastic' interface. Instead, the 'Solid Mechanics' interface should be used and coupled with the 'Darcy Law' interface in order to incorporate nonlinear behaviour and maintain the poroelastic character of the response.

The two aforementioned interfaces cannot be automatically coupled. The user has to define and link the terms of the governing equation which link the two processes. These terms are mentioned later in this section. As a result, the manual coupling between the two interfaces has to be tested. To accomplish this, a single-element soil specimen is subjected to pure shear. This procedure is a representation of the direct simple shear (DSS) laboratory test. Initially, the specimen is assumed to be dry and only the 'Solid Mechanics' interface is used. The aforementioned nonlinear law governs the behaviour. The first stage includes application of the overburden load. Similarly as before, the element is assumed to be situated at 10m depth. The effective stresses calculated at the first stage are the initial values for the next stage whereas the strains are set back to zero. During the second stage, a horizontal (radial) displacement is applied to the upper left node in steps. More specifically, the horizontal displacement of 5mm is divided into 50 equally large steps. Figure 4.5 presents the whole procedure schematically. The multi-coloured figures represent the deformed material whereas the grey figures represent states of zero strains. However, the stresses are not necessarily zero.

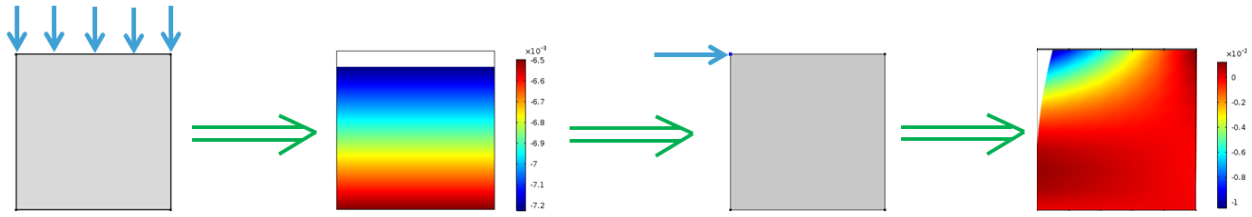

Figure 4.5. Schematic representation of the single-element test (the colours represent vertical strains in the second picture and radial strains in the last picture)

At each step, the shear stress (τ_{rz}) and shear strain (ε_{rz}) are measured at the Gauss point of the element. Taking into account that the shear strain (γ) is twice as large as (ε_{rz}) and with the aid of the τ-γ curve as extracted from the numerical experiment, the secant shear modulus can be plotted versus the shear strain, so as to be compared with the degrading shear modulus according to the hyperbolic law (Figure 4.4). The secant shear modulus is calculated to be:

$$G_s = \frac{G_{max}}{1 + \left(\frac{2\sqrt{\varepsilon_{el}^{II} + eps}}{\gamma_{ref}} \right)^{\beta}} \tag{4.8}$$

where

G_s is the secant shear modulus

ε^{II}_{el} is the second invariant of the elastic deviatoric strain tensor and

eps is a very small value to avoid division by zero

The second invariant of the elastic deviatoric strain is defined as

$$\varepsilon_{el}^{II} = \frac{1}{2}\left[\left(\varepsilon_{11}^{el} - \varepsilon\right)^2 + 2\varepsilon_{12}^{el^2} + 2\varepsilon_{13}^{el^2} + \left(\varepsilon_{22}^{el} - \varepsilon\right)^2 + 2\varepsilon_{23}^{el^2} + \left(\varepsilon_{33}^{el} - \varepsilon\right)^2 \right] \tag{4.9}$$

where

ε^{el}_{ij} are the components of the elastic strain tensor

It has to be noted that the numerator of the fraction within the brackets of Equation 4.8 is different than the shear strain (γ_{rz}) determined at the Gauss point. Hence, both definitions of the secant shear modulus will be verified. The verification of the implementation of the hyperbolic law by COMSOL Multiphysics is presented in Figure 4.6.

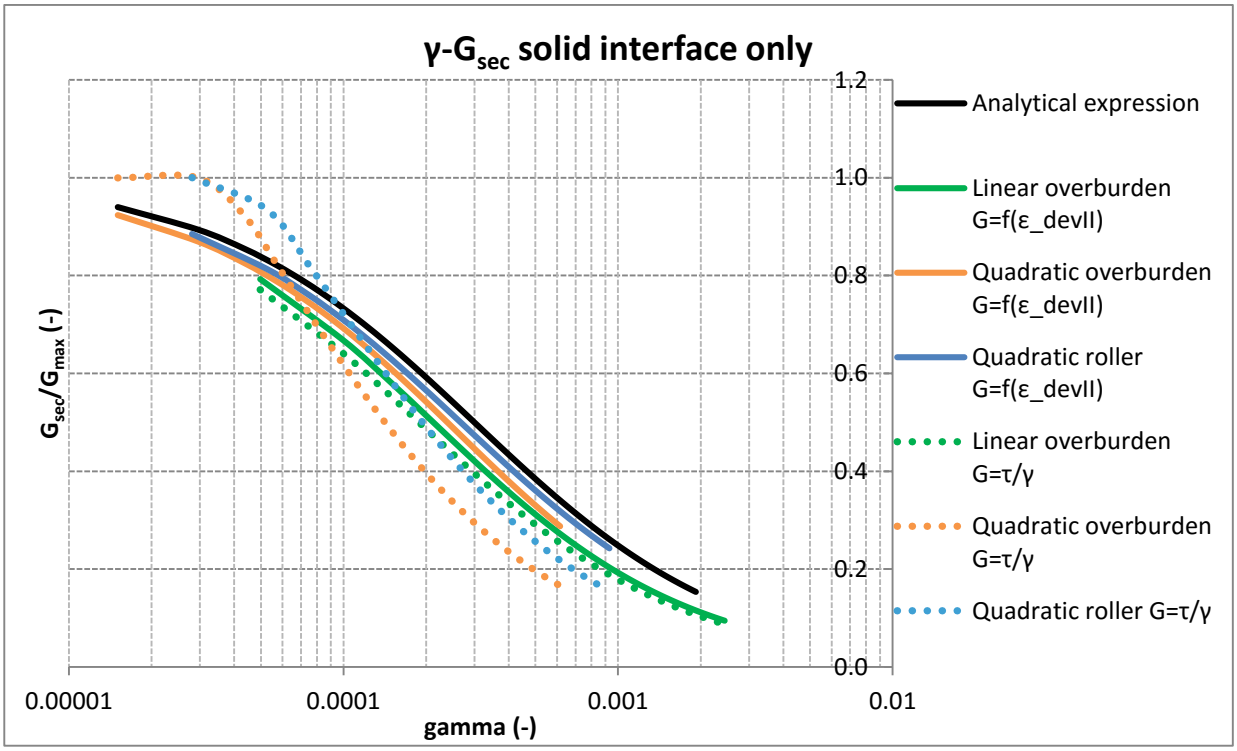

Figure 4.6. Comparison of the secant shear stiffness reduction curve with the analytical expression for both strain invariants and various element discretisation (dry material)

It is observed that the secant shear modulus used by default by COMSOL Multiphysics, which is a function of the second invariant of the deviatoric elastic strain tensor, can represent the nonlinear behaviour of the material better than the back-calculated from the stress-strain response secant shear modulus. In other words, this representation of the secant shear modulus which is obtained by COMSOL Multiphysics as a function of the second invariant of the elastic deviatoric strain tensor is the best representation of the analytical expression of the Hyperbolic law. The τ-γ representations for quadratic elements result in stiffer behaviour for small strains and softer behaviour for large strains in comparison with the analytical expression. Generally, the quadratic elements (blue and orange lines) perform better than the linear elements, meaning that the numerical error reduces and the resulting shear stiffness reduction curve lies closer to the expected one. Finally, two different boundary conditions of the upper boundary of the element were compared: Maintaining the boundary load of the overburden through the whole analysis and replacing it by rollers after the end of the first stage of the analysis. It can be concluded that replacing the overburden load with rollers provides with a better representation of the expected behaviour. Therefore, during the analysis of the pressuremeter test, the overburden boundary load will be replaced with rollers for the time-dependent stage.

The second test on the single element is to couple the already used 'Solid Mechanics' interface with the 'Poroelastic' interface. In order to accomplish this, the independent displacement variables are specified in both interfaces with the same notation. After the load of the overburden is applied to the specimen using the 'Poroelastic' interface only (linear poroelastic material), the initial shear modulus is calculated

by the 'Solid mechanics' interface. Within the latter, the secant shear stiffness value is computed for each time step. The 'Poroelastic' interface, finally, conducts a linear poroelastic analysis using the strain dependent stiffness parameters calculated by the 'Solid Mechanics' interface.

Although this coupling is efficient when the material is dry, the opposite occurs when fluid flow occurs. In fact, the coupled interfaces cannot link the effective stress distribution between the two analysis stages. This limitation results in the respective curves of Figure 4.7. It becomes clear that the stiffness is overestimated by this coupling scheme and therefore this coupling is considered as inaccurate for the nonlinear analysis.

As a result, the 'Solid Mechanics' interface is coupled with the 'Darcy Law' interface. Each interface contains one of the governing equations: Equation (2.120) is the governing equation for the 'Solid Mechanics' whilst Equation (2.121) is the governing equation for 'Darcy Law' without the storativity and the volumetric strain ratio term. As a result, the coupling of the two interfaces is implemented based on the following:

- An external force node in terms of pore pressure is introduced to the solid material and is set equal to the total pressure calculated by the 'Darcy Law'. Therefore the 'Solid Mechanics' interface works only with effective stresses.
- A 'Storage Model' node is introduced to the 'Darcy Law' interface where the storativity is defined as a function of the bulk modulus and the Biot coefficient.
- The missing term ($\rho_f \alpha \partial\varepsilon/\partial t$) is added as a 'Mass Source' term in the 'Darcy Law' interface.

In Figure 4.7 it becomes clear that the stiffness reduction curves when the 'Solid Mechanics' interface is coupled with the 'Darcy Law' (green lines) are identical to the dry material (Figure 4.6), unlike the coupled 'Solid Mechanics'-'Poroelastic' interfaces (blue lines). Consequently, the coupled interface scheme is now fully determined for the time-domain analysis of the pressuremeter test in nonlinear poroelastic material.

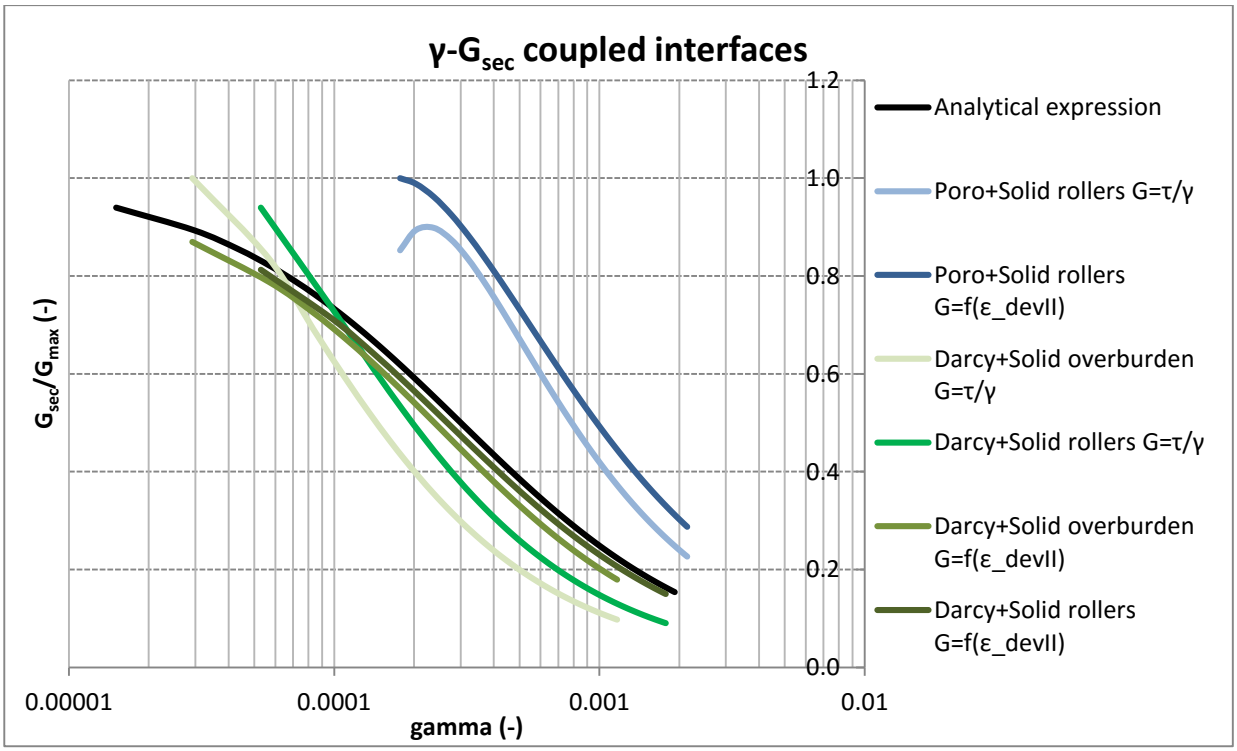

Figure 4.7. Comparison of the secant shear stiffness reduction of various coupled interfaces and boundary conditions with the analytical expression

Finally it has to be noted that the specific test exhibits a limitation. The deformed element should theoretically end up with straight vertical boundaries. This is because during the direct simple shear test the vertical boundaries are constrained by the walls of the test device. However, at the end of the test the deformed element has the form represented by Figure 4.8. Generally, in order to overcome this limitation, one has to introduce more nodal displacements along the left vertical boundary. However, when COMSOL Multiphysics is used, this is not possible because the element is automatically remeshed according to the nodes added on the boundary. Judging from the strain-stiffness behaviour though, this limitation is of minor significance; the simulation performs sufficiently well.

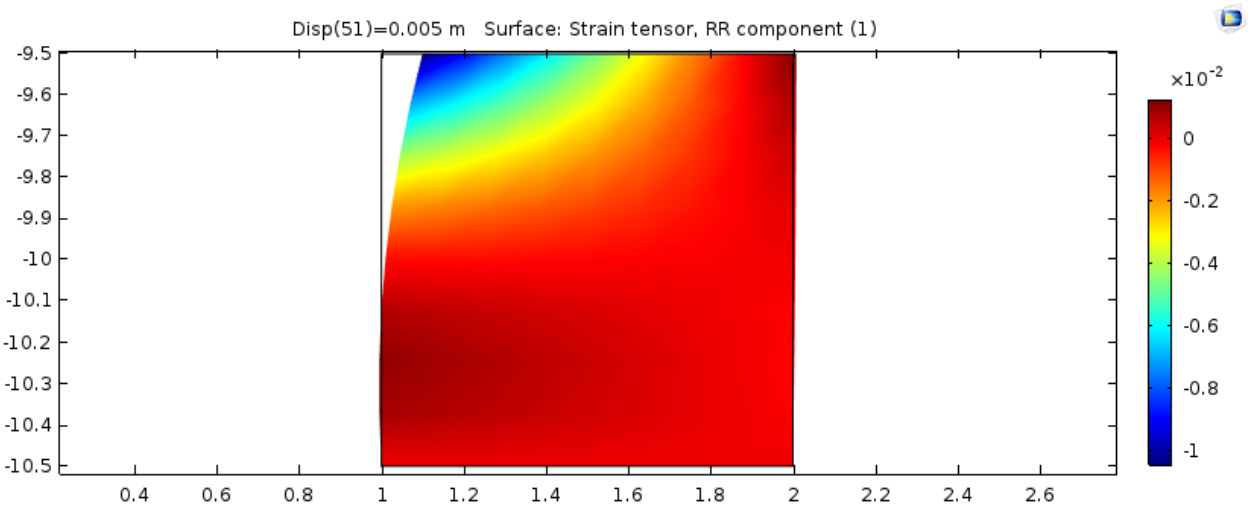

Figure 4.8. Deformed element at the end of the second stage of the test

5

Results and discussion of the numerical approximation

The models described in Chapter 4 are implemented in the software package COMSOL Multiphysics and the results are presented in this chapter. First, the frequency domain analysis of the linear poroelastic model is compared to the analytical solution by assuming both consideration and omission of the relative acceleration of the fluid and the solid phase. The results exhibit an accurate representation of the response for a selected frequency range up to 100Hz.

Second, the linear poroelastic analysis is conducted in the time domain. Initially, the soil stiffness is assumed identical to the stiffness taken into consideration for the frequency-domain analysis in order to ensure that the time-domain solver functions in an accurate way. Afterwards, the soil stiffness is determined as the function of the mean effective pressure, as defined by Equation 4.3. The same comparison between the time-domain and the frequency-domain analysis using the aforementioned calculated stiffness values is accomplished.

Finally, the nonlinear analysis is presented. The influence of poroelasticity is pointed out by comparing the poroelastic response with the response of a dry material. In other words, the response of the coupled 'Solid mechanics' with 'Darcy law' interfaces is compared to the 'Solid mechanics' interface itself. Furthermore, the influence of permeability and reference shear strain are also quantified.

5.1 Frequency domain linear poroelastic analysis

The frequency domain study is conducted for the frequency range of f=[0.1,100]Hz with a step of 0.1Hz. A domain point probe is set at z=0 on the cavity boundary in order to measure the displacement response of the cavity. The analysis has been conducted both including the relative acceleration terms and neglecting them, according to equations (2.111) and (2.112). The amplitude spectrum is presented in Figure 5.1 for both cases. The analytical solution is plotted as well, in order to present the convergence of the numerical approximations. It can be observed that the numerical result is in perfect agreement with the analytical solution derived in Section 2.2.1 when the relative acceleration terms are taken into consideration. When the latter are neglected, the response exhibits some shift, which is also negligible. As a result, the assumption of negligible relative acceleration terms is valid in such frequencies. The following analyses in time domain will make use of this assumption.

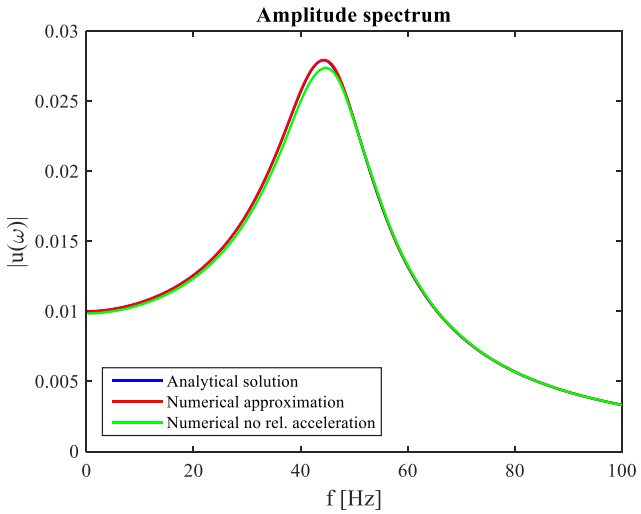

Figure 5.1. Amplitude spectrum of the displacement of the cavity computed analytically and numerically

5.2 Time-domain linear poroelastic analysis

5.2.1 Time-domain analysis without gravitational effect

The time-dependent analysis is conducted for various discrete frequency values and the respective response is presented in the following figures. It has to be noted that the following graphs refer to the linear poroelastic analysis without stress initialisation. In other words, the gravitational effect, meaning the depth at which the probe is inserted in the material, is not taken into account. Hence, the shear modulus is not calculated using equation (4.3) but as a function of the arbitrarily selected Young's modulus and Poisson ratio (see also Table 3.1). Additionally, the first stage described previously is skipped. This facilitates the comparison of the amplitude of time-domain analyses with the amplitude predicted by the frequency-domain analysis described in Section 4.1. First, in Figure 5.2 the response is presented for a low-frequency excitation (f=0.5Hz). It can be seen that the amplitude of the response is equal to the predicted value by the frequency-domain analysis (Figure 5.1).

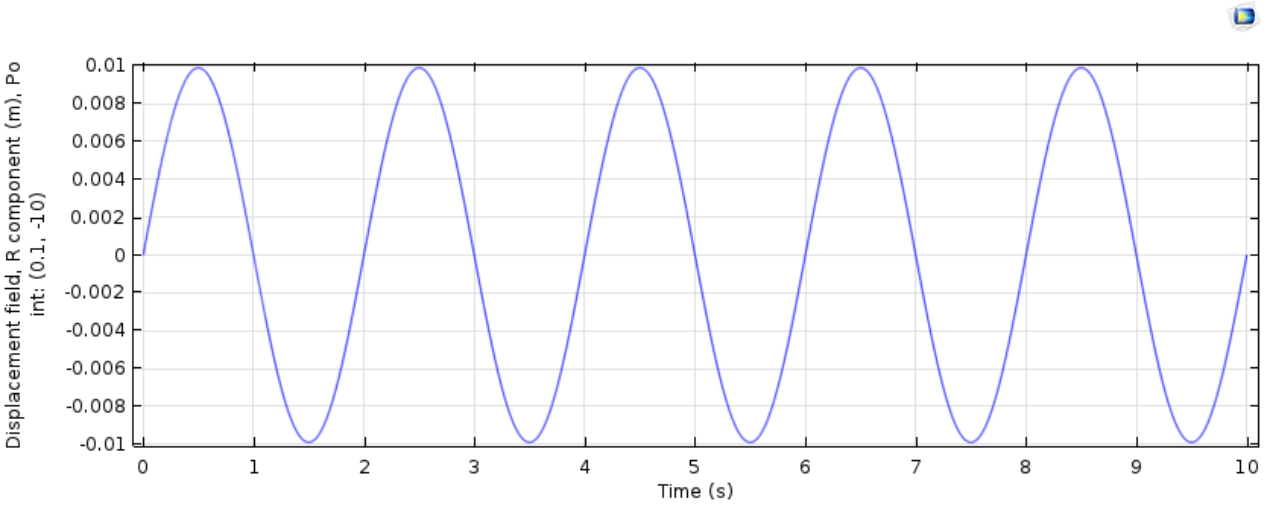

Figure 5.2. Time-domain linear elastic response for excitation of frequency f=0.5Hz

For larger values of frequency (f=10Hz) the response is presented in Figure 5.3. The first cycles do not have the same amplitude, which shows that the steady-state response is not reached before

approximately t≈1s. After that point the amplitude of the response reaches the value predicted by the frequency domain analysis (Figure 5.1).

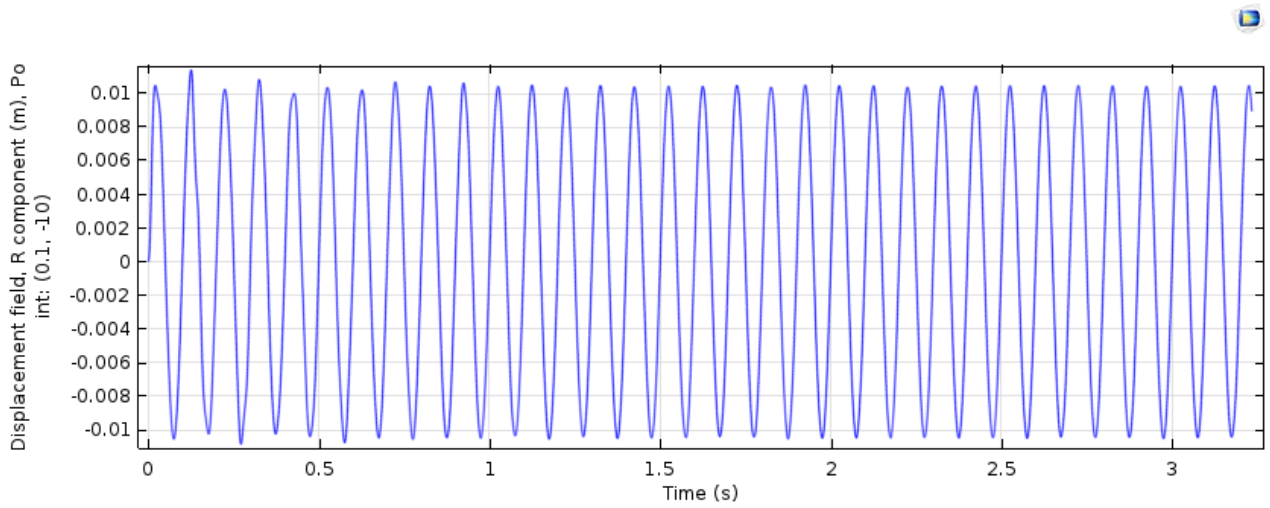

Figure 5.3. Time-domain linear elastic response for excitation of f=10Hz

In a similar way, the linear elastic response can be predicted for every value of frequency. The system reaches the steady state after some cycles, the amount of which varies with frequency. When this happens, the system vibrates only with the frequency introduced by the cavity load. Natural-frequency oscillations have been damped out. In Figure 5.4 the oscillation caused by f=40Hz sinusoidal load is presented. The steady-state response is almost reached after two cycles (much earlier than the response of 10Hz) and the amplitude of the vibration is equal to the one predicted by the frequency-domain analysis.

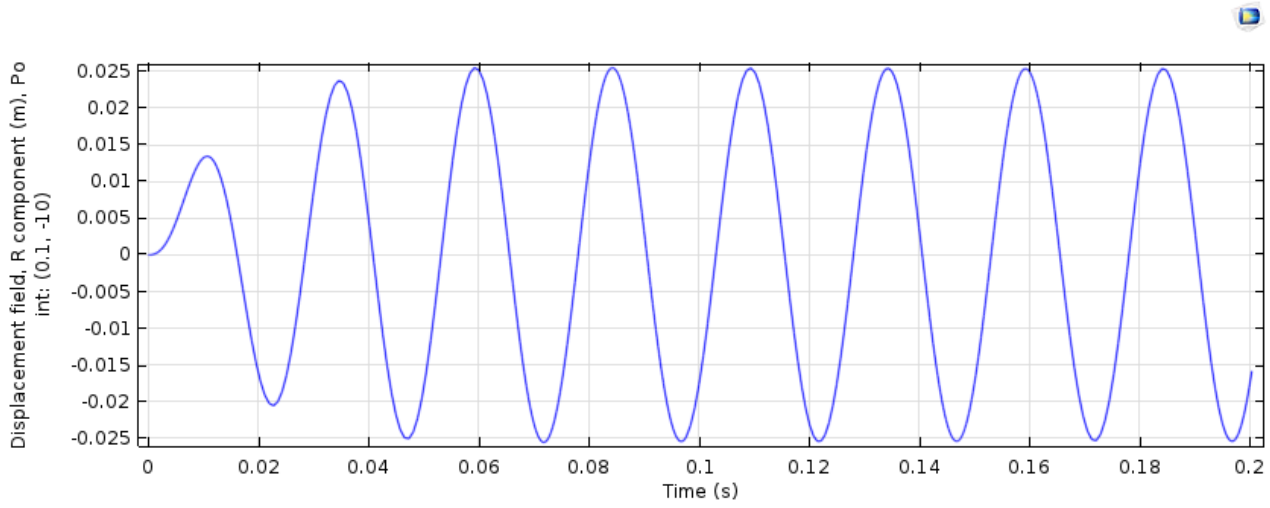

Figure 5.4. Time-domain linear elastic response for excitation of f=40Hz

Consequently, the time-domain analysis provides with results that are in accordance with the frequency-domain elastic analysis. The efficiency of this model allows enhancement with the initialisation of the stress caused by gravity, so that the nonlinear analysis can be conducted.

5.2.2 Time-domain analysis including gravity loads and stress initialisation

What follows is a linear elastic analysis in the time domain following all three stages mentioned previously, thus taking into account insertion of the probe in the poroelastic material at 10m depth and

initialisation of the stresses and strains. For this analysis the stiffness of the material is considerably larger than the previous ones, since it is a function of the mean effective stress, according to Equation 4.3. The deeper the probe is inserted, the stiffer the material behaves. When the probe is inserted in 10m depth, Equation 4.3 gives shear stiffness of G_{max}=123.7MPa. The analytical solution in the frequency domain for this value of shear modulus results in the following amplitude spectrum (Figure 5.5):

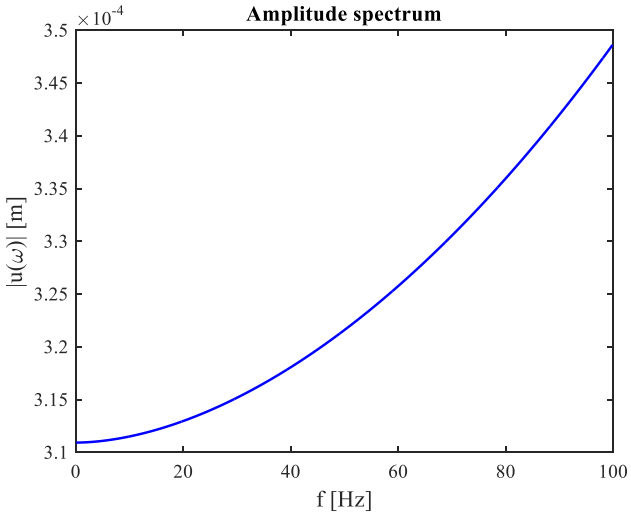

Figure 5.5. Amplitude spectrum of the linear elastic response for a probe inserted at 10m depth

The next figure illustrates the time domain response for 0.5Hz frequency. The amplitude of the response matched the prediction using the frequency domain analysis. Further analyses at more frequencies were run so that the accuracy of the time-dependent solver after stress initialisation can be checked. However, only one representative figure is presented.

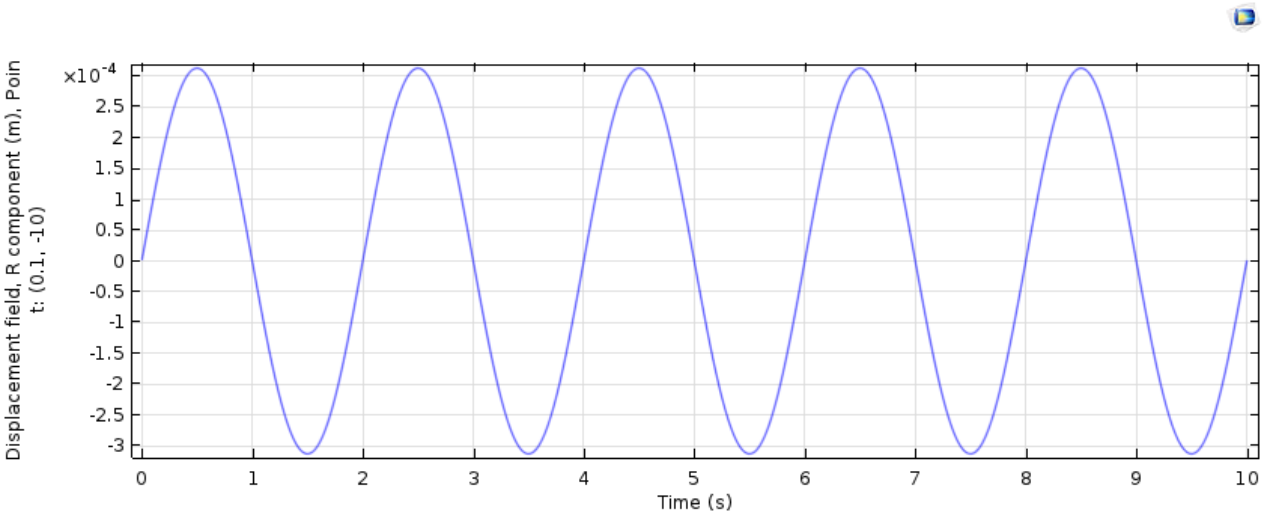

Figure 5.6. Time-domain response to excitation of 0.5Hz assuming linear poroelasticity for a probe inserted at 10m depth

It has to be noted that the amplitude of the response is mesh density dependent. The mesh has to be fine enough to reach the predicted amplitude by the frequency domain analysis. If it is coarse, the amplitude of the radial displacement is underestimated. If it is finer than some density, it leads to instabilities.

Regarding the pore pressure, in sharp contrast to the low stiffness material which was presented in Section 3.2.5, when the test is assumed to be conducted at 10m depth, it is observed much lower. The pore pressure at the cavity over frequency is illustrated in Figure 5.7.

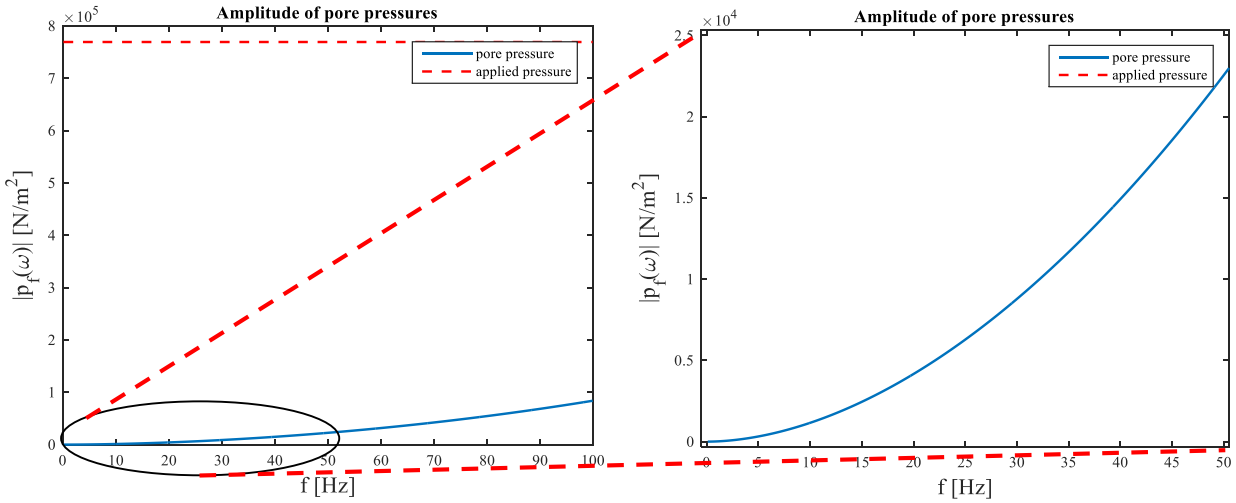

Figure 5.7. Pore pressure over frequency at the cavity of a probe inserted at 10m depth and zoom in the first 50Hz

It can be observed that for 50Hz of excitation frequency the maximum pore pressure observed is approximately 22kPa, according to the right panel of Figure 5.7. This panel will be the reference for the comparison with the pore pressure resulting from the nonlinear response, which follows.

5.3 Nonlinear poroelastic analysis

The time-domain analyses presented in Section 4.2 incorporate now the nonlinear law and the coupling between the two interfaces described in Section 4.3. Hence, the solid phase of the material behaves nonlinearly while the load imposed by the cavity is the same as the one applied so far. Because the stiffness of the material becomes less as the deformation increases and vice versa, the maximum displacement of the response is expected to be clearly larger than the amplitude resulting from the linear poroelastic analysis, as shown in Figure 5.5. Such a behaviour is presented in Figure 5.8.

The following conclusions can be drawn: The maximum displacement is clearly larger than the predicted amplitude according to linear poroelasticity. Additionally, the response is not harmonic, as it was according to linear elastic analysis. The strain-dependent stiffness of the soil gives rise to the generation of a higher harmonic, whose frequency seems to be three times as large as the excitation frequency. Such nonlinear oscillations were described by Nayfeh (1993) and for a single-degree-of-freedom system are represented in the general case by the following equation:

$$m\ddot{u} + c\dot{u} + k_1 u + k_3 u^3 = f(t) \qquad 5.1$$

where k_3u^3 is the extra term arising for nonlinearities. The above equation is known as the Duffing equation and can possibly represent the nonlinear ground response to the dynamic pressuremeter test. However, the solution of the Duffing equation and the correlation with the present study lies beyond the scope of this project.

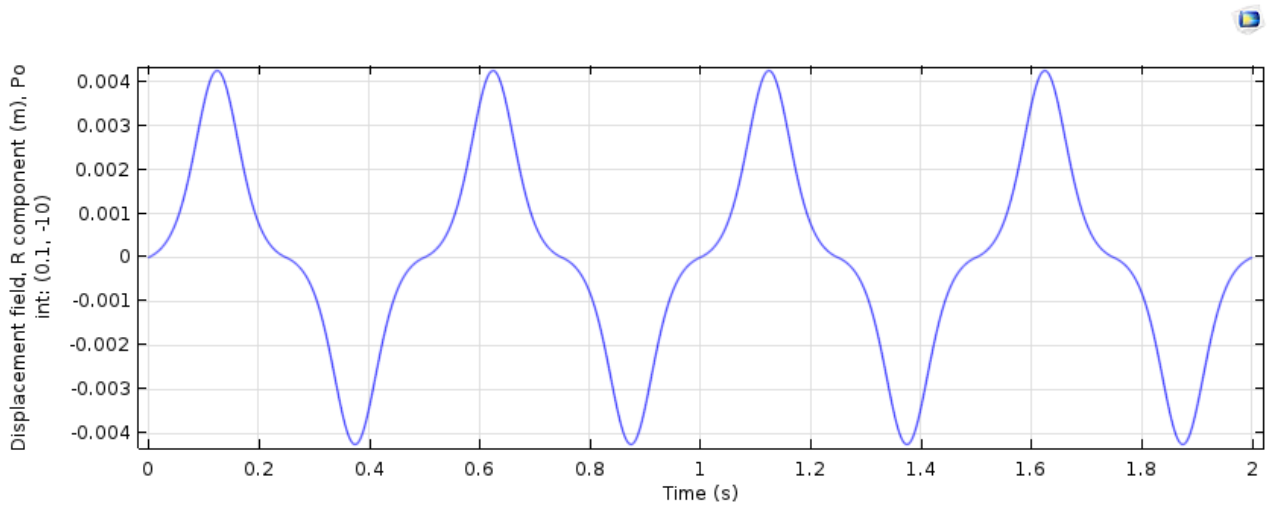

Figure 5.8. Nonlinear response to f=2Hz excitation at 10m depth (γ_{ref}=0.3% β=0.919)

The presence of higher harmonics is a natural consequence of nonlinearity. It has been observed in many applications. For instance, Karunakaran and Spidsøe (1997) measured such a behaviour while studying the nonlinear dynamic response of jack-up platforms. However, their simulations did not predict such a velocity time series, as can be seen in Figure 5.9. Hence, they assumed that there was a consequence of a possible error of the measuring device. The question is, however, whether this assumption is correct. The nonlinear behaviour described by the Duffing equation results in an extra third-order sinusoidal oscillation.

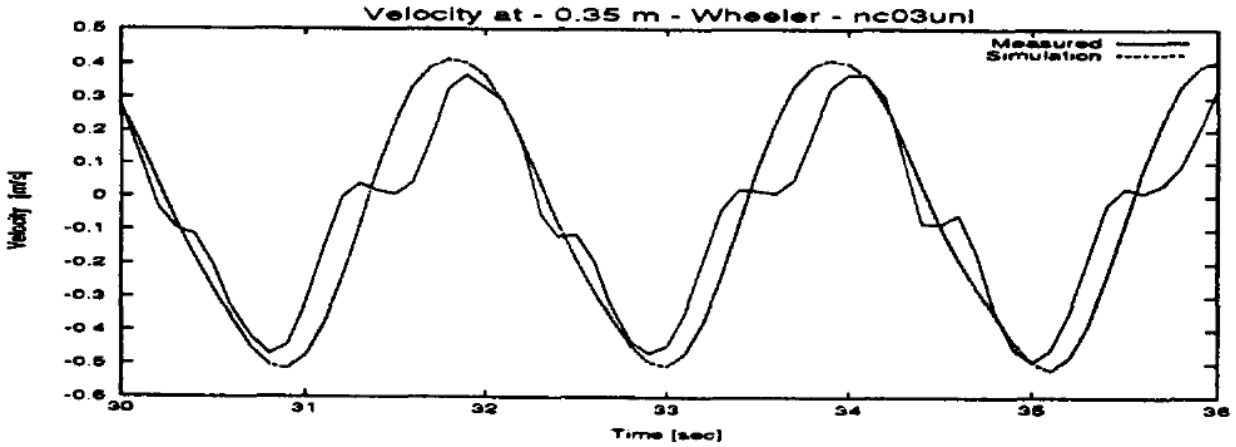

Figure 5.9. Comparison of measured and simulated velocities – Regular wave (Karunakaran and Spidsøe, 1997)

The present analysis focuses on the influence of the nonlinear parameters, and more specifically the influence of the reference shear strain (γ_{ref}). Additionally, the poroelastic nonlinear response is compared to the linear poroelastic response in order to quantify the nonlinear effect. Furthermore, the behaviour of highly permeable materials (k=10^{-3}m/s) is presented. Finally, the load upper limit for the linear poroelastic response is calculated.

5.3.1 Influence of the nonlinear parameters (γ_{ref} and β)

Darendeli (2001) based the development of the modulus reduction curves on semi-empirical parameters which were extracted from experimental data. The samples were analysed according to soil type and

geographical location. Especially for 'clean sands' the following combinations of nonlinear parameters are specified (

Table 5.1).

Table 5.1. Nonlinear parameters for 'clean sands' (Darendeli, 2001)

Nonlinear Parameter	Prior to the analysis	North California	South California	South Carolina	Overall
Reference shear strain (γ_{ref})	$2.7 \cdot 10^{-4}$	$3.7 \cdot 10^{-4}$	$1.9 \cdot 10^{-4}$	$8.4 \cdot 10^{-4}$	$\mathbf{3 \cdot 10^{-4}}$
Exponential coefficient (β)	0.85	0.941	0.834	0.838	**0.919**

The overall values of the nonlinear parameters by Darendeli (2001) were used in Section 4.3.1 to determine the stiffness reduction curve, which was presented in Figure 4.4. In this section, the response of the poroelastic medium will be investigated according to the overall nonlinear parameters by Darendeli (2001), the South Carolina sand by Darendeli (2001) and two more cases, which are summarised in Table 5.2. The respective shear stiffness reduction curves are shown in Figure 5.10.

Table 5.2. Nonlinear parameters used for the sensitivity analysis

Reference shear strain (γ_{ref})	0.003	0.00084	0.0006	0.0003
Exponential coefficient (β)	0.919	0.838	0.838	0.919

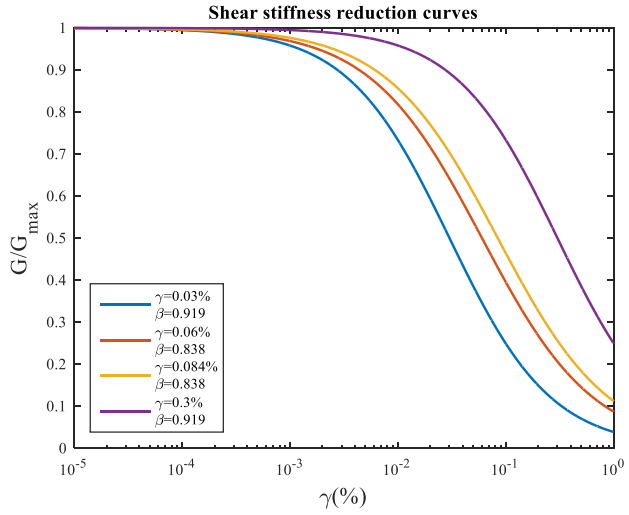

Figure 5.10. Stiffness reduction curves for the sets of nonlinear parameters of Table 5.2

Starting from the material with the largest reference shear strain and for each set of nonlinear parameters, the maximum displacement and pore pressure are presented. The analyses have been accomplished with the aid of the software package COMSOL Multiphysics. The model setup follows the process described in Section 4.3. The cavity pressure is 770kPa. In order to determine the maximum displacement for various frequencies, time-domain analyses have been run for discrete frequencies and the resulting values have been interpolated. The frequency range is 0-50Hz. The nonlinear poroelastic analysis is compared for each case to the nonlinear drained elastic analysis. For the latter, an equivalent

single-phase material is assumed whose density is equal to the average density of the poroelastic material. It has to be noted that for all cases that are presented in the following graphs over frequency the response follows the pattern illustrated by Figure 5.8.

In Figure 5.11 the maximum radial displacement and the pore pressure of the steady-state response are presented over frequency for the material which is supposed to exhibit the least nonlinear behaviour (γ_{ref}=0.3% and β=0.919). Compared to the linear poroelastic analysis (Figure 5.5) the maximum radial displacement is about one order of magnitude larger. In addition, an amplification peak is detected for frequencies around 40Hz, in accordance to the analytical solution (Figure 3.18). Compared to the nonlinear elastic solution, the displacements do not seem to deviate much, which can be explained in combination with the small values of pore pressures calculated. Additionally, the relative-to-the-hydrostatic pore pressure measured at the cavity is presented. As expected, for very low frequency there is no pore pressure variation. The pore pressures gradually build up as the frequency increases. Because the nonlinearity is not strong in this case, the maximum pore pressure resulting for 50Hz of frequency excitation is of the same order of magnitude as the one resulting from the linear analysis (Figure 5.7).

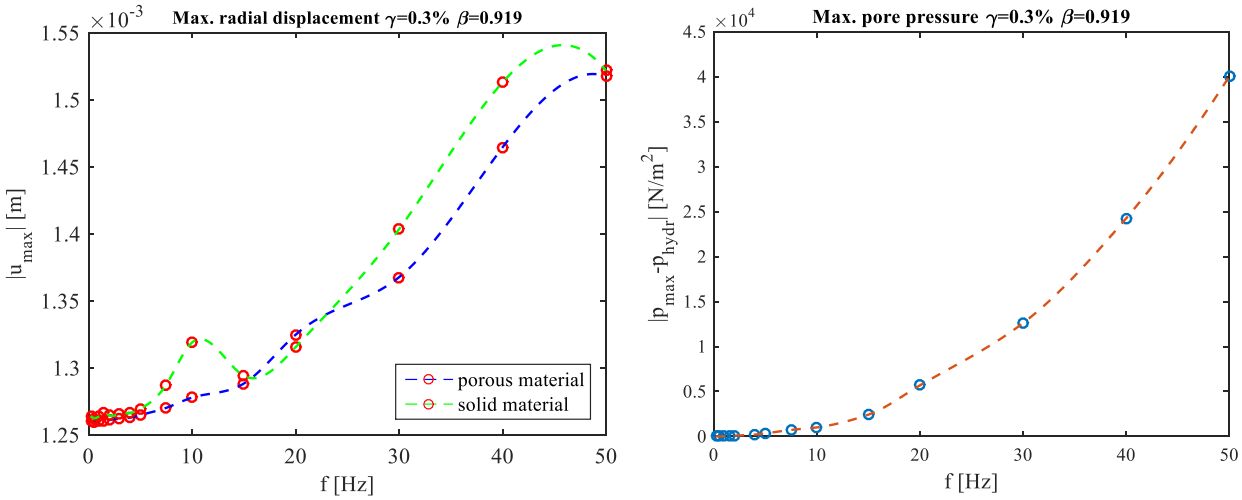

Figure 5.11. Maximum radial displacement over frequency for nonlinear poroelastic and elastic analysis (γ=0.3% β=0.919) and the respective pore pressure

Secondly, the nonlinear parameters of the South Carolina sand are used to conduct a similar analysis. This set of parameters exhibited the least nonlinear behaviour among the sandy materials which formed the basis for the parameter determination by Darendeli (2001). Figure 5.12 illustrates the maximum radial displacements and pore pressure over frequency. The poroelastic effect is observed in this case for frequencies larger than 5Hz, where the amplification of the response of the porous material is larger than the single-phase material. It is associated with considerable pore pressure which is built up at such frequency range, whereas for frequencies less than 5Hz the pore pressures that build up are almost negligible. This is significant for liquefaction analyses, which are conducted considering frequencies around 10Hz. The amplification value is one order of magnitude larger than the respective values of the sand with large reference shear strain value (Figure 5.12). Therefore, as the nonlinearity gets more intense, the pore pressures are larger.

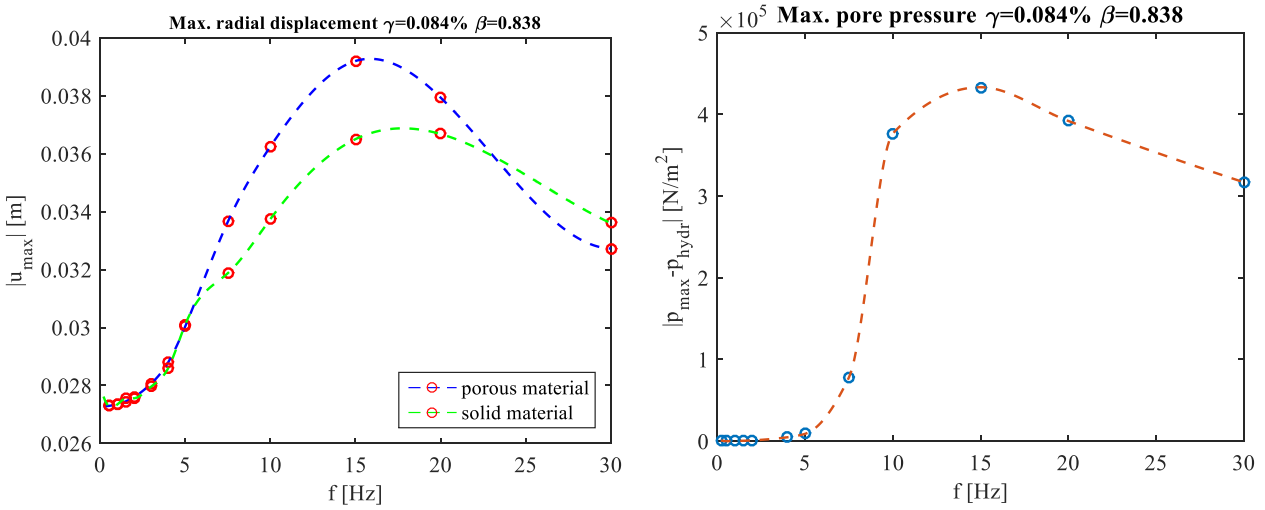

Figure 5.12. Maximum radial displacement over frequency for nonlinear poroelastic analysis (South Carolina sand: γ=0.084% β=0.838) and the respective pore pressure

For frequencies larger than 30Hz, the nonlinearity observed was so strong that led to unrealistically large displacements. An example is presented in Figure 5.13, which is the time series of the cavity response to sinusoidal load of 770kPa and 40Hz.

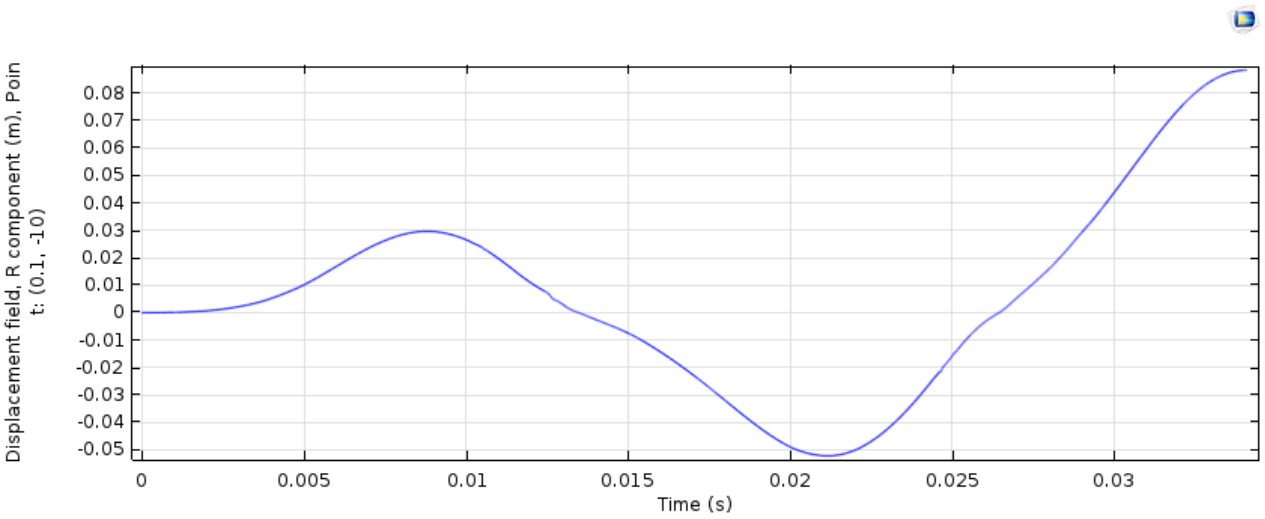

Figure 5.13. Nonlinear response to f=40Hz excitation (South Carolina sand: γ=0.084% β=0.838)

Next, the reference shear strain is reduced to 0.06%, so that the nonlinearity becomes even more intense. The difference in the maximum displacement compared to the elastic analysis is expected to be larger, based on the more rapid reduction of the secant shear modulus (Figure 5.10). Figure 5.14 confirms this expectation. For frequencies larger than 2Hz the difference between the nonlinear poroelastic and nonlinear elastic analysis become considerable whereas for frequencies larger than 15Hz, the analysis leads to a time series which follows the pattern of Figure 5.13. The pore pressure, which is illustrated by the right panel of Figure 5.14 is even larger than the one determined for the South Carolina sand. When the nonlinear effects become more intense, the developed pore pressure increases as well.

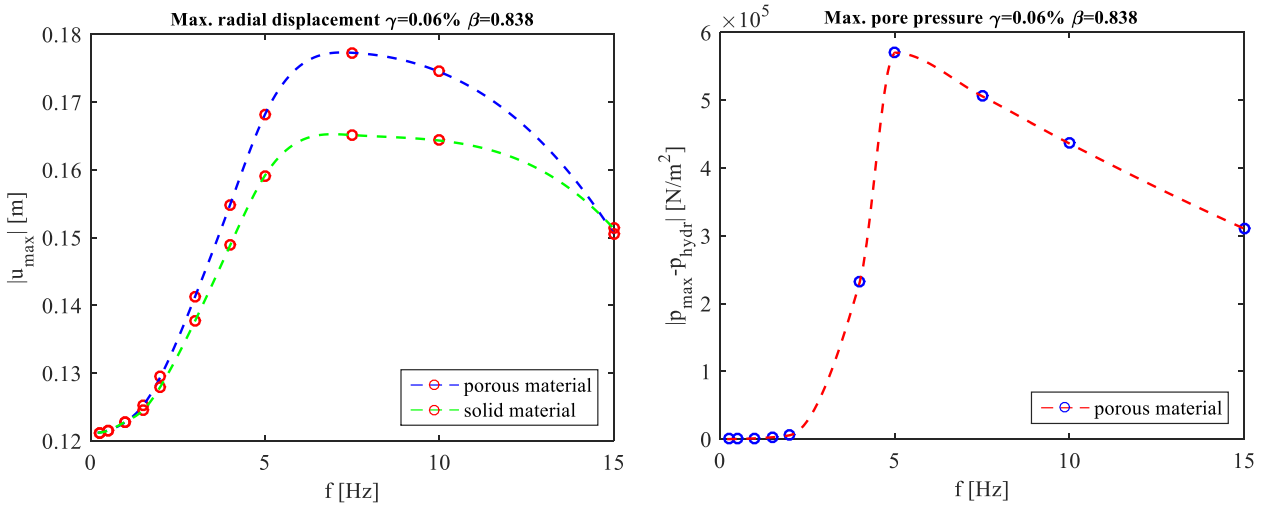

Figure 5.14. Maximum radial displacement over frequency for nonlinear poroelastic analysis (γ=0.06% β=0.838) and the respective pore pressure

Finally, the overall nonlinear parameters of Table 5.1 are used. The time series of the response for f=0.25Hz are shown in Figure 5.15. It can be observed that both the amplitude and the phase shift of the response is unrealistically large (20km at 1s later than expected). The nonlinearity is strong. Consequently, a shortcoming of the numerical solver COMSOL Multiphysics is detected: it cannot conduct stable analysis for such strong nonlinearity.

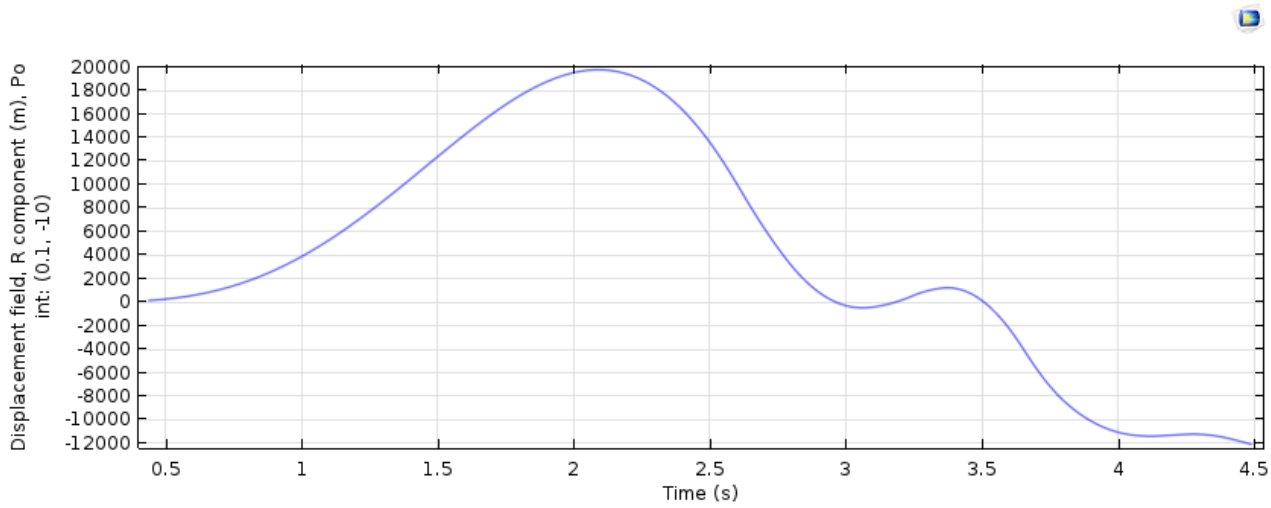

Figure 5.15. Nonlinear response to f=0.25Hz excitation at 10m depth (γ_{ref}=0.03% β=0.919)

5.3.2 Influence of the applied load

In this section, for a constant value of frequency (f=1Hz) the amplitude of the sinusoidal pressure applied is increased gradually from 50kPa to 1MPa. The lowest value leads to almost linear response, while the largest value is a common pressure applied in practice during pressuremeter tests at 10m depth. It is observed that nonlinearity is present even for very low pressure values, as can be seen in the right panel of Figure 5.16, which focuses on low pressure. The maximum displacement is calculated according to both the nonlinear elastic and the nonlinear poroelastic model. Both of them result in almost identical maximum displacements, mainly because the frequency of excitation is too low to excite considerable pore pressures, taking into account the results of the previous section. Consequently, the nonlinear poroelastic response to varying applied pressure is expected to be differ more at higher frequencies.

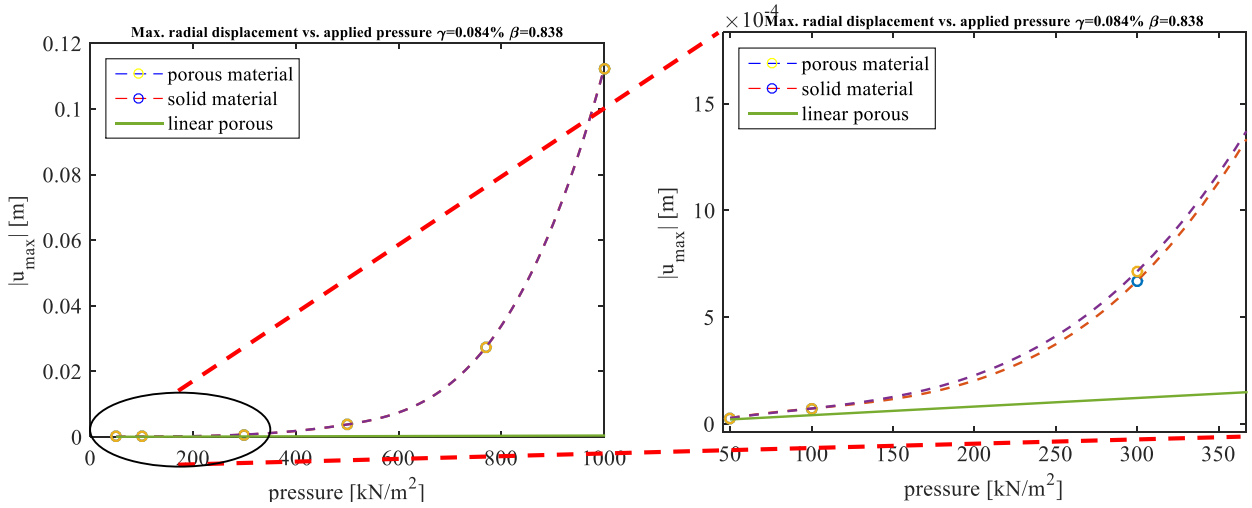

Figure 5.16. Maximum radial displacement vs. applied pressure: Comparison of the nonlinear poroelastic with the linear elastic and the nonlinear elastic analyses (f=1Hz)

5.3.3 Influence of the hydraulic conductivity of the porous medium

In this section, the permeability of the porous medium is modified to $k=10^{-3}$m/s and $k=10^{-6}$m/s, because these were the extreme hydraulic conductivity values throughout the present research. The influence of permeability on the poroelastic effect was significant in the case of the infinite soil bar (Section 3.1) but not of much importance for the cylindrical cavity expansion case (Section 3.2.3). Therefore, this influence is evaluated in this section for the nonlinear cylindrical cavity expansion. The nonlinear parameters are selected $\gamma_{ref}=0.06\%$ and $\beta=0.838$, corresponding to the material that exhibits the most intense nonlinear behaviour amongst the materials investigated in Section 5.3.1.

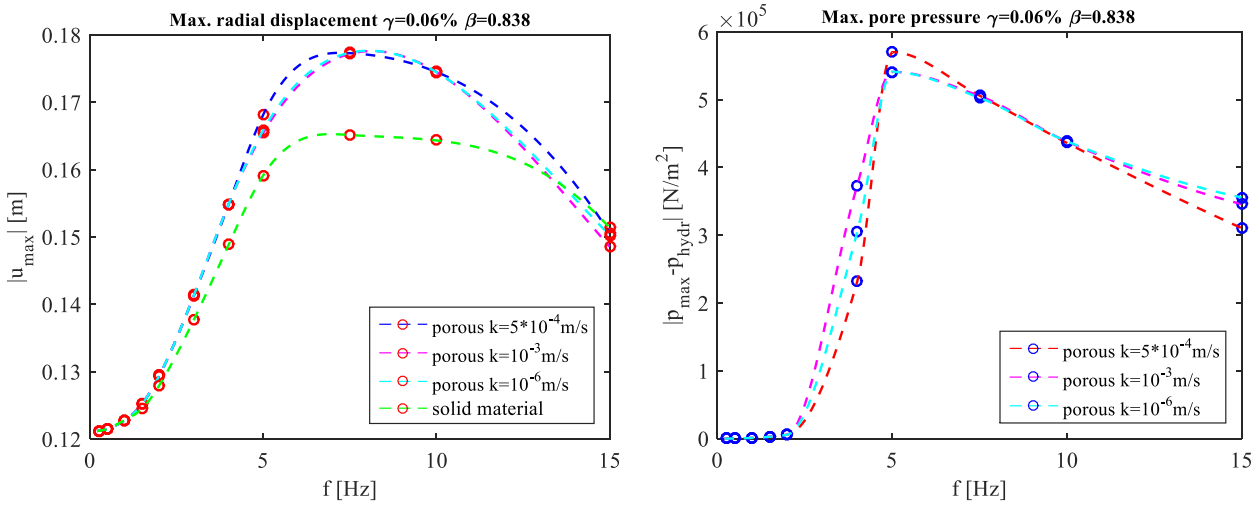

Figure 5.17. Maximum radial displacement over frequency for nonlinear poroelastic analysis (γ=0.06% β=0.838) and the respective pore pressure for both medium and highly permeable material

Figure 5.17 illustrates the maximum radial displacement of the poroelastic nonlinear analysis both medium ($k=5\cdot10^{-4}$m/s), high ($k=1\cdot10^{-3}$m/s) and low ($k=1\cdot10^{-6}$m/s) permeability and their comparison with the results of the single-phase analysis. It becomes clear that permeability is not a sensitive parameter, which can also be confirmed by the pore pressure for various frequencies (right panel).

5.3.4 Energy dissipation in nonlinear poroelasticity

The poroelastic effects are finally illustrated in terms of energy dissipation, taking into account that the latter can be measured by the area contained within the curve of a force-displacement graph. Figure 5.18 is an analogous graph to the ones presented in Section 3.2.7 for the linear analysis. It is observed that the area enclosed by the force-displacement poroelastic curve is larger than the elastic one. The difference is due to the Biot damping which acts additionally to the radiation damping. What is more, because of the nonlinear response and the higher-order harmonics, the force-displacement graph is not an ellipse, as it was for the linear case.

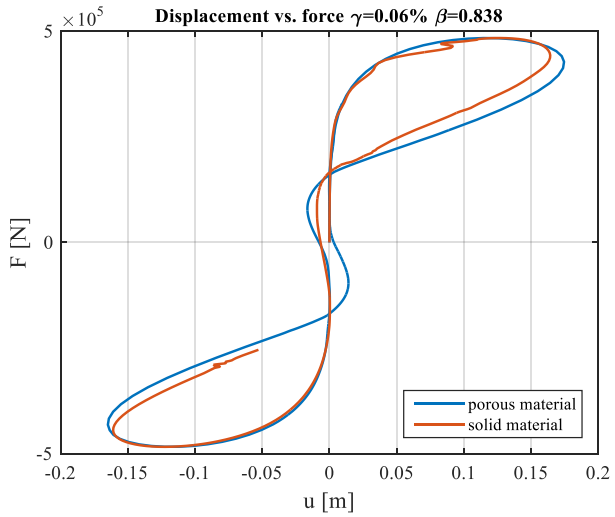

Figure 5.18. Force-displacement graph for f=10Hz: Nonlinear poroelasticity nonlinear drained elasticity

6

Conclusions and recommendations

6.1 Conclusions

During the present research, an extensive study on poroelastodynamics was conducted in order to determine the ground response to the dynamic cone pressuremeter test. Starting from the original Biot theory, the analytical solution of the wave propagation in a one dimensional porous medium was parametrically investigated in the low frequency range, which is the operational range of the test. The scope of this parametric analysis was to identify the two wave modes which propagate in the porous medium and quantify their effect. It was observed that the most crucial soil parameters that determine the response are the soil stiffness and permeability, which can be correlated. The stiffer sands which are closer to the nature of gravel are more pervious and vice versa. Hence, highly permeable materials ($k<10^{-4}$ m/s) exhibit significant relative displacement between the pore fluid and the solid particles (Figure 3.2). On the other hand, differences in porosity do not cause the two phases of the material to respond differently (Figure 3.6).

Additionally, the meaning of the phase velocity was thoroughly explained and the evolution of that parameter for both phases of the material with frequency was investigated. Although the fast compressional wave has a constant phase velocity over frequency, the slow mode exhibits an increasing phase velocity at low frequencies (Figure 3.11). However, it's amplitude ratio is constant with frequency whereas the amplitude of the fast mode increases with frequency (Figure 3.12). For large frequencies, but still within the low frequency range defined by Biot, the fast wave can also exhibit an amplitude ratio, because the difference in the mobilised inertia of each phase is more predominant.

Regarding the saturation of the porous medium, nearly saturated media make the poroelastic effects slightly more predominant than for the fully saturated media, but the difference is not remarkable. What is essential to be noted though is the influence in the overall displacement of the cavity. When air is entrapped in the pores, the displacement is much larger than the displacement of the fully saturated medium, because the fluid compressibility increases a lot (Figure 3.14). However, the displacement tends asymptotically to a certain value as the degree of saturation decreases, and therefore, further decrease than 95% does not affect the resulting displacement anymore. In addition, the presence of air in the pores brings the poroelastic response closer to the drained linear elastic response because of the reduced fluid stiffness.

Regarding the cavity expansion problem, the solution of Biot's theory was derived with the aid of Hankel functions. Analysis in the frequency domain results in a resonance frequency according to the poroelastic model equal to the drained linear elastic model, but with considerably larger amplification. In comparison with the undrained linear elastic model, the amplification in which both models result is the same. However, the undrained linear elastic model exhibits resonance at much lower frequencies (Figure 3.18). Consequently, the poroelastic model amplifies as much as the undrained linear elastic model at the same

frequency as the drained linear elastic model. The developed pore pressures around the resonance frequency are predicted to be much larger than the amplitude of the introduced stress, in accordance with the amplification ratio that was measured between the resonant response and the static displacement.

A crucial feature of the analysis is the radius of the cavity. As the cavity radius becomes larger, the resonance frequencies become smaller (Figure 3.21). However, the amplification ratio is the same for every cavity, since it does not depend on the radius of the cavity. The actual displacement figures on the other hand vary accordingly. This observation is valuable for the design of large cylindrical structures, such as offshore monopiles. Physical modelling of the monopile response is feasible using the dynamic cone pressuremeter test, but the response (amplitude, phase shift and frequency) should be extrapolated accordingly.

For the numerical modelling of the problem the FE platform COMSOL Multiphysics was used. This choice was based on the capability of this platform to couple different physical phenomena, such as solid mechanics and fluid flow studied here, and conduct efficiently dynamic analyses. In the frequency domain analysis, the amplitude spectrum is identical to that of the analytical solution (Figure 5.1). Hence, an accurate prediction is provided for the linear poroelastic analysis. However, one should be careful when evaluating the slow-wave phase velocity, because COMSOL Multiphysics defines it in a slightly different way than the literature.

Both COMSOL Multiphysics and the solution derived in the present study take into account the relative acceleration between the solid and the fluid phase, in contrast to the solution derived by Zienkiewicz et al. (1999). The assumption made by the latter is generally acceptable for the operational frequency range of the dynamic pressuremeter test. The differences in the resulting amplitudes are observed around the resonant frequency where the amplification is strong and are considerably small (Figure 5.1). As a result, the design engineer is advised to neglect the relative accelerations as well. However, special attention should be paid on that when the amplification is intense, for instance when the material stiffness is small. In general, the more intense the amplification, the more dominant the poroelastic effect is.

Because linear elasticity is a simplification of the soil behaviour, more advanced soil models are introduced and more specifically the nonlinear Hyperbolic law. However, nonlinear models require analysis in the time domain. Despite the fact that the derived set of equations of motion results in high-order time derivatives when it is transformed to the time domain using the inverse Fourier transformation, the equations of motion proposed by Zienkiewicz et al. (1999) can be directly used, since the aforementioned assumption of negligible relative displacements is valid. COMSOL Multiphysics can solve the dynamic consolidation formulation in time domain by manual coupling of the ‘Solid Mechanics’ interface with the ‘Darcy Law’ interface. The stronger the material nonlinearity gets, the larger the maximum radial displacements measured and additionally the stronger the poroelastic effect (Figure 5.11, Figure 5.12 and Figure 5.14). The effect of applied pressure and hydraulic conductivity of the material was also examined, leading to the conclusion that they are not sensitive parameters compared to the material nonlinearity. It should be noted that COMSOL Multiphysics exhibits a limitation when nonlinearities are very strong.

Moreover, the nonlinear response exhibits an amplification peak that is observed in lower frequencies, as the nonlinearity gets stronger (Figure 5.11, Figure 5.12 and Figure 5.14). This peak is associated to the development of pore pressures. The latter are generally smaller as the initial confining pressure, and

therefore initial stiffness, is larger. When nonlinearity gets more intense, the pore pressure build-up is more intense as well, leading to the aforementioned larger maximum displacements.

Therefore, for low frequencies (smaller than 5Hz) the poroelastic analysis does not seem to be necessary when the material is nonlinear. A nonlinear elastic drained analysis is appropriate instead. However, for liquefaction analysis (frequency range of about 10Hz), strong nonlinearity leads to intense poroelastic effects. The same applies to modelling of the dynamic behaviour of monopiles using the cone pressuremeter, when the frequency applied to the pressuremeter should be larger than the frequency of excitation of the actual monopile. Overall, the dynamic cone pressuremeter test can be an effective test to tackle nonlinearity and quantify it, and therefore determine the nonlinear parameters γ_{ref} and β. Except for that, the cone pressuremeter test is a possible method to assess the drainage condition of the soil (drained, partially drained, or rather undrained).

6.2 Recommendations for further research

The objective of the present research was to point out the poroelastic effect during the dynamic cone pressuremeter test. Both linear and nonlinear soil behaviour were investigated, resulting in the respective responses which were found to be different from each other with different features being determinant for each case. The model, however, has not incorporated hysteretic damping, which results to energy dissipation. In addition, the development of irreversible plastic strains leads to dependency of the response on the loading cycles, which is significant for the execution of the cone pressuremeter test. Thereafter can the computed response be even more realistic.

Regarding the nonlinear response, it was found that during the execution of the test higher order harmonics are excited. An additional stiffness term of third order, whose coefficient (k_3 of the Duffing equation) is recommended to be specified and linked to the nonlinear parameters, with the aid of the Duffing equation, which can quite accurately describe the nonlinear response to dynamic loading. An analytical solution of the nonlinear poroelastodynamics can be derived.

Finally, it was concluded that mainly the nonlinear parameters and the soil stiffness, along with the frequency, the applied pressure and the permeability can alter the response, in terms of the maximum displacement, the amplification frequency and the pore pressure. The sensitivity of these factors varies and therefore it is recommended that an extensive sensitivity analysis is conducted to result in a few non-dimensional factors which determine the nonlinear response.

Overall, the present research adds value to the prediction of the dynamic response of the ground to load by an expanding cavity. It can be directly applied to the dynamic version of the cone pressuremeter test, when the pressure is applied with specific frequency. Moreover, it expands the field of knowledge to further applications, such as the offshore monopile design and earthquake analysis, possibly predicting the occurrence of liquefaction.

References

Abbas, I.A., Abd-alla, A.N. (2012). A two-dimensional wave propagation in a poroelastic infinite circular cylinder. Journal of Physics, Vol.1 No.3, pp. 32-38.

Aliguer, I. et al. (2015). Numerical stress initialisation in geomechanics via the FEM and a two-step procedure. Proceedings of the XIII International Conference on Computational Plasticity: Fundamentals and applications. pp. 667-676.

Atalla, N., Panneton, R. and Debergue, P. (1998). A mixed displacement pressure formulation for poroelastic materials. J. Acoust. Soc. Am. 104, pp. 1444-1452.

Ballivy, G. (1995). The pressuremeter and its new avenues. Rotterdam [u.a.]: Balkema.

Berenger, J. (1994). A perfectly matched layer for the absorption of electromagnetic waves. Journal of Computational Physics, 114(2), pp.185-200.

Biot, M. A. (1941). General Theory of Three-Dimensional Consolidation. J. Appl. Phys., 12, pp. 155–164.

Biot, M. A. (1956). Theory of propagation of elastic waves in a fluid saturated porous solid. I Low frequency range. J. Acoust. Soc. Am. 28, pp. 168–178.

Biot, M. A. (1962), Mechanics of Deformation and Acoustic Propagation in Porous Media, J. Appl. Phys., 33, pp. 1482–1498.

Chan, A. H. C. (1988). A unified finite element solution to static and dynamic geomechanics problems. Ph.D. Dissertation, University College of Swansea, Wales.

Cheng, A. H.-D. (2016). Poroelasticity. Springer.

COMSOL Acoustic Module User's Guide Version 4.3b (2013).

COMSOL Multiphysics Reference Manual Version 5.2 (2015).

Deresiewicz, H. and Skalak, R. (1963). On uniqueness in dynamic poroelasticity. Bull. Seismol. Soc. Am., 53, pp. 783-788.

Detournay, E. and Cheng, A.H.-D. (1993). Fundamentals of poroelasticity. Comprehensive Rock Engineering: Principles, Practice and Projects, Vol. II, pp. 113-171.

Fahey, M. Carter, J. P., (1993). A finite element study of the pressuremeter test in sand using a nonlinear elastic plastic model. Canadian Geotechnical Journal. 30(2), pp. 348-362.

Frenkel, J. (1944). On the Theory of Seismic and Seismoelectric Phenomena in a Moist Soil. J. Phys. _USSR_, 3, pp. 230–241.

Gao, M., Wang, Y., Gao, G. and Yang, J. (2013). An analytical solution for the transient response of a cylindrical lined cavity in a poroelastic medium. Soil Dynamics and Earthquake Engineering, 46, pp. 30-40.

Hardin, B.O. and Drnevich, V.P., (1972). Shear modulus and damping in soils: Design equations and curves. J. Soil Mech. Found. Div., 98(7), pp. 667-692.

Hardin, B. O. (1978). The nature of stress-strain behaviour of soils, State-of-the-art report. Proceedings of the ASCE Specialty Conference on Earthquake Engineering and Soil Dynamics, Vol. 1 ASCE, Pasadena, pp. 3-90.

Johnson, S. (2007). Notes on Perfectly Matched Layers (PMLs).

Karunakaran, D. and Spidsøe, N. (1997). Verification of methods for simulation of nonlinear dynamic response of jack-up platforms. Marine structures, 10(2-4), pp. 181-219.

Kestin, J., Sokolov, M. and Wakeham, W. (1978). Viscosity of liquid water in the range −8 °C to 150 °C. Journal of Physical and Chemical Reference Data, 7(3), p.941.

Kramer, S. (1996). Geotechnical earthquake engineering. Upper Saddle River, N.J.: Prentice Hall, USA.

Marburg, S. (2002). Six boundary elements per wavelength: Is that enough?. Journal of Computational Acoustics, 10(01), pp.25-51.

Matyka, M., Khalili, A. and Koza, Z. (2008). Tortuosity-porosity relation in porous media flow. Physical Review E, 78(2).

Metrikine, A. and Vrouwenvelder, A. (2015). Dynamics of Structures - CT4140, Lecture notes, Delft, Netherlands.

Nayfeh, A. (1993). Introduction to perturbation techniques. New York. Wiley.

Richard, F.E., Hall, J.R. and Woods, R.D., (1970). Vibrations of soils and foundations. Prentice-Hall, Inc., Engelwood Cliffs, N.J.

Schanz, M. (2009). Poroelastodynamics: linear models, analytical solutions and numerical methods. Appl. Mech. Rev. ASME 62 030803.

Schnaid, F. (n.d.). Pressuremeter testing. Federal University of Rio Grande do Sul, Brazil.

Senjuntichai, T., and Rajapakse, R. K. N. D. (1993). Transient Response of a Circular Cavity in a Poroelastic Medium. Int. J. Numer. Analyt. Meth. Geomech., 17, pp. 357–383.

Smeulders, D. (1992). On wave propagation in saturated and partially saturated porous media. [S.l.: s.n.].

Terzaghi, K. (1925). Erdbaumechanik auf bodenphysikalischer Grundlage. Leipzig and Wien. Franz Deuticke.

Van Dalen, K. N. (2013). Multi-component acoustic characterization of porous media. Berlin: Springer.

Vardoulakis, I. and Beskos, D. E. (1986). Dynamic Behavior of Nearly Saturated Porous Media. Mech. Mater., 5, pp. 87–108.

Verruijt, A. (2010). An introduction to soil dynamics. Dordrecht: Springer.

Verruijt, A. (2015). Theory and problems of poroelasticity. Delft, Netherlands.

Whittle R. (n.d.). A description of the cone pressuremeter and the associated parts

Withers, N.J., Schaap, L.H.J. and Dalton, C.P. (1986). The development of a full displacement pressuremeter. The pressuremeter and its marine applications, Second International Symposium: ASTM STP 950, American Society for Testing and Materials, pp. 22-37.

Zienkiewicz, O. (1999). Computational geomechanics with special reference to earthquake engineering. Chichester: Wiley.

Appendix

A. General solution of the cavity expansion problem

If purely elastic conditions are assumed, the stresses are correlated to the strains according to Hooke's law:

$$\sigma_{rr} = \lambda\varepsilon + 2\mu\varepsilon_{rr} \quad \text{A.1}$$

$$\sigma_{tt} = \lambda\varepsilon + 2\mu\varepsilon_{tt} \quad \text{A.2}$$

where $e = \varepsilon_{rr}+\varepsilon_{tt}$ is the volumetric strain and λ, μ the Lamé constants. If u is the radial displacement, then the radial and tangential strains can be correlated to it, by:

$$\varepsilon_{rr} = \frac{du}{dr} \quad \text{A.3}$$

$$\varepsilon_{tt} = \frac{u}{r} \quad \text{A.4}$$

As a result, the equation of static equilibrium in the radial direction is:

$$\frac{d\sigma_{rr}}{dr} + \frac{\sigma_{rr} - \sigma_{tt}}{r} = 0 \Rightarrow (\lambda + 2\mu)\left[\frac{d^2u}{dr^2} + \frac{1}{r}\frac{du}{dr} - \frac{u}{r^2}\right] = 0 \Rightarrow \left[\frac{d^2u}{dr^2} + \frac{1}{r}\frac{du}{dr} - \frac{u}{r^2}\right] = 0 \quad \text{A.5}$$

The general solution of the static equilibrium equation is:

$$u = Ar + \frac{B}{r} \quad \text{A.6}$$

and the stresses can be expressed as (Verruijt, 2010):

$$\sigma_{rr} = 2(\lambda + \mu)A - 2\mu\frac{B}{r^2} \quad \text{A.7}$$

$$\sigma_{tt} = 2(\lambda + \mu)A + 2\mu\frac{B}{r^2} \quad \text{A.8}$$

For the dynamic solution, an additional inertia term is added, so it becomes:

$$\left[\frac{\partial^2u}{\partial r^2} + \frac{1}{r}\frac{\partial u}{\partial r} - \frac{u}{r^2}\right] = \frac{1}{c^2}\frac{\partial^2 u}{\partial t^2} \quad \text{A.9}$$

where $c = \sqrt{[(\lambda+2\mu)/\rho]}$ is the compression wave velocity.

The calculation of the response of the cylindrical cavity expansion problem in linear elastic medium is conducted according to Verruit (2010). Assuming that the boundary responds harmonically to sinusoidal loading, i.e.

$$u = F(r)e^{i\omega t} \quad \text{A.10}$$

the differential equation (A.9) in the frequency domain is:

$$\frac{d^2F}{dr^2} + \frac{1}{r}\frac{dF}{dr} + \left(\frac{\omega^2}{c^2} - \frac{1}{r^2}\right)F = 0 \quad \text{A.11}$$

The general solution of the differential equation (AA.11) is

$$F(r) = AJ_1(\omega r/c) + BY_1(\omega r/c) \quad \text{A.12}$$

where J_1 and Y_1 are Bessel functions and A=iB, because of the radiation condition (waves propagate to infinity where there is no reflection).

The constant B is calculated from the loading boundary condition on the cavity

$$\sigma_{tot,rr} = -p_0 e^{i\omega t} \quad \text{A.13}$$

with the following stress strain relationship

$$\sigma_{tot,rr} = \lambda\varepsilon + 2\mu\varepsilon_{rr} = \lambda(\varepsilon_{rr} + \varepsilon_{tt}) + 2\mu\varepsilon_{rr} \quad \text{A.14}$$

If ε_{rr}=du/dr and ε_{tt}=u/r, substitution in the boundary condition gives after elaboration:

$$B = -p_0 \Big/ \left[(\lambda + 2\mu)\left(i\omega\frac{J_0(\omega r_0/c)}{c} + \omega\frac{Y_0(\omega r_0/c)}{c}\right) - 2\mu\left(i\frac{J_1(\omega r_0/c)}{r_0} + \frac{Y_1(\omega r_0/c)}{r_0}\right)\right] \quad \text{A.15}$$

As a result, by making use of equations (A.10), (A.12) and the relation A=iB, the final solution for a sinusoidal load is:

$$u = Im\left\{\frac{-p_0[iJ_1(\omega r/c) + Y_1(\omega r/c)]e^{i\omega t}}{\left[(\lambda + 2\mu)\left(i\omega\frac{J_0(\omega r_0/c)}{c} + \omega\frac{Y_0(\omega r_0/c)}{c}\right) - 2\mu\left(i\frac{J_1(\omega r_0/c)}{r_0} + \frac{Y_1(\omega r_0/c)}{r_0}\right)\right]}\right\} \quad \text{A.16}$$

B. One dimensional wave propagation in an infinitely long soil bar

Figure A.6.1 illustrates the ground response to sinusoidal loading of relatively high frequency. Displacements and stresses are plotted in time for 5 random points of the domain in order to present the development of the variables. The latter are also plotted over distance from the cavity. The phase shift of the various points across the domain is equal for effective stresses and pore pressures. The same applies for the displacement components as well. The effective stresses developed are relatively small. About the graphs over distance, the pressure and displacement variables are plotted every 0.1s. The two aforementioned waves cannot be distinguished in this case, because of the low permeability of the medium.

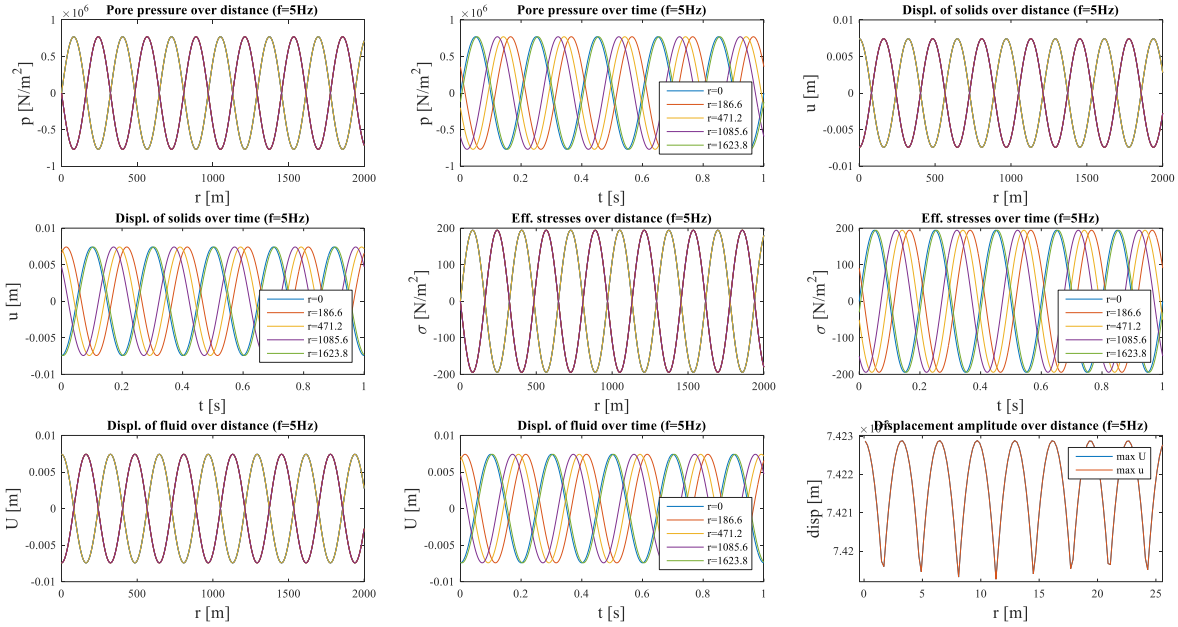

Figure A.6.1. Response to sinusoidal load of low permeability soil (k=10^{-6}m/s)

Regarding the highly-permeable material, the effective stresses are much higher compared to the lower permeability material. The amplitude of the displacements, on the other hand, seems to be independent of permeability. The amplitudes of all variables attenuate with distance from cavity. However, the effective stresses at the cavity are much smaller than the rest of the domain examined. The second kind wave is probably of higher amplitude than the case of lower permeability, and this can explain the decay of variables (clearly visible in the last graph of Figure A.6.2).

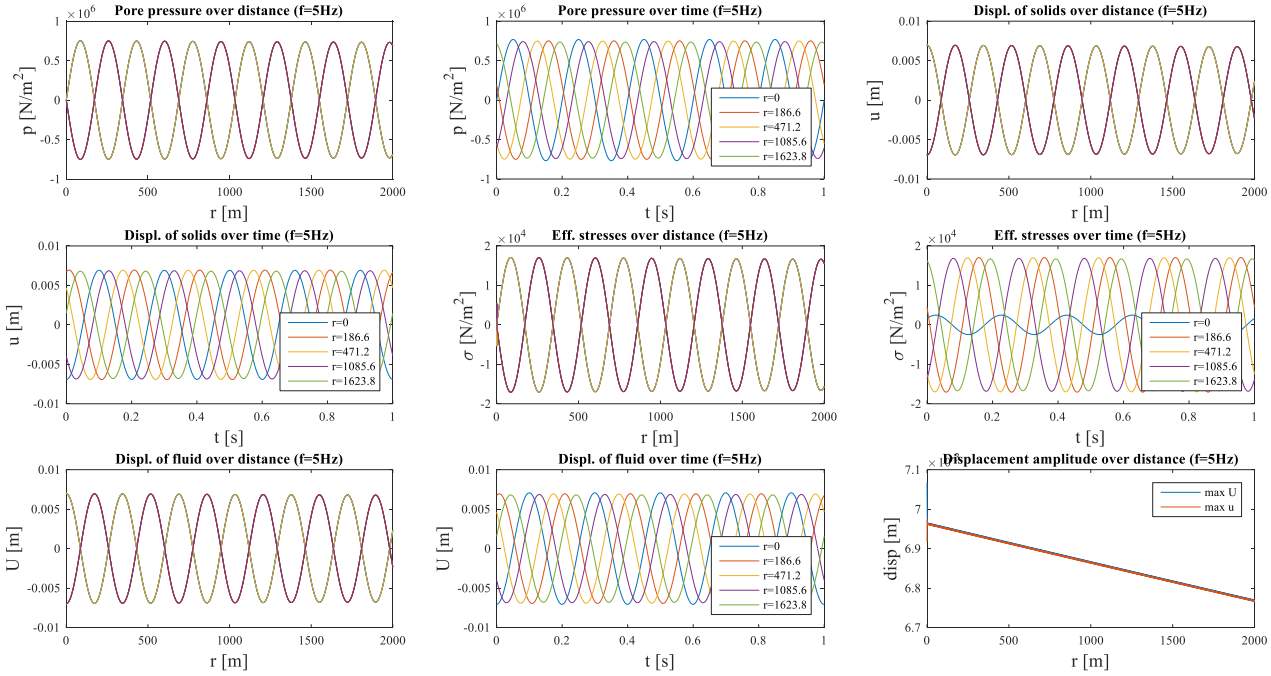

Figure A.6.2. Response to sinusoidal load of high permeability soil (k=10^{-3}m/s)

Figure A.6.3 presents the response of unsaturated ground to high frequency sinusoidal excitation. The effective stresses developed in this case are higher than those developed in fully saturated soil. The opposite implies for the pore pressures. The displacements are higher than the saturated cases. In addition, a slight decay of all stress and displacement variables is observed in distance, while the displacement of the fluid drops significantly within a few centimeters away from the cavity (last graph of Figure A.6.3).

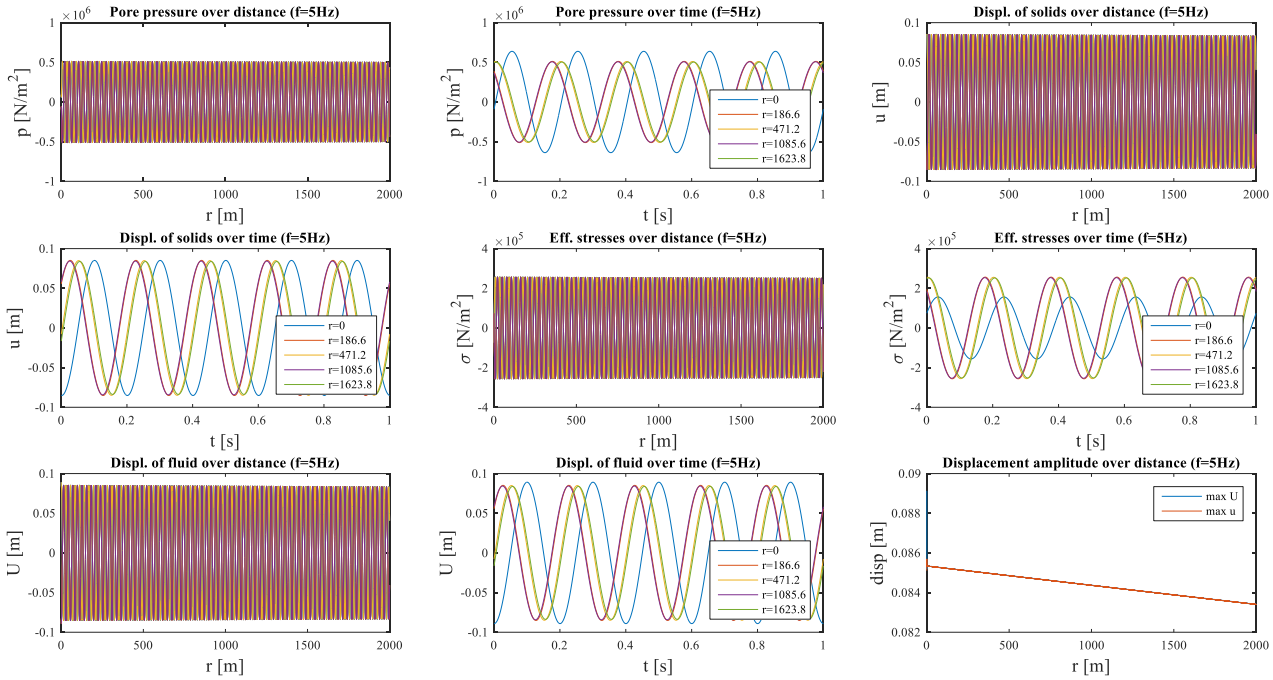

Figure A.6.3. Unsaturated soil (1% air content) response to sinusoidal load

The amplitudes of the displacement of both the solid phase and the fluid are larger, when the porosity increases, because the proportion of the more compressible material (fluid) is larger. The same occurs for the effective stresses as well. No significant amplitude decay is to be observed at this case.

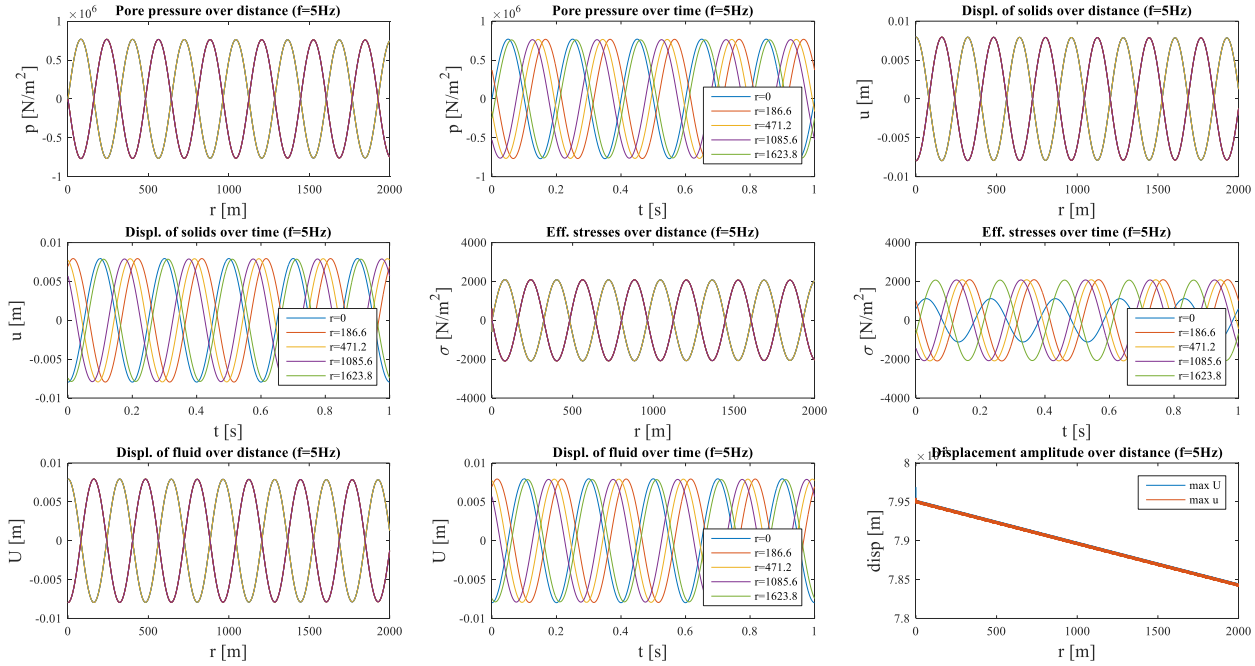

Figure A.6.4. Response of material with high porosity (n=0.45)

Figure A.6.5 illustrates the response of a lower porosity material. The phase shift evolves differently throughout the domain compared to the higher porosity material. The displacement and effective stress amplitudes are also lower, in this case. The decay rate of the displacements is equivalent to the higher porosity medium.

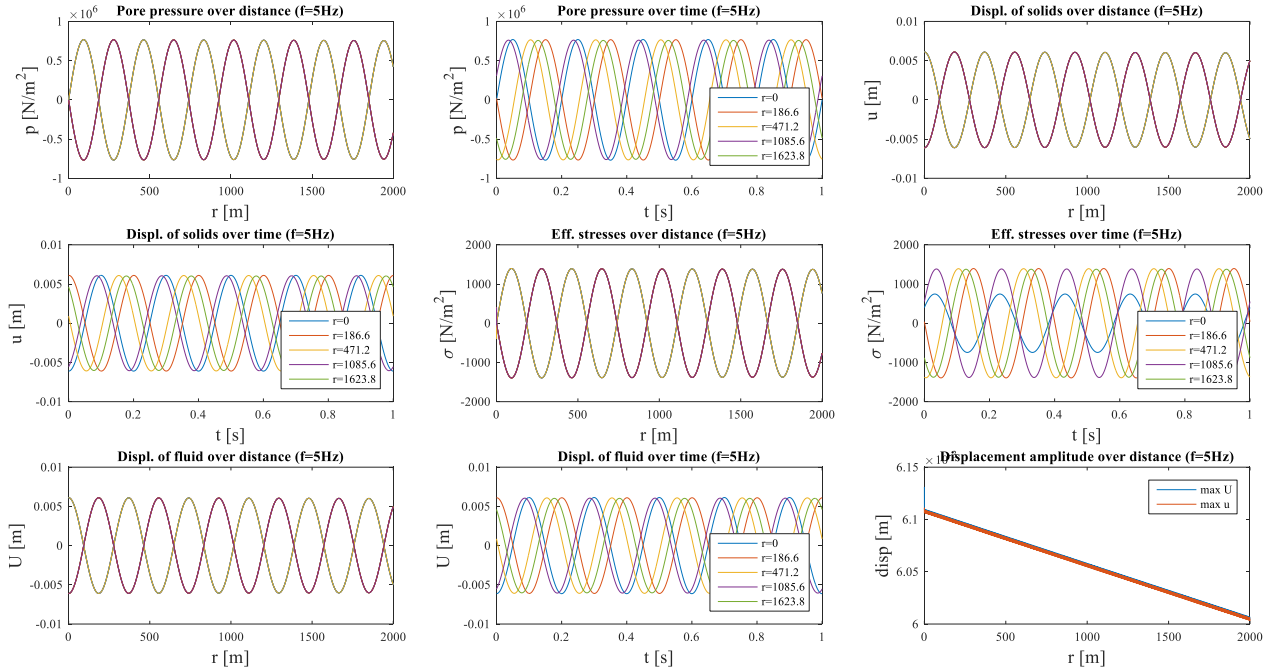

Figure A.6.5. Response of material with relatively low porosity (n=0.3)

In contrast to the high frequency excitation, the development of all variables for the low-permeability material over distance fluctuates with a larger period, as can be observed in Figure A.6.6. Response to sinusoidal load of low permeability soil (k=10^{-6}m/s) The amplitudes of the stress variables are equal to the

high frequency excitation, but the displacements of both fluid and solid phase become significantly larger when the frequency is reduced.

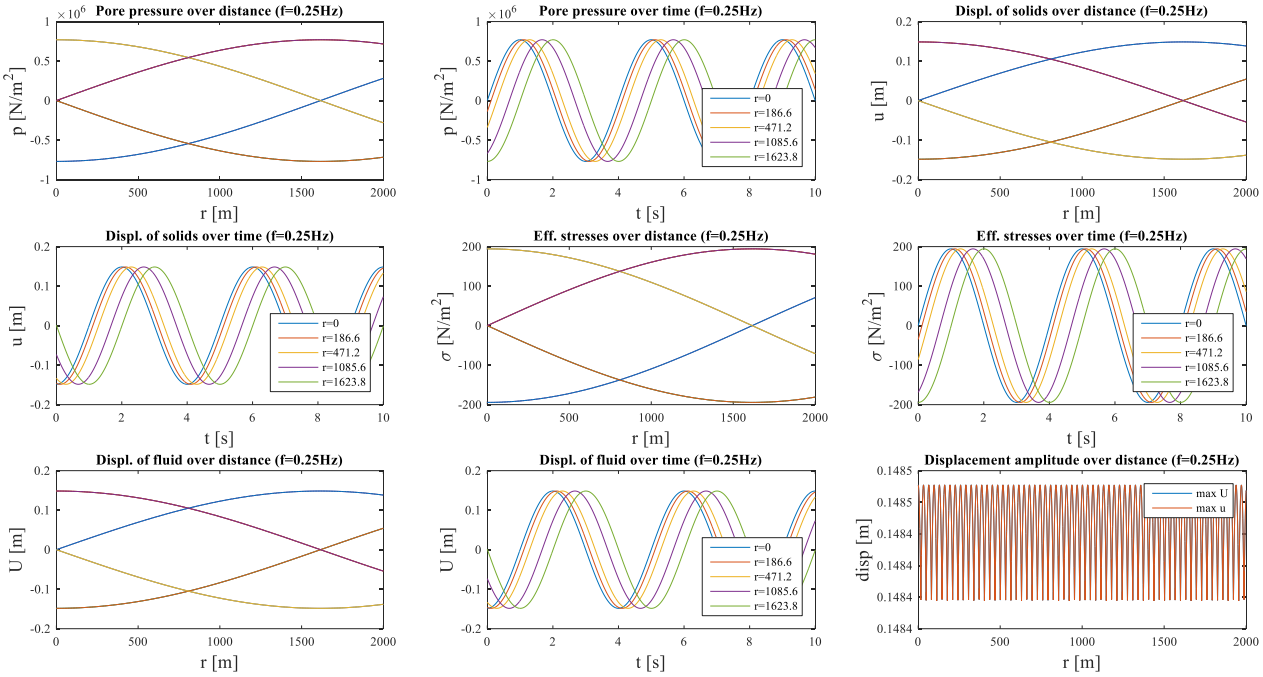

Figure A.6.6. Response to sinusoidal load of low permeability soil (k=10^{-6}m/s)

When the permeability is low (k=10^{-3}m/s), the effective stresses increase rapidly, because the pore pressures dissipate faster. Within a few meters away from the cavity the solid and fluid phase exhibit a slight different amplitude, but this difference attenuates quickly, and the displacements become equivalent for both solid matrix and pore fluid. The effective stresses also exhibit a different kind of fluctuation within the first two meters from the cavity.

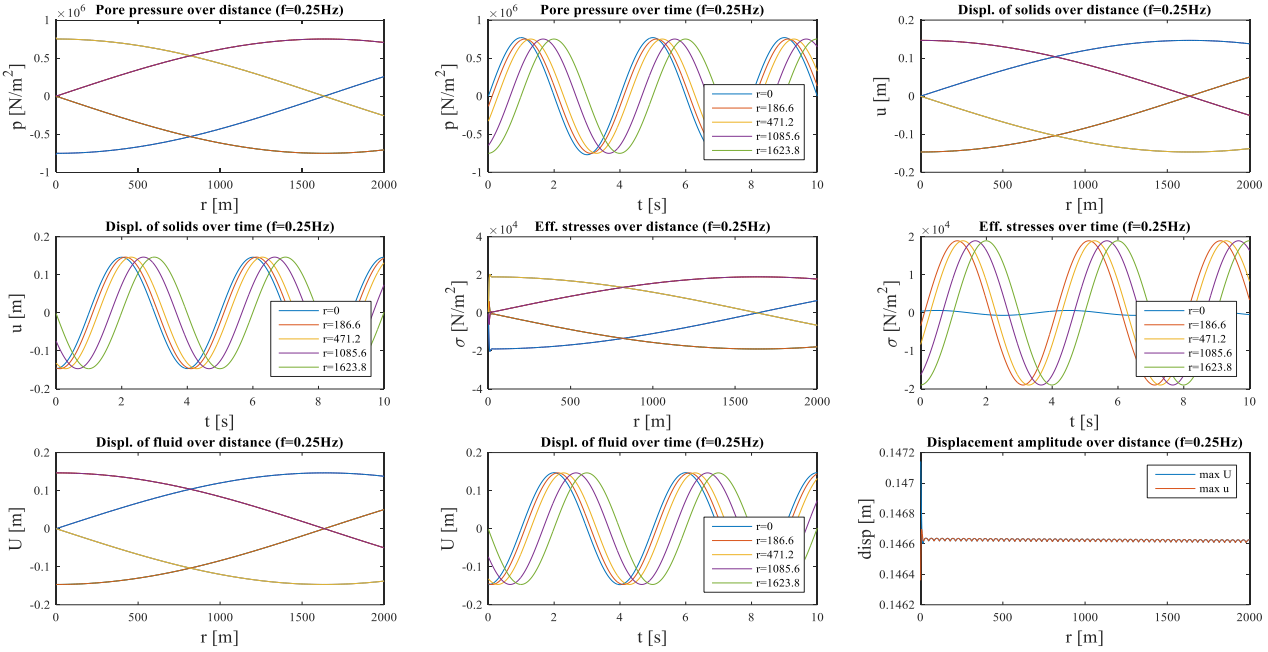

Figure A.6.7. Response to sinusoidal load of high permeability soil (k=10^{-3}m/s)

For the nearly saturated material, the results are plotted in Figure A.6.8. The development of stresses over distance are plotted only for the first few meters away from the cavity, where they exhibit a different kind of fluctuation from the rest of the domain. In this case, the displacements are unexpectedly high (order of magnitude of meters). They are different between the two phases of the porous material, but they become equal within about 3m away from the cavity, as can be observed by the last graph of Figure A.6.8.

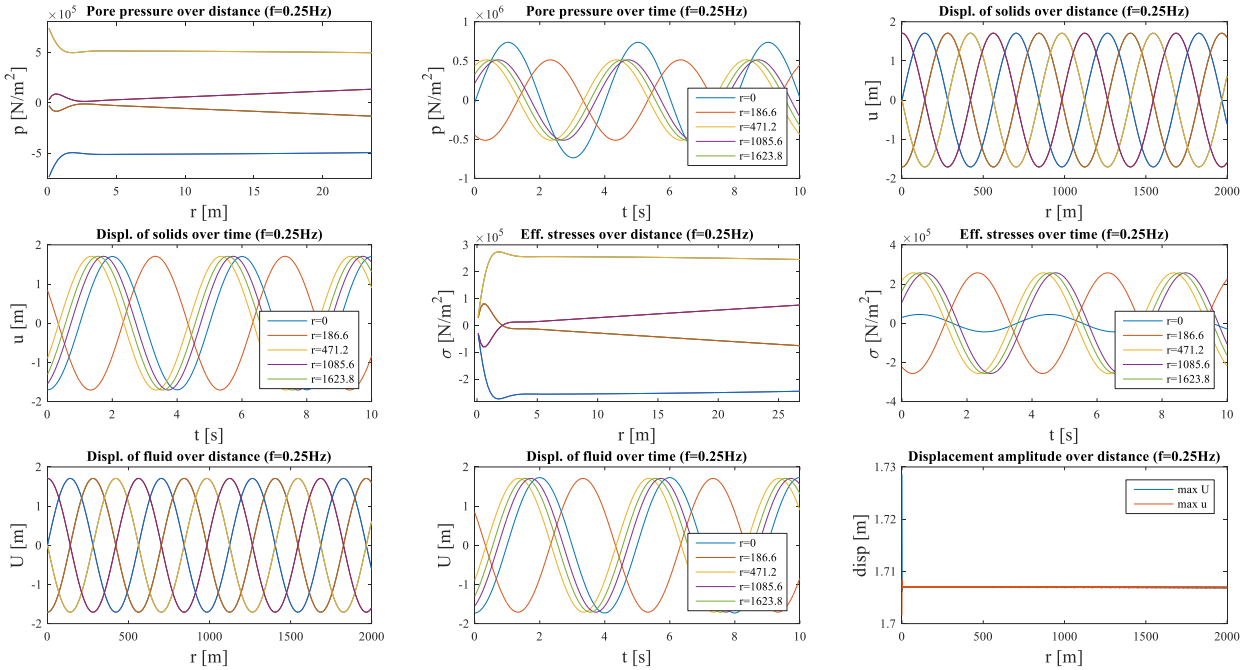

Figure A.6.8. Unsaturated soil (1% air content) response to low frequency sinusoidal load

C. Modelling with COMSOL Multiphysics 5.2

As already mentioned in the present report, COMSOL Multiphysics is a powerful tool when multiple physical phenomena need to be modelled and coupled. In the present research, the analyses were focused on the dynamic response of a porous medium. In this section some details/guidelines will be given for future reference.

- Modelling the poroelastic response in the frequency domain

The 'Poroelastic Waves' interface is the appropriate tool to conduct linear poroelastic analysis in the frequency domain. Special attention should be paid to the discretisation of the domain, which has to take into account the minimum wavelength expected. The element size should be defined by resticting the maximum size and set this equal to (at least) 6 elements per wavelength. One should be careful about the 'slow wave speed' defined by the software itself (as pelw.cp_slow). It is not the same as the phase velocity discribed in the literature!

Regarding the boundary absorption of the incoming waves, a very coarsely meshed PML with the default setting works fine. Always use a mapped mesh with PML!

- Modelling the poroelastic response in the time domain

This can be done efficiently using the 'Poroelasticity' interface, but only if it is linear. However, 'Poroelasticity' models a static consolidation model, and therefore, the dynamic terms have to be added

manually. There are modelling nodes for that. If specified variables have to be modified (such as the Darcy velocity field), this can be done within the 'Equation View' of the material node in the Model Builder.

When it comes to multiple stage modelling, one can refer to variables resulting from previous solutions using the structure: withsol('sol#',variable name) e.g. withsol('sol1',poro.sr) If the stages are defined as continuous steps within the same study, one does not have to do the aforementioned setting. This is only necessary to set parameter or initial values as a function of results of previous solutions. It is also recommended to set as user controlled the initial values of the dependent variables in the 'Values of independent variables' section of the settings of the next study step, if different studies are linked.

COMSOL Multiphysics uses the solid mechanics notation; that is; negative sign for compression and positive for tension. The same is valid for pore pressure as well.

Regarding the absorption of the waves, the PMLs used for the frequency-domain analysis should be replaced by a 'Symmetry' boundary condition.

- Modelling nonlinear poroelastic behaviour

This should be done using coupled 'Solid Mechanics' and 'Darcy Law' interfaces instead of 'Poroelasticity' because the latter does not allow for nonlinear models. In the 'Solid Mechanics'-->Structural Transient Behaviour one should just activate the inertial terms to avoid setting them as body loads.

COMSOL Multiphysics 5.2 works with total stresses while the new update (5.2a) works with effective stresses. Maybe using 5.2a it is possible to use the 'Poroelasticity' interface and couple it with 'Solid Mechanics'. The latter will be only used to compute the secant G while 'Poroelasticity' will conduct equivalent linear poroelasric analysis with varying G_sec.

Regarding the single-element tests, they resulted in non-uniform stresses within the same element which is strange. This might be investigated as well. In principal however, one cannot add more geometrical nodes to define a more uniform nodal load or displacement, because COMSOL remeshes the domain automatically according to the geometrical nodes added. A point load cannot be defined either without defining a geometrical node. Last but not least, one should pay attention while using rollers or equivalent boundary conditions based on the respective stresses. One example of this is described in Chapter 4 where the boundary conditions are explained both for the time-domain analysis and the single-element tests.